



UNIVERSITAT DE VALÈNCIA

DOCTORAT EN FÍSICA

Precise phenomenology in the LHC era

Ivan Rosario Bonastre

supervised by
Dr. Francisco CAMPANARIO Pallás

October 11, 2021

Francisco Campanario Pallás, Investigador Ramón y Cajal del Departamento de Física Teórica de la Universidad de Valencia,

CERTIFICA que la presente memoria “**Precise Phenomenology in the LHC era**” ha sido realizada bajo su dirección, en el Departamento de Física Teórica de la Universidad de Valencia, por D. **Ivan Rosario Bonastre**, y constituye su Tesis Doctoral para optar al grado de Doctor por la Universidad de Valencia.

Y para que así conste, en cumplimiento de la legislación vigente, presenta ante la Facultad de Física de la Universidad de Valencia la referida memoria, y firma el presente certificado

en Burjassot, a 24 de Setiembre de 2021

Francisco Campanario Pallás

Abstract

Since the detection of the Higgs boson in 2012, the experimental community has centered its efforts on precision measurements of the Standard Model. To satisfy the demands of the experimental precision at the LHC in the foreseeable future, next-to-leading order calculations are mandatory.

The LHC is a hadron collider, meaning that high multiplicity final states are to be expected due to QCD radiation. To compare our theoretical predictions with the experiment, this QCD radiation has to be modeled and computed, which is done with parton showers and calculated with Monte Carlo (MC) event generators.

MCs are usually only capable of leading order predictions of the partonic cross-section but can be interfaced with other programs that provide the next-to-leading order amplitude. Furthermore, the next-to-leading order amplitude can be matched with the parton shower and hadronized to obtain observables that can be compared with the experiment.

In this thesis, the di-photon production process through vector-boson scattering in the vector-boson scattering approximation is implemented in the parton level Monte Carlo VBFNLO. This implementation contains anomalous couplings for the vector bosons and the Higgs, including dimension-6 and -8 operators, which allows to systematically account for effects of physics beyond the Standard Model.

The interface proposed at Les Houches is implemented in VBFNLO for all di-boson and tri-boson processes with leptonic decays. We use this interface to communicate with the MC event generator Herwig and perform a phenomenological study of parton shower effects in selected tri-boson production processes.

Contents

1	Introduction	3
2	Theoretical Background	6
2.1	The Standard Model	6
2.1.1	Quantum Chromodynamics	9
2.1.2	Electroweak Model	10
2.2	Effective Field Theory	13
2.3	LHC Physics	15
2.3.1	The experiments	16
2.3.2	Rapidity and pseudorapidity	16
2.3.3	Parton model	18
2.3.4	Next-to-Leading-Order QCD Calculations	19
2.3.5	Jet Observables	24
2.3.6	Monte Carlo	26
2.3.7	Catani-Seymour Subtraction	28
2.3.8	Parton Shower	32
2.3.9	Frixione Isolation	35
3	Di-photon production in the VBS channel	37
3.1	Introduction	37
3.2	Implementation	40
3.2.1	Born contributions	41
3.2.2	Real contributions	47
3.2.3	Virtual contributions	49
3.2.4	Anomalous Couplings	56
3.3	Checks	56
3.4	Phenomenological Results	60
3.4.1	Parameters and cuts	61
3.4.2	Comparisons with other VBS processes	64
3.4.3	Differential distributions	65
3.4.4	Anomalous couplings	71
4	Parton Shower in Di-boson and Tri-boson processes	72
4.1	Introduction	72
4.2	Interface Implementation	74
4.2.1	Pre-runtime phase	76
4.2.2	Initialization phase	77
4.2.3	Runtime phase	80
4.3	Checks	82

4.4 Phenomenological Results	84
4.4.1 Scale Variations	84
4.4.2 Frizione Isolation Cut	89
5 Conclusions	93
6 Resum	96

Chapter 1

Introduction

The 20th century was a pivotal time for physics. When the century started, physicists still used as their principal theoretical toolset the classical theories of Newton and Maxwell, and statistical methods were recently introduced to describe the macroscopic properties of ensembles of particles. When it finished, quantum mechanics was understood as the fundamental description of our universe, the theory of relativity established as the correct description of the spacetime geometry, and the **Standard Model** (SM) of particle physics was basically finished. While a typical argument between physicists at the end of the 19th century would involve the existence of atoms, the fundamental nature of thermodynamics, or the movement of the earth relative to the static background, and we could hear terms like ether and phlogiston. At the start of the 21st century, physicists will argue about unification, inflation, dark matter, and extra dimensions. The existence of atoms is not only established, but we now know they are not even fundamental. Not even the particles found in the atomic nucleus, like the proton or neutron, are fundamental. The 20th century was a century of revolutions in physics. While particle physicists were probing smaller and smaller distances, discovering new particles, astronomers and Cosmologists were understanding the bigger picture. This effort ended with a system of matter particles interacting through four fundamental forces: the electromagnetic, the weak and strong nuclear forces, and gravitation. The first three are currently understood as quantum gauge theories inside the SM. The fourth one is still not quantized due to the high energies required to see quantum effects in the weak gravitational interaction.

Now, as particle physicists, it is our time to keep probing smaller scales, to try to understand the fundamental blocks that create our universe. This is a monumental task that requires the involvement of thousands of physicists and enormous machines. The style of experiment in particle physics today is a scale-up version of the one Geiger and Marsden did under the supervision of Rutherford during the first decade of the 20th century. It involved colliding alpha particles from a radioactive source into a thin gold foil. Today, we keep colliding particles to understand their basic properties, just at a larger scale. The biggest of these machines is the **Large Hadron Collider** (LHC). It collides bunches of particles with a center of mass energies of 14 TeV, which allows us to probe distances of about 10^{-20} m. It was designed to discover the final missing piece in the SM, the Higgs boson, which was successfully found in the year 2012 [\[1,2\]](#).

There is a major experimental effort involved in building, maintaining, and analyzing the data from the LHC, which to be compared to our theories, needs an equivalent effort on the theoretical side. The calculations needed to compare with the experimental data, at the current precision, are a complicated, multi-step, process that requires the use of fundamental theories, like the SM, together with phenomenological models. Our main tool

to calculate observable quantities from scattering experiments, like the ones done at the LHC, is **perturbation theory**. However, a theoretical complication appears involving one property of non-Abelian gauge theories, like the ones forming the SM, called confinement. The strong interaction is much stronger at small energy scales, which makes perturbation theory not well suited to study this interaction when the interaction energies are small. Moreover, when colored particles are involved in the collision, like the ones inside the hadrons colliding at the LHC, the radiation from the strong interaction at small energies creates a high multiplicity final-state, sometimes involving hundreds of particles. We can overcome these difficulties by splitting the calculations into different parts, depending on the typical energy scale of each piece. Using phenomenological models to describe the low energy parts and perturbation theory for the high energy component. Currently, these calculations are performed with computer programs, **Monte Carlo event generators** (MC), that can create events from the theoretical models. The events from the MC can be directly compared with the observed experimental measurements once the detector effects are taken into account.

Moreover, with the discovery of the Higgs particle, all the components making the SM have been found. Now, the experimental effort is focused on precisely measuring the parameters involving these particles, to find any deviation from the SM predictions, and in searching new physics; directly, through the detection of a new particle, or indirectly, through the effects that the inaccessible particles will have on the current measurements. Those indirect detections will need high accuracy predictions and measurements. It will mean better phenomenological models with higher accuracy and, at the same time, higher-order calculations in perturbation theory. The state-of-the-art are **next-to-leading order** (NLO) calculations¹ together with parton showers, QCD radiation added to the fixed-order calculation, and hadronization models. On the other hand, we will also need tools to classify possible deviations from the SM predictions. It is accomplished systematically with **Effective Field Theories**, theories that include the effects due to the high energy particles on the degrees of freedom that are accessible and respect the symmetries of the low energy theory.

In this thesis, we are going to describe a large set of the physics needed to create theoretical results that could be compared with experiments like the LHC. The thesis will be divided into three main chapters, excluding the introduction, the conclusions, and the summary in the Valencian language.

In chapter 2, we will start with a review of the theory used to make these calculations, the SM. We will briefly explain the concept of an Effective Field Theory and list the effective operators of dimension-6 and dimension-8 involving vector bosons and the Higgs particle. Next, the tools needed to perform calculations for the LHC will be presented. A brief description of the different experiments will be given and notation related to the coordinates used in a particle detector setting introduced. Ensuing with the introduction of the parton model, which describes colored particles with fractional charge forming hadrons, like the proton and the pions. The parton model is an approximation, the hadron content will be fundamentally described by QCD, but it allows us to factorize the cross-section into separate pieces involving different energy scales. The high energy component in this factorization will be calculated using perturbation theory. A description of how it is done at NLO will follow. A dedicated section is then given to the infrared and collinear singularities and the different ways to regularize them. Finally, how parton showers are implemented and some basic concepts about Monte Carlo integration are explained.

Chapter 3 will be dedicated to di-photon production with two jets in the **vector boson**

¹For selected processes higher-order corrections are currently known.

scattering (VBS) approximation. After a brief introduction, explaining the components and importance of the process, we will give a detailed exposition of the implementation of the process at NLO QCD in the parton level Monte Carlo VBFNLO. The exposition will be divided into four different subsections. Details about the different subroutines used to construct the Feynman diagrams will be introduced at the same time as the LO amplitude is assembled, which will serve as an example of how to use them. Then, we will explain the implementation of the real contribution together with the Catani-Seymour dipoles needed to remove the infrared and collinear singularities. Next, the virtual contributions will be described. This process receives vertex, box, and pentagon corrections. The vertex correction will be explicitly calculated. The process implementation will end with the anomalous couplings. The following section will focus on the checks performed to ensure the correct implementation of the process. The chapter will end with a phenomenological analysis of the process using our implementation. We will analyze the cuts involved in the VBS approximation, and we will compare our results with similar VBS processes. Subsequently, the phenomenologically relevant differential distributions of the process are shown, which will give us an idea of the process shape and the effects of the NLO correction. We will include in the analysis the QCD channel with the same final-state particles which will be used as our main background. Finally, to show the potential of our implementation to use anomalous couplings, the invariant distribution of the two-photon system with two different values of an anomalous operator is presented.

In chapter 4, the implementation of an interface for di-boson and tri-boson production that will allow the communication between VBFNLO and the MC event generator Herwig is shown. While VBFNLO generates partonic cross-sections at NLO QCD and allows the implementation of anomalous couplings; the implementation of parton showers, hadronization models, and multi-particle interactions are obtained with event generators, like Herwig. The interface allows taking advantage of the benefits provided by both programs. After a brief introduction, the implementation of the interface, which will be divided into different parts depending on the phase of the event generation, is presented. Then, some checks performed to guarantee the correct implementation of the interface are shown. The chapter ends with a phenomenological analysis of a couple of tri-boson production processes including the scale variation uncertainties of a group of selected observables, and the effect of cut migration due to the parton shower for the Frixione isolation cut.

Finally, in chapter 5, a summary of the results obtained is presented and, in chapter 6, a summary of the thesis is given in Valencian language.

Chapter 2

Theoretical Background

2.1 The Standard Model

In this section, the most important concepts of the Standard Model (SM) are presented. The reader is referred to standard textbooks for a more detailed introduction Refs. [3-5] or to Ref. [6] for a more advanced treatment. The following exposition follows closely the book by Schwartz [5].

Our most fundamental, current understanding of particle physics is given by the **Standard Model** (SM). In nature, four different interactions have been discovered; the electromagnetic, the strong and weak nuclear forces, and gravitation. The Standard Model allows us to make extremely precise predictions for three of these four forces, i.e., the current best theoretical prediction of the electron's anomalous electric dipole moment matches its experimental counterpart in 9 significant digits [7-9].

The Standard Model is an example of a **non-Abelian gauge theory**, which is a generalization of the Maxwell theory of electromagnetism. The gauge theory Lagrangian is given by terms that are invariant under certain local continuous transformations, which in the case of electromagnetism is local phase invariance. Symmetry transformations are mathematically represented by group elements. In the case of continuous transformations, these groups are called **Lie groups**, groups which are also differentiable manifolds. The group elements continuously connected to the identity can be written as

$$U(\theta) = \exp(i\theta^a T^a),$$

where T^a are a set of matrices, θ^a real numbers, and a an integer index that runs from 1 to d_G , where d_G is the group's **dimension**. The T^a are called the **generators** of the Lie group, and they form a **Lie algebra**, which means that there is a defined product, the **Lie bracket**, for which the set is closed:

$$[T^a, T^b] = i f^{abc} T^c, \tag{2.1}$$

the i in this equation is conventional, and the f^{abc} are called structure constants. The number of generators gives the dimension of the group. The product on Eq. (2.1) must also obey the Jacobi identity

$$[A, [B, C]] + [B, [C, A]] + [C, [A, B]] = 0,$$

which is automatically satisfied for matrices if the Lie bracket is defined as the commutator. The normalization of the generators is not fixed in Eq. (2.1). In physics, we usually normalize the structure constants so

$$f^{acd} f^{bcd} = N \delta^{ab}. \tag{2.2}$$

Restricting the discussion to finite-dimensional **simple** Lie algebras, there is only a few possibilities. The groups can be $SO(N)$, $SU(N)$, and $Sp(N)$, which respectively preserve the N-dimensional real, complex and quaternionic inner products, or one of the five exceptional groups G_2 , F_4 , E_6 , E_7 , E_8 .

Hereafter, the representations of $SU(2)$ and $SU(3)$ will be studied. While $SU(2)$ is extensively analyzed in any Quantum Mechanics course, because it represents actions on the particle spins, it is also an SM gauge group together with $SU(3)$ and $U(1)$.

The smallest non-trivial representation of any group is called **fundamental representation**. The fundamental representation of $SU(2)$ is given by

$$T^a = \frac{\sigma^a}{2},$$

where σ^a are the **Pauli matrices**:

$$\sigma^1 = \begin{pmatrix} 0 & 1 \\ 1 & 0 \end{pmatrix}, \quad \sigma^2 = \begin{pmatrix} 0 & -i \\ i & 0 \end{pmatrix}, \quad \sigma^3 = \begin{pmatrix} 1 & 0 \\ 0 & -1 \end{pmatrix},$$

which satisfy $[T^a, T^b] = i\epsilon^{abc}T^c$, meaning its structure functions are $f^{abc} = \epsilon^{abc}$. In the case of $SU(3)$, an equivalent set of matrices λ^a , such that $T^a = \lambda^a/2$ is given by eight 3×3 matrices, called **Gell-Mann matrices**.

$$\begin{aligned} \lambda^1 &= \begin{pmatrix} 0 & 1 & \\ 1 & 0 & \\ & & 0 \end{pmatrix}, & \lambda^2 &= \begin{pmatrix} 0 & -i & \\ i & 0 & \\ & & 0 \end{pmatrix}, & \lambda^3 &= \begin{pmatrix} 1 & & \\ & -1 & \\ & & 0 \end{pmatrix}, \\ \lambda^4 &= \begin{pmatrix} & & 1 \\ & 0 & \\ 1 & & \end{pmatrix}, & \lambda^5 &= \begin{pmatrix} & & -i \\ & 0 & \\ i & & \end{pmatrix}, & \lambda^6 &= \begin{pmatrix} & & \\ & 0 & 1 \\ & 1 & 0 \end{pmatrix}, \\ \lambda^7 &= \begin{pmatrix} & & \\ & 0 & -i \\ & i & 0 \end{pmatrix}, & \lambda^8 &= \frac{1}{\sqrt{3}} \begin{pmatrix} 1 & & \\ & 1 & \\ & & -2 \end{pmatrix}. \end{aligned}$$

These matrices generate the transformations of the fermions in the theory while the gauge bosons transform under the **adjoint representation**.

The different representations can be characterized independently of the basis through the **quadratic Casimir** operator, $T^a T^a$. **Schur's lemma** states that any group element that commutes with all the other group elements in an irreducible representation must be proportional to the identity. The quadratic Casimir, $T^a T^a$, commuting with all the generators T^b :

$$\begin{aligned} [T^a T^a, T^b] &= T^a [T^a, T^b] + [T^a, T^b] T^a \\ &= T^a (i f^{abc} T^c) + (i f^{abc} T^c) T^a = i f^{abc} \{T^c, T^a\} = 0, \end{aligned}$$

allows us to write, by Schur's lemma,

$$T^a T^a = C_R 1.$$

In any representation, we can write

$$\text{tr}(T^a T^b) = T_R \delta^{ab}, \quad (2.3)$$

where the T_R is called the **index** of the representation, which can be used to find the values of C_R in different representations. In the fundamental and adjoint representations, they are given by:

$$T_F = \frac{1}{2}, \quad T_A = N.$$

To calculate the quadratic Casimir, one takes $a = b$ in Eq. (2.3), and sum over a , which yields

$$\text{tr}(T^a T^a) = C_R \text{tr}(1) = C_R d_R = T_R d_G.$$

Using $d_F = N$, $d_A = N^2 - 1$, $d_G = N^2 - 1$, the quadratic Casimir in the fundamental and adjoint representations are given by

$$C_F = \frac{N^2 - 1}{2N}, \quad C_A = N.$$

In order to obtain an invariant $SU(N)$ Lagrangian, following the same strategy that in electromagnetism, partial derivatives are converted into covariant ones given by

$$D_\mu = \partial_\mu - ig A_\mu^a T^a,$$

where A_μ^a transforms under $SU(N)$ transformations as

$$A_\mu^a \rightarrow A_\mu^a + \frac{1}{g} \partial_\mu \alpha^a - f^{abc} \alpha^b A_\mu^c.$$

Since $[D_\mu, D_\nu]$ is not an operator but a function, we can define $F_{\mu\nu}$ as

$$F_{\mu\nu} \equiv \frac{i}{e} [D_\mu, D_\nu].$$

So that

$$F_{\mu\nu} = \partial_\mu A_\nu^a - \partial_\nu A_\mu^a + g f^{abc} A_\mu^b A_\nu^c,$$

which effectively reduces to the electromagnetic field strength tensor in the Abelian case, where $f^{abc} = 0$. Thus, the only gauge-invariant Lagrangian with **renormalizable interactions** is

$$\mathcal{L} = -\frac{1}{4} F_{\mu\nu}^a F^{a\mu\nu} + \bar{\psi}(i\not{D} - m_\psi)\psi,$$

except for one extra renormalizable, gauge-invariant possible term

$$\mathcal{L}_\theta = \theta \epsilon^{\mu\nu\alpha\beta} F_{\mu\nu}^a F_{\alpha\beta}^a = 2\theta \partial_\mu \left(\epsilon^{\mu\nu\alpha\beta} A_\nu^a F_{\alpha\beta}^a \right),$$

where θ is a real number. Experimentally θ is compatible with zero [10-12], which is known as the **strong CP-problem**.

Given the gauge symmetry group under which our theory must be invariant, we are now able to write the most general, renormalizable, Lagrangian. In particular, the SM is the quantization of the non-Abelian gauge theory invariant under the gauge group

$$\underbrace{SU(3)_C}_{QCD} \otimes \underbrace{SU(2)_L \otimes U(1)_Y}_{EW}$$

where the C, L, and Y are the color, flavor, and hypercharge quantum numbers.

2.1.1 Quantum Chromodynamics

The quantized version of the non-Abelian $SU(3)_C$ gauge theory, which is one of the pieces of the SM, is known as Quantum Chromodynamics. The quantization of this theory requires dealing with certain subtleties. For example, it is known that insisting in Lorentz covariance and gauge invariance propagates non-physical degrees of freedom; spin-1, zero mass particles, have two degrees of freedom, but they are described covariantly by four-vectors, with 4 degrees of freedom. The contribution from the spurious degrees of freedom is removed with Faddeev-Popov ghosts [13], which are non-physical scalar particles with fermionic statistics (violating the spin-statistics theorem). Adding the Faddeev-Popov ghost and gauge fixing with R_ξ -gauges, the Lagrangian then becomes

$$\mathcal{L} = -\frac{1}{4}F_{\mu\nu}^a F^{a\mu\nu} + \bar{\psi}(i\not{D} - m_\psi)\psi - \frac{1}{2\xi}(\partial_\mu A_\mu^a)^2 + (\partial_\mu \bar{c}^a)(\delta^{ac}\partial_\mu + g f^{abc} A_\mu^b)c^c, \quad (2.4)$$

from where the Feynman rules can be deduced (see Ref. [14] for example).

The vertices are derived expanding the covariant derivatives in Eq. (2.4), and the interaction part of the Lagrangian reads

$$\begin{aligned} \mathcal{L}_{int} = & -g f^{abc}(\partial_\mu A_\nu^a)A_\mu^b A_\nu^c - \frac{1}{4}g^2(f^{eab}A_\mu^a A_\nu^b)(f^{ecd}A_\mu^c A_\nu^d) \\ & + g f^{abc}(\partial_\mu \bar{c}^a)A_\mu^b c^c + g A_\mu^a \bar{\psi}_i \gamma^\mu T_{ij}^a \psi_j. \end{aligned} \quad (2.5)$$

The fermion-gluon interacting term after renormalization, using dimensional regularization, is given by

$$\mathcal{L} = \mu^{\frac{4-d}{2}} g_R \frac{Z_1}{Z_2 \sqrt{Z_3}} A_\mu^{a(0)} \bar{\psi}_i^{(0)} \gamma^\mu T_{ij}^a \psi_j^{(0)},$$

where the (0) superscripts indicate that these are bare quantities. The bare coupling as a function of the renormalization constants is written by

$$g_0 = g_R \frac{Z_1}{Z_2 \sqrt{Z_3}} \mu^{\frac{4-d}{2}},$$

where the μ is a mass dimension scale that appears during renormalization in order to maintain the Lagrangian mass dimension. Since the bare Lagrangian did not depend on this scale, the g_0 does not either, and, we obtain

$$0 = \mu \frac{d}{d\mu} g_0 = \mu \frac{d}{d\mu} \left[g_R \frac{Z_1}{Z_2 \sqrt{Z_3}} \mu^{\frac{4-d}{2}} \right], \quad (2.6)$$

which is called the **renormalization group equation** (RGE). The beta function is defined by

$$\beta(g_R) \equiv \mu \frac{d}{d\mu} g_R.$$

Expanding perturbatively at $\mathcal{O}(g_R^2)$, and using Eq. (2.6), we obtain in dimensional regularization

$$\beta(g_R) = -\frac{\epsilon}{2} g_R + \frac{\epsilon}{2} g_R^2 \frac{\partial}{\partial g_R} \left(\delta_1 - \delta_2 - \frac{1}{2} \delta_3 \right). \quad (2.7)$$

The values of the counterterms at 1-loop in R_ξ -gauges are

$$\begin{aligned}\delta_1 &= \frac{1}{\epsilon} \left(\frac{g^2}{16\pi^2} \right) \left[-2C_F - 2C_A + 2(1-\xi)C_F + \frac{1}{2}(1-\xi)C_A \right], \\ \delta_2 &= \frac{1}{\epsilon} \left(\frac{g^2}{16\pi^2} \right) [-2C_F + 2(1-\xi)C_F], \\ \delta_3 &= \frac{1}{\epsilon} \left(\frac{g^2}{16\pi^2} \right) \left[\frac{10}{3}C_A - \frac{8}{3}n_f T_F + (1-\xi)C_A \right].\end{aligned}$$

Using these counterterms in Eq. (2.7), we get

$$\beta(g_R) = -\frac{\epsilon}{2}g_R - \frac{g_R^3}{16\pi^2} \left[\frac{11}{3}C_A - \frac{4}{3}n_f T_F \right].$$

With $\beta_0 = 11/3C_A - 4/3n_f T_F$ and $\alpha_s = g_s^2/4\pi$, we obtain the differential equation

$$\mu \frac{d}{d\mu} \alpha_s = -\frac{\alpha_s^2}{2\pi} \beta_0,$$

which can be solved for α_s

$$\alpha_s(\mu) = \frac{2\pi}{\beta_0} \frac{1}{\ln \frac{\mu}{\Lambda_{QCD}}}, \quad (2.8)$$

where Λ_{QCD} is the value of μ for which α_s goes to infinity.

A couple of crucial facts about the strong interaction can be inferred from Eq. (2.8). If we set the values of $C_A = 3$, $N = 3$, $n_f = 6$, and $\epsilon = 0$, β_0 is equal to 7 and $\alpha_s(\mu)$ decreases with increasing μ . This fact is known as asymptotic freedom [15, 16], which explains why we can treat partons as free particles inside the proton. In Fig. 2.1, we can see the values of α_s at different scales obtained from various experiments. The increasing of $\alpha_s(\mu)$ for small values of μ points to the experimentally observed property of confinement.

2.1.2 Electroweak Model

The other two interactions included in the SM, the electromagnetic and weak nuclear forces, are described by the Weinberg-Glashow-Salam model [18-20],

$$SU(2)_L \times U(1)_Y \rightarrow U(1)_{EM}.$$

The model unifies both interactions with a Lagrangian invariant under the gauge group $SU(2)_L \times U(1)_Y$ broken by the vacuum of the theory into the $U(1)_{EM}$; a process known as **Spontaneous Symmetry Breaking** (SSB). The vector bosons of the broken symmetries acquire masses through the Higgs-Englert-Brout mechanism [21, 23]. In what follows, we briefly recount the electroweak model.

In the Weinberg-Glashow-Salam model, the symmetry is broken by the **vacuum expectation value** (vev) of a scalar $SU(2)_L$ doublet with $Y = 1/2$, the **Higgs multiplet**, Φ . The Lagrangian of the EW theory is

$$\mathcal{L} = -\frac{1}{4}(W_{\mu\nu}^a)^2 - \frac{1}{4}B_{\mu\nu}^2 + (D_\mu \Phi)^\dagger (D_\mu \Phi) + m_h^2 \Phi^\dagger \Phi - \lambda(\Phi^\dagger \Phi)^2, \quad (2.9)$$

where the covariant derivative acting on the Higgs multiplet is

$$D_\mu \Phi = \partial_\mu \Phi - igT^a W_\mu^a \Phi - \frac{1}{2}ig' B_\mu \Phi, \quad (2.10)$$

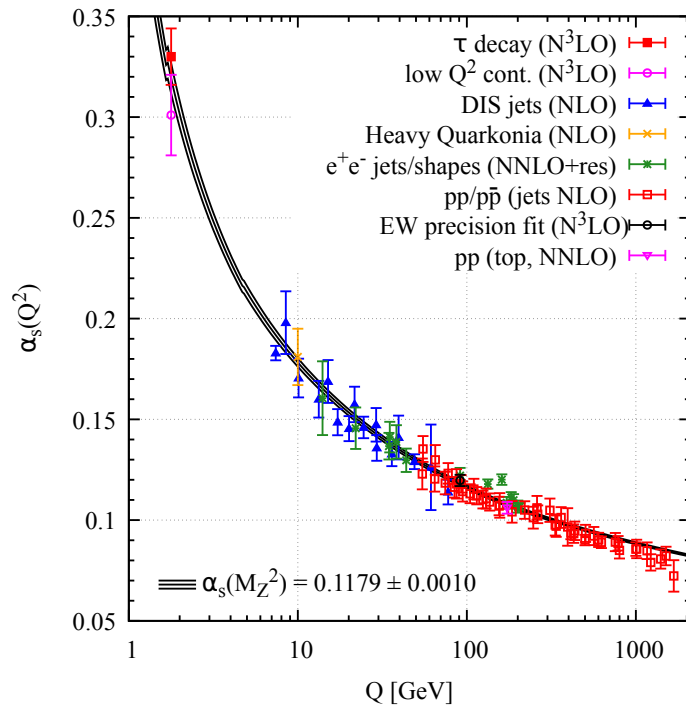


Figure 2.1: Set of measurements of α_s as a function of the energy scale Q . Source Ref. [17].

and the **Higgs potential** is

$$V(\Phi) = -m_h^2 |\Phi|^2 + \lambda |\Phi|^4.$$

The particle spectrum is given by the field excitations around a true minimum. To write the Lagrangian as a function of these excitations, the Higgs multiplet is expanded around the minimum of the potential as

$$\Phi = \exp\left(2i\frac{\pi^a T^a}{v}\right) \begin{pmatrix} 0 \\ \frac{v}{\sqrt{2}} + \frac{h}{\sqrt{2}} \end{pmatrix}, \quad (2.11)$$

where v is the Higgs vev. The $SU(2)_L$ gauge invariance allows us to use the so-called **unitary gauge**, where the Higgs multiplet is real, $\pi^a = 0$. Replacing Eq. (2.11) in unitary gauge into the Lagrangian of Eq. (2.9), the mass terms for the vector bosons and interactions between the vector bosons and a scalar field h , called the **Higgs field**, are obtained.

The physical fields are not the ones that transform under $SU(2)_L \times U(1)_Y$, but the ones defined as follows. The charged W^\pm bosons are given by the linear combination

$$W_\mu^\pm \equiv \frac{1}{\sqrt{2}}(W_\mu^1 \mp iW_\mu^2). \quad (2.12)$$

While the neutral bosons are rotated like

$$\begin{pmatrix} Z_\mu \\ A_\mu \end{pmatrix} \equiv \begin{pmatrix} \cos \theta_W & -\sin \theta_W \\ \sin \theta_W & \cos \theta_W \end{pmatrix} \begin{pmatrix} W_\mu^3 \\ B_\mu \end{pmatrix}, \quad (2.13)$$

where θ_W is the electroweak angle, sometimes called Weinberg angle. If we expand the covariant derivative terms of the Higgs multiplet in unitary gauge and use Eq. (2.12), and

Eq. (2.13), the coefficients accompanying the quadratic terms of the Lagrangian define the following masses for the physical vector bosons

$$\begin{aligned} m_A &= 0, \\ m_W &= \frac{v}{2}g, \\ m_Z &= \frac{1}{2\cos\theta_w}gv = \frac{v}{2}\sqrt{g^2 + g'^2} = \frac{m_W}{\cos\theta_w}. \end{aligned}$$

There are three different **generations** of fermions in the SM, and only the left-handed components transform under the fundamental representation of $SU(2)_L$ like

$$L^i = \begin{pmatrix} \nu_{eL} \\ e_L \end{pmatrix}, \begin{pmatrix} \nu_{\mu L} \\ \mu_L \end{pmatrix}, \begin{pmatrix} \nu_{\tau L} \\ \tau_L \end{pmatrix}, \quad Q^i = \begin{pmatrix} u_L \\ d_L \end{pmatrix}, \begin{pmatrix} c_L \\ s_L \end{pmatrix}, \begin{pmatrix} t_L \\ b_L \end{pmatrix}.$$

The right-handed components are singlets under $SU(2)_L$ but charged under $U(1)_Y$

$$\begin{aligned} e_R^i &= \{e_R, \mu_R, \tau_R\} \\ u_R^i &= \{u_R, c_R, t_R\}, \quad d_R^i = \{d_R, s_R, b_R\}. \end{aligned}$$

The covariant derivatives appearing in the fermionic Lagrangian, $i\bar{f}\not{D}_\mu f$, are given by

$$\begin{aligned} D_\mu &= \partial_\mu - igW_\mu^3 T^3 - ig'B_\mu Y \\ &= \partial_\mu - ieA_\mu(T^3 + Y) - ieZ_\mu(\cot\theta_W T^3 - \tan\theta_W Y), \end{aligned}$$

for left-handed particles and by

$$\begin{aligned} D_\mu &= \partial_\mu - ig'B_\mu Y \\ &= \partial_\mu - ieY(A_\mu - \tan\theta_W Z_\mu), \end{aligned}$$

for right-handed particles. From the coefficient accompanying the photon in the covariant derivatives, which is the electric charge, a relation between the $SU(2)_L \times U(1)_Y$ quantum numbers and the electric charge can be found, and it is given by

$$Q = T^3 + Y.$$

In the right-handed case $T^3 = 0$ and $Q = Y$.

The Dirac fermion mass terms are of the form $f_L f_R + f_R f_L$. These terms are not invariant under $SU(2)_L$ transformations, so Dirac fermion masses are in principle forbidden in the SM Lagrangian. This problem is solved through the Higgs multiplet by introducing **Yukawa interaction terms** like

$$\mathcal{L}_{Y,e} = -y\bar{L}H e_R + h.c., \quad (2.14)$$

which are $SU(2)_L$ invariant. Using as a basis the excitation of the H multiplet from the vacuum in the unitary gauge, there appear mass terms proportional to the vacuum expectation value of the Higgs.

$$\mathcal{L}_{mass,e} = -\frac{yv}{\sqrt{2}}\bar{e}_L e_R + h.c.,$$

and the lepton masses are $m_e = \frac{yv}{\sqrt{2}}$.

For the quarks, we introduce similar terms

$$\mathcal{L}_{Y,q} = -Y_{ij}^d \bar{Q}^i H d_R^j - Y_{ij}^u \bar{Q}^i \tilde{H} d_R^j + h.c., \quad (2.15)$$

where $\tilde{H} \equiv i\sigma_2 H^*$. The mass terms are given by

$$\mathcal{L}_{Y,q} = -\frac{v}{\sqrt{2}} Y_{ij}^d \bar{d}_L^i H d_R^j - \frac{v}{\sqrt{2}} Y_{ij}^u \bar{u}_L^i \tilde{H} d_R^j + h.c..$$

The non-diagonal $Y_{ij}^{d,u}$ are called **Yukawa matrices**. The Yukawa matrices can be diagonalized using

$$Y_d = U_d M_d K_d^\dagger, \quad Y_u = U_u M_u K_u^\dagger,$$

where $U_{d,u}$ and $K_{d,u}$ are two sets of unitary matrices and $M_{d,u}$ are diagonal mass matrices. The quark rotation $d_R \rightarrow K_d d_R$, $u_R \rightarrow K_u u_R$, $d_L \rightarrow U_d d_L$, $u_L \rightarrow U_u u_L$, leaves all the same-flavor terms untouched, but it introduces a flavor-mix in the flavor changing charged currents,

$$V \equiv U_u^\dagger U_d.$$

This matrix is known as the **Cabibbo-Kobayashi-Maskawa** (CKM) matrix. Since the CKM matrix is non-diagonal, the charged currents mix different quark generations. However, the off-diagonal terms are small and in some cases can be neglected. Furthermore, the CKM matrix is a complex matrix which implies the existence of CP-violation [24, 25].

2.2 Effective Field Theory

The SM is a **renormalizable theory**, which means that to make predictions at any order in perturbation theory, we only need to fix experimentally a finite number of parameters. A theory is renormalizable if the coefficients accompanying the operators have positive mass dimensions. Because the mass dimension of the Lagrangian has to be 4, i.e. the action has to be dimensionless, the maximum allowed dimension for the operators in a renormalizable Lagrangian is 4.

In an Effective Field Theory approach, we consider all operators, independently of their mass dimension, that are consistent with a given set of symmetries. Effective Field Theories are usually non-renormalizable, which means that for higher order predictions, the number of parameters fixed by the experiment increases.

The **Standard Model Effective Field Theory** (SMEFT) has the EW symmetries of the SM, $SU(2)_L \times U(1)_Y \rightarrow U(1)_{EM}$, spontaneously broken by the Higgs vev, but has operators of arbitrary mass dimension. The Lagrangian of the SMEFT is given by

$$\mathcal{L}_{SMEFT} = \mathcal{L}_{SM} + \sum_{d=5}^{\infty} \frac{f_i^{(d)}}{\Lambda^{d-4}} \mathcal{O}_i^{(d)},$$

where the Λ is a mass dimension parameter that indicates the energy scale of the given parameter, i.e. the possible scale of new physics. The $f_i^{(d)}$ are dimensionless parameters usually called **Wilson coefficients**, and $\mathcal{O}_i^{(d)}$ are any operators of mass dimension d compatible with the SM symmetries.

Hereafter, we only consider operators involving exclusively the electroweak vector bosons, the Higgs, and operators of dimension 6 or 8. The following simplification in the notation is used

$$\begin{aligned} \widehat{W}_{\mu\nu} &= igT^a W_{\mu\nu}, \\ \widehat{B}_{\mu\nu} &= ig'Y B_{\mu\nu}. \end{aligned}$$

The covariant derivative Eq. (2.10) is then written as

$$D_\mu = \partial_\mu + \widehat{W}_{\mu\nu} + \widehat{B}_{\mu\nu}.$$

Dimension-6 operators

The dimension-6 operators [26-30] are divided into CP-even operators or CP-odd operators, with the CP-even operators given by

$$\begin{aligned}\mathcal{O}_W &= (D_\mu \Phi)^\dagger \widehat{W}^{\mu\nu} (D_\nu \Phi), \\ \mathcal{O}_B &= (D_\mu \Phi)^\dagger \widehat{B}^{\mu\nu} (D_\nu \Phi), \\ \mathcal{O}_{WWW} &= \text{Tr} \left(\widehat{W}_{\mu\nu} \widehat{W}^{\nu\rho} \widehat{W}_\rho^\mu \right), \\ \mathcal{O}_{WW} &= \Phi^\dagger \widehat{W}_{\mu\nu} \widehat{W}^{\mu\nu} \Phi, \\ \mathcal{O}_{BB} &= \Phi^\dagger \widehat{B}_{\mu\nu} \widehat{B}^{\mu\nu} \Phi.\end{aligned}$$

The CP-odd operators, with the **Hodge dual** tensor defined by $\widetilde{T}^{\mu\nu} = \frac{1}{2} \epsilon^{\mu\nu\rho\sigma} T_{\rho\sigma}$, for $\widehat{W}_{\mu\nu}$ and $\widehat{B}_{\mu\nu}$ are

$$\begin{aligned}\mathcal{O}_{\widetilde{W}} &= (D_\mu \Phi)^\dagger \widetilde{\widehat{W}}^{\mu\nu} (D_\nu \Phi), \\ \mathcal{O}_{\widetilde{B}} &= (D_\mu \Phi)^\dagger \widetilde{\widehat{B}}^{\mu\nu} (D_\nu \Phi), \\ \mathcal{O}_{\widetilde{WWW}} &= \text{Tr} \left(\widetilde{\widehat{W}}_{\mu\nu} \widehat{W}^{\nu\rho} \widehat{W}_\rho^\mu \right), \\ \mathcal{O}_{\widetilde{WW}} &= \Phi^\dagger \widetilde{\widehat{W}}_{\mu\nu} \widehat{W}^{\mu\nu} \Phi, \\ \mathcal{O}_{\widetilde{BB}} &= \Phi^\dagger \widetilde{\widehat{B}}_{\mu\nu} \widehat{B}^{\mu\nu} \Phi, \\ \mathcal{O}_{D\widetilde{W}} &= \text{Tr} \left([D_\mu, \widetilde{\widehat{W}}_{\nu\rho}] [D^\mu, \widehat{W}^{\nu\rho}] \right), \\ \mathcal{O}_{B\widetilde{W}} &= \Phi^\dagger \widehat{B}_{\mu\nu} \widetilde{\widehat{W}}^{\mu\nu} \Phi.\end{aligned}$$

Among these operators, there are only four linearly independent since there are relations between them. For example $\mathcal{O}_{\widetilde{W}}$, $\mathcal{O}_{B\widetilde{W}}$, and $\mathcal{O}_{D\widetilde{W}}$ can be written as

$$\begin{aligned}\mathcal{O}_{\widetilde{W}} &= \mathcal{O}_{\widetilde{B}} - \frac{1}{2} \mathcal{O}_{\widetilde{WWW}} + \frac{1}{2} \mathcal{O}_{\widetilde{BB}}, \\ \mathcal{O}_{B\widetilde{W}} &= -2\mathcal{O}_{\widetilde{B}} - \mathcal{O}_{\widetilde{BB}}, \\ \mathcal{O}_{D\widetilde{W}} &= -4\mathcal{O}_{\widetilde{WWW}}.\end{aligned}$$

Dimension-8 operators

The dimension-8 operators [31, 32] are divided into three different categories depending on whether they include only the Higgs, only vector bosons, or both.

- Operators that only include the Higgs boson:

$$\begin{aligned}\mathcal{L}_{S,0} &= \left[(D_\mu \Phi)^\dagger D_\nu \Phi \right] \times \left[(D^\mu \Phi)^\dagger D^\nu \Phi \right], \\ \mathcal{L}_{S,1} &= \left[(D_\mu \Phi)^\dagger D^\mu \Phi \right] \times \left[(D_\nu \Phi)^\dagger D^\nu \Phi \right], \\ \mathcal{L}_{S,2} &= \left[(D_\mu \Phi)^\dagger D_\nu \Phi \right] \times \left[(D^\nu \Phi)^\dagger D^\mu \Phi \right].\end{aligned}$$

- Operators that include the vector and the Higgs bosons:

$$\begin{aligned}\mathcal{L}_{M,0} &= \text{Tr} \left(\widehat{W}_{\mu\nu} \widehat{W}^{\mu\nu} \right) \times \left[(D_\rho \Phi)^\dagger D^\rho \Phi \right], \\ \mathcal{L}_{M,1} &= \text{Tr} \left(\widehat{W}_{\mu\nu} \widehat{W}^{\nu\rho} \right) \times \left[(D_\rho \Phi)^\dagger D^\mu \Phi \right], \\ \mathcal{L}_{M,2} &= \text{Tr} \left(\widehat{B}_{\mu\nu} \widehat{B}^{\mu\nu} \right) \times \left[(D_\rho \Phi)^\dagger D^\rho \Phi \right], \\ \mathcal{L}_{M,3} &= \text{Tr} \left(\widehat{B}_{\mu\nu} \widehat{B}^{\nu\rho} \right) \times \left[(D_\rho \Phi)^\dagger D^\mu \Phi \right], \\ \mathcal{L}_{M,4} &= \left[(D_\mu \Phi)^\dagger \widehat{W}_{\rho\nu} D^\mu \Phi \right] \times \widehat{B}^{\rho\nu}, \\ \mathcal{L}_{M,5} &= \left[(D_\mu \Phi)^\dagger \widehat{W}_{\rho\nu} D^\nu \Phi \right] \times \widehat{B}^{\rho\mu}, \\ \mathcal{L}_{M,5hc} &= \left[(D_\mu \Phi)^\dagger \widehat{W}_{\rho\mu} D^\nu \Phi \right] \times \widehat{B}^{\rho\nu}, \\ \mathcal{L}_{M,6} &= \left[(D_\mu \Phi)^\dagger \widehat{W}_{\rho\nu} \widehat{W}^{\rho\nu} D^\mu \Phi \right], \\ \mathcal{L}_{M,7} &= \left[(D_\mu \Phi)^\dagger \widehat{W}_{\rho\nu} \widehat{W}^{\rho\mu} D^\nu \Phi \right].\end{aligned}$$

- Operators that include only the vector bosons:

$$\begin{aligned}\mathcal{L}_{T,0} &= \text{Tr} \left(\widehat{W}_{\mu\nu} \widehat{W}^{\mu\nu} \right) \times \text{Tr} \left(\widehat{W}_{\rho\sigma} \widehat{W}^{\rho\sigma} \right) \\ \mathcal{L}_{T,1} &= \text{Tr} \left(\widehat{W}_{\rho\nu} \widehat{W}^{\mu\sigma} \right) \times \text{Tr} \left(\widehat{W}_{\mu\sigma} \widehat{W}^{\rho\nu} \right) \\ \mathcal{L}_{T,2} &= \text{Tr} \left(\widehat{W}_{\rho\mu} \widehat{W}^{\mu\sigma} \right) \times \text{Tr} \left(\widehat{W}_{\sigma\nu} \widehat{W}^{\nu\rho} \right) \\ \mathcal{L}_{T,3} &= \text{Tr} \left(\widehat{W}_{\mu\nu} \widehat{W}^{\rho\sigma} \right) \times \text{Tr} \left(\widehat{W}_{\nu\rho} \widehat{W}^{\sigma\mu} \right) \\ \mathcal{L}_{T,4} &= \text{Tr} \left(\widehat{W}_{\mu\nu} \widehat{W}^{\rho\sigma} \right) \times \widehat{B}_{\nu\rho} \widehat{B}^{\sigma\mu} \\ \mathcal{L}_{T,5} &= \text{Tr} \left(\widehat{W}_{\mu\nu} \widehat{W}^{\mu\nu} \right) \times \widehat{B}_{\rho\sigma} \widehat{B}^{\rho\sigma} \\ \mathcal{L}_{T,6} &= \text{Tr} \left(\widehat{W}_{\rho\nu} \widehat{W}^{\mu\sigma} \right) \times \widehat{B}_{\mu\sigma} \widehat{B}^{\rho\nu} \\ \mathcal{L}_{T,7} &= \text{Tr} \left(\widehat{W}_{\rho\mu} \widehat{W}^{\mu\sigma} \right) \times \widehat{B}_{\sigma\nu} \widehat{B}^{\nu\rho} \\ \mathcal{L}_{T,8} &= \widehat{B}_{\mu\nu} \widehat{B}^{\mu\nu} \widehat{B}_{\rho\sigma} \widehat{B}^{\rho\sigma} \\ \mathcal{L}_{T,9} &= \widehat{B}_{\rho\mu} \widehat{B}^{\mu\sigma} \widehat{B}_{\sigma\nu} \widehat{B}^{\nu\rho}\end{aligned}$$

2.3 LHC Physics

The LHC is a complex machine that involves thousands of scientists and engineers; to build it, maintain it and analyze the data that produces. On the other hand, the calculations

needed to be able to compare our theories with the experimental observations are equally challenging, and require a multi-step approach combining heuristic models with first principles.

In this section, a summary of the experiment and the calculations required to compare the theory with the experimental observations are given, focusing on the calculations needed for the rest of the thesis. For more in-depth explanations, we refer the reader to Refs. [33,34].

2.3.1 The experiments

The **Large Hadron Collider** (LHC) is a proton-proton and lead ion collider, located 150 m underground under the France-Switzerland border, near Geneva. It is a 27 km ring of superconducting magnets and accelerator cavities that accelerates proton bunches in two separate beam pipes to near the speed of light. The two pipes meet at four different points where the different experiment detectors are placed. These are ALICE, LHCb, CMS, and ATLAS. ALICE focuses on lead ion collisions to study quark-gluon plasma, LHCb studies CP-properties using b-quark interactions, and ATLAS and CMS are general-purpose detectors. The physics studied in this thesis relates to the latter two.

The detectors are cylinders centered around the collision point, and are built as a set of detector layers with different purposes. A schematic view of the different detector layers is showed in Fig. 2.2. The first is the tracking chamber which allows the reconstruction of the tracks of the charged particles. Powerful electromagnets bend these tracks allowing the experimentalist to reconstruct the charge and mass of the particles. Next, the electromagnetic calorimeter absorbs the electrons, positrons and photons which allows a reconstruction of their energy. The hadron calorimeter does the same for hadrons. Finally, the muon chamber tries to reconstruct the momenta of the muons that go through all the other calorimeters. The neutrinos pass all the detectors without any signal and their reconstruction depends on the value of the missing momentum.

2.3.2 Rapidity and pseudorapidity

In the following, we are going to explain a typical set of coordinates used in hadron colliders. A common choice is the so-called rapidity, y , defined by

$$\Lambda = \begin{pmatrix} \cosh y & \sinh y \\ \sinh y & \cosh y \end{pmatrix}, \quad (2.16)$$

where Λ is a boost in the z -axis, which is chosen to be aligned with the beam pipe. The rapidity has the advantageous property that under two consecutive boosts in the z -direction, it is an additive quantity.

$$\begin{aligned} \Lambda_1 \Lambda_2 &= \begin{pmatrix} \cosh y_1 & \sinh y_1 \\ \sinh y_1 & \cosh y_1 \end{pmatrix} \begin{pmatrix} \cosh y_2 & \sinh y_2 \\ \sinh y_2 & \cosh y_2 \end{pmatrix} \\ &= \begin{pmatrix} \cosh y_1 \cosh y_2 + \sinh y_1 \sinh y_2 & \cosh y_1 \sinh y_2 + \sinh y_1 \cosh y_2 \\ \sinh y_1 \cosh y_2 + \cosh y_1 \sinh y_2 & \cosh y_1 \cosh y_2 + \sinh y_1 \sinh y_2 \end{pmatrix} \\ &= \begin{pmatrix} \cosh (y_1 + y_2) & \sinh (y_1 + y_2) \\ \sinh (y_1 + y_2) & \cosh (y_1 + y_2) \end{pmatrix}. \end{aligned}$$

In high-energy hadron collisions, the particles colliding are the particles that compose the proton, called **partons**. The detectors are situated in the center-of-mass frame of the protons. As will be shown in the next section, the partons only carry a fraction of the

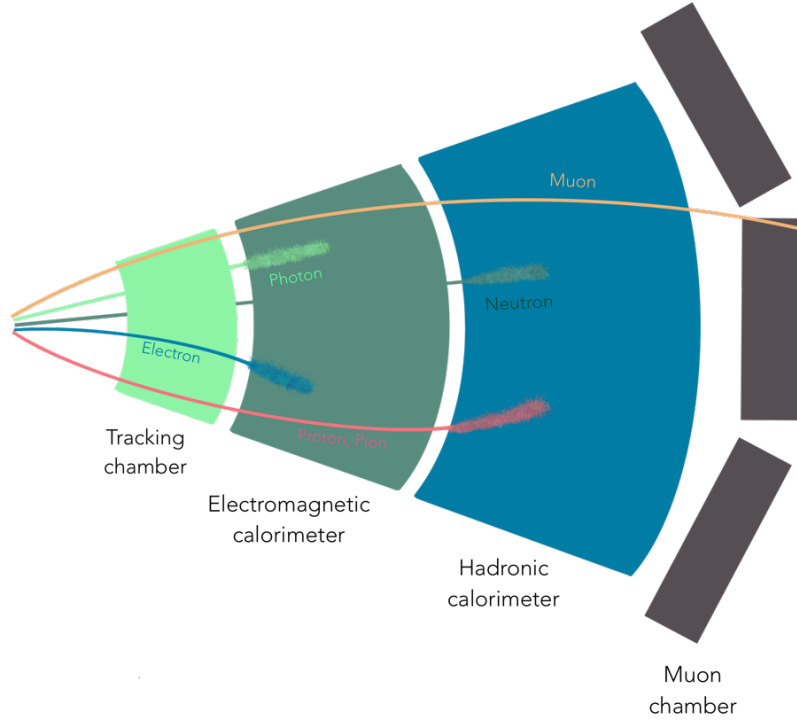


Figure 2.2: ATLAS detector layers.

momentum of the proton, which makes the center-of-mass frame of the parton collision to be boosted in the z -axis.

The matrix transformation representing the Lorentz boost can be written as

$$\Lambda = \begin{pmatrix} \gamma & \gamma\beta \\ \gamma\beta & \gamma \end{pmatrix}, \quad (2.17)$$

where

$$\gamma = \frac{1}{\sqrt{1 - \beta^2}}, \quad \text{and} \quad \beta = \frac{p_z}{E}.$$

Comparing Eq. (2.16) with Eq. (2.17),

$$\cosh y = \frac{e^y + e^{-y}}{2} = \gamma, \quad \text{and} \quad \sinh y = \frac{e^y - e^{-y}}{2} = \gamma\beta,$$

we can solve for y as a function of the momentum's z -component and the energy of the particle,

$$y = \frac{1}{2} \ln \frac{E + p_z}{E - p_z}.$$

For massless particles, $m = 0$,

$$E = |\vec{p}|, \quad \text{and} \quad p_z = |\vec{p}| \cos \theta,$$

thus, the rapidity is a geometrical quantity that only depends on the value of θ ,

$$y = -\ln \tan \left(\frac{\theta}{2} \right).$$

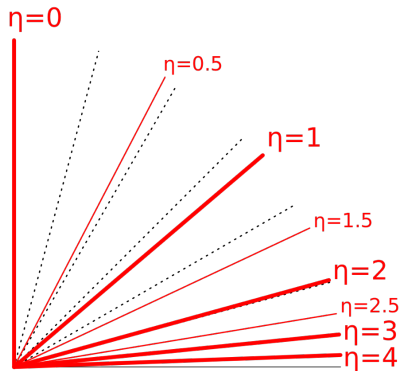


Figure 2.3: Values of the pseudorapidity for a particular set of angles. The pseudorapidity is zero in a perpendicular direction to the beam pipe and approaches infinity when the angle goes to zero.

This motivates the definition of the **pseudorapidity** as

$$\eta \equiv -\ln \tan \left(\frac{\theta}{2} \right),$$

independently of the particle mass. Typical values of the pseudorapidity for different orientations can be seen in Fig. 2.3.

2.3.3 Parton model

The key ingredient to be able to calculate cross-sections in hadron collisions is the ability to split the short from the long distance physics. The high energy collision is assumed to happen between the free components of the proton, called **partons**, Ref. [35]. The long distance physics, which gives the probability of a certain parton to be involved in the collision with a momentum fraction x , can not be perturbatively calculated, and it is encoded into empirically acquired **parton distribution functions** (PDFs), $f_{p/h}(x, \mu_F)$. The hadronic cross-section can be written as

$$\sigma(h_1 h_2 \rightarrow p_1 \dots p_n) = \sum_{a,b} \int_0^1 dx_a dx_b f_{a/h_1}(x_a, \mu_F) f_{b/h_2}(x_b, \mu_F) \hat{\sigma}(ab \rightarrow p_1 \dots p_n). \quad (2.18)$$

The μ_F is called the **factorization scale**, and it marks the boundary between the short and long distance physics. The partonic cross-section $\hat{\sigma}(ab \rightarrow p_1 \dots p_n)$ is given by

$$\hat{\sigma}(ab \rightarrow p_1 \dots p_n) = \frac{1}{2\hat{s}} \int d\Phi_n \overline{\sum_{\substack{\text{spins} \\ \text{colors}}} |\mathcal{M}(p_a, p_b, \Phi_n)|^2}, \quad (2.19)$$

where the phase space, $d\Phi_n$, is given by

$$d\Phi_n = \prod_{i=1}^n \frac{d^4 p_i}{(2\pi)^4} (2\pi) \delta(p_i^2 - m_i^2) \theta(E_i) (2\pi)^4 \delta^4 \left(p_a + p_b - \sum_i p_i \right).$$

The PDFs depend on our choice of the factorization scale, μ_F , but the evolution can be analytically calculated. The initial-state emissions of QCD radiation can be resolved

into final-state particles if the energy and angle of these particles is greater than the experimental resolution, or they can remain unresolved. The boundary between the resolved and unresolved emissions is given by μ_F .

A general property of the scattering amplitudes states that in the **soft-collinear limit**, they factorize into the $n - 1$ particle amplitude and a universal function of the angle and energy of the emitted particle, which for massless particles is given by

$$\lim_{\theta_{in} \rightarrow 0, E_n \rightarrow 0} d\Phi_n |\mathcal{M}(p_a, p_b, \Phi_n)|^2 = d\Phi_{n-1} |\mathcal{M}(p_a, p_b, \Phi_{n-1})|^2 \frac{\alpha_S C_i}{\pi} \frac{d\theta_{in}^2}{\theta_{in}^2} \frac{dE_n}{E_n}, \quad (2.20)$$

where $C_i = C_F, C_A$ depending on whether the emitted particle is a quark or a gluon. The previous result is divergent for $\theta_{in} \rightarrow 0$, called **collinear divergence**, and for $E_n \rightarrow 0$, called **soft divergence**. In this limit, the particles will be unresolved, and they will be part of the non-perturbative PDFs.

The soft-collinear factorization can be used to calculate the evolution of the PDFs when the factorization scale changes, which is given by the **Dokshitzer-Gribov-Lipatov-Altarelli-Parisi** (DGLAP) equations [36–39].

$$\begin{aligned} & \frac{\partial}{\partial \log \mu_F^2} \begin{pmatrix} f_{q/h}(x, \mu_F^2) \\ f_{g/h}(x, \mu_F^2) \end{pmatrix} \\ &= \frac{\alpha_S(\mu_F^2)}{2\pi} \int_x^1 \frac{dz}{z} \begin{pmatrix} P_{qq}\left(\frac{x}{z}\right) & P_{qg}\left(\frac{x}{z}\right) \\ P_{gq}\left(\frac{x}{z}\right) & P_{gg}\left(\frac{x}{z}\right) \end{pmatrix} \begin{pmatrix} f_{q/h}(z, \mu_F^2) \\ f_{g/h}(z, \mu_F^2) \end{pmatrix}, \end{aligned}$$

where the $P_{ij}(x)$ are the **Altarelli-Parisi splitting functions** given by

$$\begin{aligned} P_{qq}(z) &= C_F \left[\frac{1+z^2}{(1-z)_+} + \frac{3}{2} \delta(1-z) \right], \\ P_{qg}(z) &= C_F \left[\frac{1+(1-z)^2}{z} \right], \\ P_{gq}(z) &= T_F [1 - 2z(1-z)], \\ P_{gg}(z) &= 2C_A \left[\frac{z}{(1-z)_+} + \frac{1-z}{z} + z(1-z) \right] \\ &\quad + \delta(1-z) \left(\frac{11}{6} C_A - \frac{2}{3} n_f T_F \right), \end{aligned}$$

which can be calculated perturbatively from the parton splitting diagrams in the soft-collinear limit.

2.3.4 Next-to-Leading-Order QCD Calculations

As explained before, the factorization ansatz, Eq. (2.18), divides the long distance and the short distance physics. The partonic composition of the proton will be encoded into experimentally acquired PDFs, while the hard energy collision between the partons can be calculated using perturbation theory. The reason that perturbation theory can be used to calculate the hard collision is that QCD is asymptotically free. So, the high energy collision will have a small value of α_S which we can use as the variable in our expansion

$$\hat{\sigma} = \hat{\sigma}^{(0)} + \alpha_S \hat{\sigma}^{(1)} + \alpha_S^2 \hat{\sigma}^{(2)} + \dots$$

The leading order (LO) $\hat{\sigma}^{(0)}$ is the cross-section in the Born approximation. The **next-to-leading order** (NLO) cross-section includes the Born approximation and the

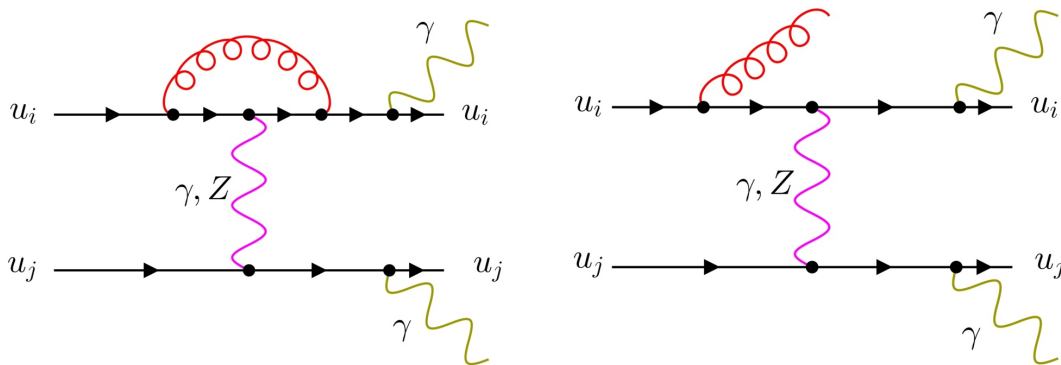


Figure 2.4: Diagrams contributing to the NLO correction. The left diagram shows an example of a loop correction while the right diagram shows an example of a real contribution. Almost all diagrams in this thesis have been drawn with FeynGame, see [40].

cross-section at the next order in α_S

$$\hat{\sigma}^{NLO} = \hat{\sigma}^{(0)} + \alpha_S \hat{\sigma}^{(1)} = \underbrace{\int_n d\hat{\sigma}^B}_{\hat{\sigma}^{(0)}} + \underbrace{\int_n d\hat{\sigma}^V + \int_{n+1} d\hat{\sigma}^R}_{\alpha_S \hat{\sigma}^{(1)}}, \quad (2.21)$$

There are two possible contributions including an extra α_S factor: the interference between the **virtual contribution**, which adds gluon loop between any colored particle, Fig. 2.4 (left), and the Born amplitude, and the amplitude square of the **real contribution** graph given by an extra gluon emission, Fig. 2.4 (right).

Virtual contribution

In the following, a brief explanation of the techniques used to evaluate the virtual corrections is presented. The development of mathematical tools to evaluate loop diagrams is currently at the frontier of the high precision research. Nowadays, one-loop integrals are considered to be solved, although there are difficulties for high multiplicity final-states. We will focus on one of the classical techniques used to evaluate one-loop integrals, the **Passarino-Veltman reduction procedure**. A much broader discussion can be found in Ref. [41], which we will follow in the exposition below.

The partonic cross-section due to the virtual correction can be written as

$$d\hat{\sigma}^V = d\Phi_n \frac{1}{2\hat{s}} \sum_{\substack{\text{spins} \\ \text{colors}}} 2 \text{Re} (\mathcal{M}^B(p_a, p_b, \Phi_n) \mathcal{M}^{*V}(p_a, p_b, \Phi_n, \mu_R)), \quad (2.22)$$

The virtual matrix element, \mathcal{M}^V , appearing in Eq. (2.22) will contain loop diagrams as the one shown in Fig. 2.5. The vertex momenta conserving δ -functions are not enough to specify the loop momentum, so, we will need to solve integrals like

$$I_N \propto \int \frac{d^4\ell}{(2\pi)^4} \frac{\mathcal{N}(\ell)}{(\ell^2 - m_1^2)[(\ell + q_1)^2 - m_2^2] \cdots [(l + q_{N-1})^2 - m_N^2]},$$

where N is the number of external particles entering the loop, and $q_i = \sum_{j=1}^{N-1} p_j$. The numerator, $\mathcal{N}(\ell)$, is a polynomial function in the loop momentum that can also include

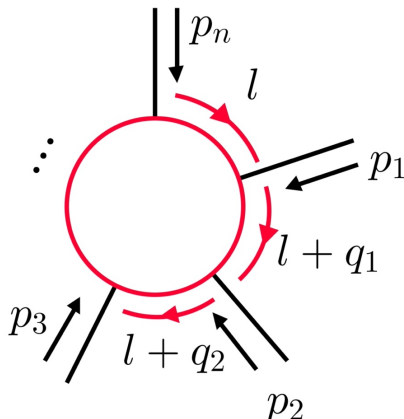


Figure 2.5: Figure of a prototypical loop diagram with n external momenta entering the loop.

external momenta, polarization vectors and other Lorentz and Dirac structures. For the particular case where $\mathcal{N}(\ell) = 1$, the integral I_N will be called a **scalar integral**. The integrals containing a product of r loop momenta are called tensor integrals of rank r .

For large loop momentum, $\ell \rightarrow \infty$, we can ignore all the other constant terms,

$$I_N \sim \int \frac{d^4\ell}{(2\pi)^4} \frac{\mathcal{N}(\ell)}{\ell^{2N}}.$$

The asymptotic behavior of the integral can be deduced from naïve power counting. We can observe that the integral will diverge for large ℓ if the rank of the $\mathcal{N}(\ell)$, r , is $r \geq 2N - 4$. The highest rank for any N -point function in a **renormalizable** quantum field theory is N . Then, the only divergent scalar integrals are the one- and two-point functions. Moreover, the five- and higher-point functions are always **ultraviolet** (UV), meaning for $\ell \rightarrow \infty$, finite.

The UV divergences will be absorbed into the Lagrangian parameters through a **renormalization** thereof. In order to isolate the divergent pieces, we need some **regularization** procedure. A widely used regularization procedure is **dimensional regularization** [42, 43] where the space-time dimension is analytically continued to $d = 4 - 2\epsilon$ with $\epsilon > 0$,

$$\frac{d^4\ell}{(2\pi)^4} \rightarrow \frac{d^d\ell}{(2\pi)^d}.$$

Among the dimensional regularization's properties are the explicit Lorentz and gauge invariance through all the steps, and that the divergences appear as poles in the integral.

If any of the particles involved are massless, there can be another kind of divergences called **soft and collinear divergences** (IRC). These divergences can also be treated using dimensional regularization [44] but with $\epsilon < 0$. For inclusive observables, like the total cross-section, these singularities will cancel when the full NLO contribution is taken into account [45, 47].

In the $d \rightarrow 4$ limit, any I_N can be written as a linear combination of $N \leq 4$ scalar integrals and a finite remainder from the regularization procedure

$$I_N = c_{4;j} I_{4;j} + c_{3;j} I_{3;j} + c_{2;j} I_{2;j} + c_{1;j} I_{1;j} + \mathcal{R} + \mathcal{O}(d - 4),$$

where the $c_{i;j}$ are constant coefficients independent of ϵ . The advantage of this decomposition is that, having tabulated all the $N \leq 4$ scalar integrals [48–51], the calculation is reduced to the determination of the coefficients $c_{i;j}$ and \mathcal{R} .

To achieve the above decomposition, we need to reduce the tensor integrals to scalar ones. The process we are going to use was originally proposed by Passarino and Veltman [43]. The full set of $N \leq 4$ integrals are written, following the notation from Ref. [43] as

$$\begin{aligned} A_0(m_1^2) &= \frac{1}{i\pi^{d/2}} \int d^d \ell \frac{1}{d_1}, \\ B_0, B^\mu, B^{\mu\nu}(p_1^2, m_1^2, m_2^2) &= \frac{1}{i\pi^2} \int d^d \ell \frac{1; \ell^\mu; \ell^\mu \ell^\nu}{d_1 d_2}, \\ C_0, C^\mu, C^{\mu\nu}, C^{\mu\nu\alpha}(p_1^2, p_2^2, p_3^2; m_1^2, m_2^2, m_3^2) &= \frac{1}{i\pi^2} \int d^d \ell \frac{1; \ell^\mu; \ell^\mu \ell^\nu; \ell^\mu \ell^\nu \ell^\alpha}{d_1 d_2 d_3}, \\ D_0, D^\mu, D^{\mu\nu}, D^{\mu\nu\alpha}, D^{\mu\nu\alpha\beta}(p_1^2, p_2^2, p_3^2, p_4^2; s_{12}, s_{23}; m_1^2, m_2^2, m_3^2, m_4^2) \\ &= \frac{1}{i\pi^2} \int d^d \ell \frac{1; \ell^\mu; \ell^\mu \ell^\nu; \ell^\mu \ell^\nu \ell^\alpha \ell^\mu \ell^\nu \ell^\alpha \ell^\beta}{d_1 d_2 d_3 d_4}, \end{aligned}$$

where $d_i = (\ell + \sum_{j=1}^{i-1} p_j)^2 - m_i^2$.

The Passarino-Veltman method is shown by working a particular example, the reduction of the rank one 3-point function to scalar integrals. The C^μ integral transforms as a Lorentz vector. Thus, by Lorentz invariance, it can be written as

$$C^\mu = p_1^\mu C_1 + p_2^\mu C_2, \quad (2.23)$$

since the external momenta are the only Lorentz vectors involved after integrating the loop momenta. Contracting Eq. (2.23) with $p_{1,\mu}$ we get

$$p_{1,\mu} C^\mu = \frac{1}{i\pi^{d/2}} \int d^d \ell \frac{p_1 \cdot \ell}{d_1 d_2 d_3}. \quad (2.24)$$

The scalar product $p_1 \cdot \ell$ appearing in the numerator can be written as a function of the denominators, the external momenta, and the masses,

$$p_1 \cdot \ell = \frac{1}{2}(m_2^2 - m_1^2 - p_1^2 + d_2 - d_1). \quad (2.25)$$

Substituting Eq. (2.25) into Eq. (2.24) allows us to write the contracted integral as a function of scalar integrals

$$\begin{aligned} p_{1,\mu} C^\mu &= \\ &= \frac{1}{2} \left[(m_2^2 - m_1^2 - p_1^2) \underbrace{\frac{1}{i\pi^2} \int d^d \ell \frac{1}{d_1 d_2 d_3}}_{C_0(p_1^2, p_2^2, p_3^2; m_1^2, m_2^2, m_3^2)} + \underbrace{\frac{1}{i\pi^2} \int d^d \ell \frac{1}{d_1 d_3}}_{B_0((p_1+p_2)^2; m_1^2, m_3^2)} - \underbrace{\frac{1}{i\pi^2} \int d^d \ell \frac{1}{d_2 d_3}}_{B_0((p_1+p_2)^2; m_2^2, m_3^2)} \right] \\ &= \frac{1}{2} \left[(m_2^2 - m_1^2 - p_1^2) C_0(p_1^2, p_2^2, p_3^2; m_1^2, m_2^2, m_3^2) + B_0((p_1 + p_2)^2; m_1^2, m_3^2) \right. \\ &\quad \left. - B_0((p_1 + p_2)^2; m_2^2, m_3^2) \right]. \end{aligned}$$

We can proceed analogously to obtain the contracted integral $p_{2,\mu}C^\mu$. With both results, we can use Eq. (2.23) to write the following system of equations

$$\begin{pmatrix} p_{1,\mu}C^\mu \\ p_{2,\mu}C^\mu \end{pmatrix} = \underbrace{\begin{pmatrix} p_1 \cdot p_1 & p_1 \cdot p_2 \\ p_2 \cdot p_1 & p_2 \cdot p_2 \end{pmatrix}}_G \begin{pmatrix} C_1 \\ C_2 \end{pmatrix}.$$

The left-hand side is completely known as a function of the scalar integrals. So to get the coefficients C_1, C_2 , we just have to invert the **Gram matrix** G .

$$\begin{pmatrix} C_1 \\ C_2 \end{pmatrix} = G^{-1} \begin{pmatrix} p_{1,\mu}C^\mu \\ p_{2,\mu}C^\mu \end{pmatrix}.$$

A generalization of the above procedure allow us to recursively reduce any tensor integral to $N \leq 4$ scalar integrals.

The simplicity of the method is not without its drawbacks. There are three main problems that complicate its straightforward application to high multiplicity final-states. First, the number of Feynman diagrams dramatically increases with the number of external particles. Also, the number of terms generated during the reduction procedure grows rapidly with the number of external particles and the rank of the integral. Finally, the inversion of the Gram matrix,

$$G^{-1} = \frac{1}{\det G} \text{Adj}(G)^T \quad (2.26)$$

has the determinant of the Gram matrix in the denominator. For degenerate kinematics, the **Gram determinant** goes to zero. When we evaluate numerically the inverse, the small Gram determinants produce numerical instabilities that has to be taken care of with dedicated rescue systems, see Refs. [52–54].

Real contribution

The extra α_S can also come from the squaring of the matrix element, $\mathcal{M}^R(p_a, p_b, \Phi_{n+1})$, from diagrams with an extra QCD emission, Fig. 2.4 (right),

$$d\hat{\sigma}^R = d\Phi_{n+1} \frac{1}{2\hat{s}} \sum_{\substack{\text{spins} \\ \text{colors}}} |\mathcal{M}^R(p_a, p_b, \Phi_{n+1})|^2. \quad (2.27)$$

The extra emitted parton can be resolved, if the angle and energy of emission is large enough, or unresolved. The kinematical configuration of the unresolved process is identical to the Born or virtual contributions. When the particles involved in the QCD emission are massless, there can appear divergences when the emitter and the emitted particles are **collinear** or when the emitted particle is **soft**, meaning its energy is smaller than the energy resolution. Following the procedure described for the virtual contributions, we use dimensional regularization to handle the singularities which appear as poles in the result. The Laurent coefficients of these poles are of equal magnitude between the real and virtual contributions but with opposite sign, so they vanish when we sum both contributions. This statement is guaranteed by the Kinoshita-Lee-Nauenberg (KLN) theorem [45–47] which ensures the cancellation of IRC singularities for sufficiently inclusive observables.

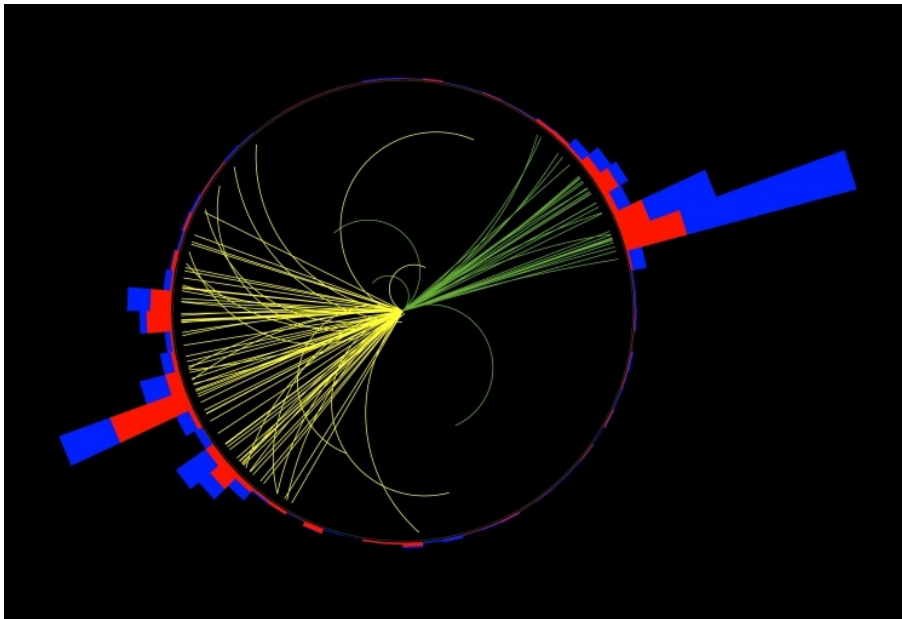


Figure 2.6: This event recorded by the ATLAS collaboration shows two collimated beams of particles, or jets, in opposite directions.

2.3.5 Jet Observables

Hitherto, only fully inclusive observables have been considered, i.e. the total cross-section at NLO. However, often exclusive observables are necessary, for example, we could introduce cuts to isolate interesting kinematic regions or to take into account experimental limitations. The problem is that the KLN theorem do not guarantee the cancellation of soft and collinear singularities in this case. Let us study the conditions that an observable must obey so that the cancellation still occurs. A prediction for an exclusive observable is written as

$$\langle \mathcal{O} \rangle = \sum_{a,b} \int_0^1 dx_a dx_b f_{a/h_1}(x_a, \mu_F) f_{b/h_2}(x_b, \mu_F) \times \quad (2.28)$$

$$\left[\int_n \mathcal{O}^n(p_a, p_b, \Phi_n) d\hat{\sigma}^B + \int_n \mathcal{O}^n(p_a, p_b, \Phi_n) d\hat{\sigma}^V + \int_{n+1} \mathcal{O}^{n+1}(p_a, p_b, \Phi_{n+1}) d\hat{\sigma}^R \right],$$

where \mathcal{O} includes all cuts, binning, selection criteria, \dots , that define the observable.

The cancellation of the singularities between the real and virtual contribution will still happen if the observable is **soft and collinear safe**. Soft and collinear safety fundamentally means that the observable must be independent of the exact shape of the QCD radiation pattern. Formally, we write

$$\mathcal{O}^{n+1}(p_1, \dots, p_j, \dots, p_{n+1}) \xrightarrow{p_j \rightarrow 0} \mathcal{O}^n(p_1, \dots, p_{n+1}), \quad (2.29)$$

$$\mathcal{O}^{n+1}(p_1, \dots, p_j, \dots, p_k, \dots, p_{n+1}) \xrightarrow{\hat{p}_j \rightarrow \hat{p}_k} \mathcal{O}^n(p_1, \dots, p_{jk}, \dots, p_{n+1}). \quad (2.30)$$

A finite prediction of the cross-section with fixed final-state particle number requires to establish an arbitrary resolution criteria to decide when the extra emission from the real contribution is resolved or unresolved. All detectors have a finite spatial resolution and minimum energy sensitivity that could be use as a criterion. The problem is that it depends on the particular parameters of the detector, making its implementation laborious. A

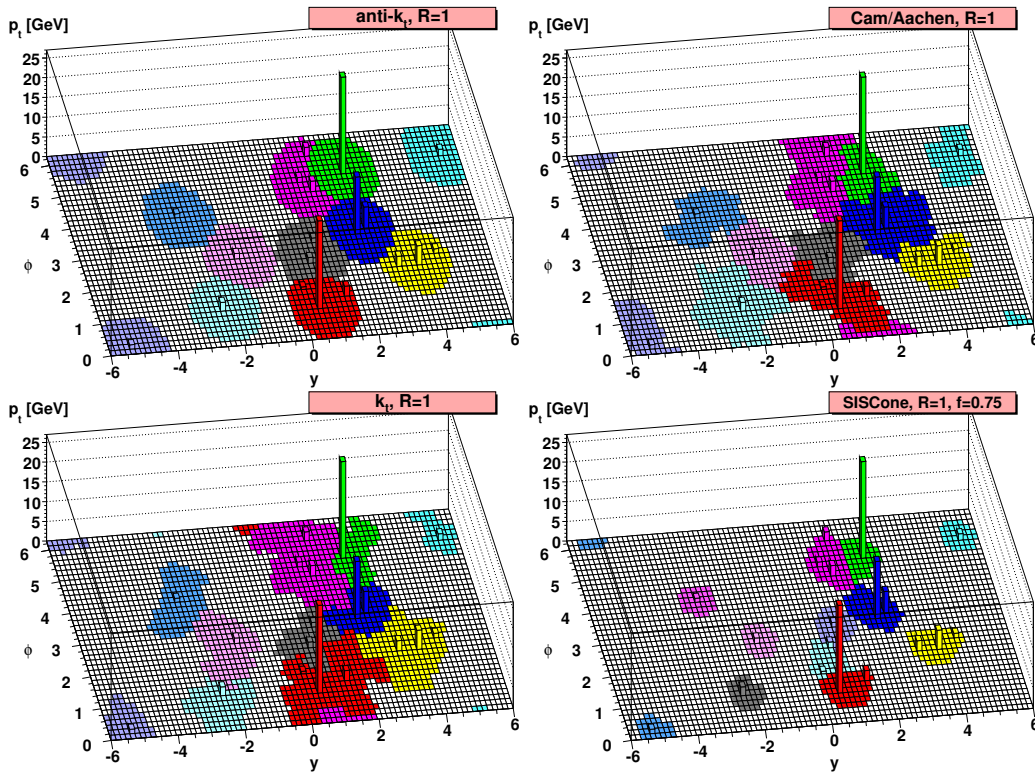


Figure 2.7: Examples of jet algorithms [55].

better approach to select safe observables is a **jet algorithm**. Typical collider events show collimated showers of particles called jets, Fig. [2.6]. The general shape of the jets is given by the hard collision between the partons, but its inner structure is formed through the QCD radiation emitted from the final-state colored particles. A jet algorithm merges different partons into jets in a soft and collinear safe manner leaving an observable that is agnostic about the specific inner structure of the radiation pattern, but is sensitive to the hard collision kinematics. This algorithm should be applicable in the theoretical and experimental sides, and be independent of the parameters of the detector.

In the following, a particular set of jet algorithms, called **k_T -algorithms** [56–59], which are used in the rest of this work, are introduced. An example of the different members of the family together with the SISConc [60] algorithm can be seen in Fig. [2.7]. The k_T -algorithms recursively cluster particles into jets. It starts taking the list of particles and defining the following distances between them, and between the beam axis,

$$\begin{aligned}
 d_{i,j} &= \min \left(k_{T,i}^{2p}, k_{T,j}^{2p} \right) \frac{R_{i,j}^2}{R_0^2}, \\
 d_{i,B} &= k_{T,i}^{2p},
 \end{aligned}$$

where $k_{T,i}$ is the transverse momentum of the particle i , $R_{i,j} = \sqrt{(\eta_j - \eta_i)^2 + (\phi_j - \phi_i)^2}$ is the Euclidean distance in the $\eta - \phi$ plane, and p and R_0 are parameters that define the particular algorithm. Then, it starts with the smallest distances. If it is $d_{i,B}$, it considers the particle i to be a jet, and it is removed from the list of particles. If it is $d_{i,j}$, particle i and j are merged into one. The algorithm stops when all particles have become jets and the list of particles is empty. The jets formed with this procedure are soft and collinear safe but, generally, have strange shapes. The particular case when $p = -1$, called

N_{eval}	Trapezoidal	Simpson	Monte Carlo	Exact result
2	0.538849	0.692566	0.089266	0.292593
4	0.348010	0.284397	0.323231	0.292593
6	0.307477	0.340160	0.184650	0.292593
8	0.296682	0.279573	0.239619	0.292593
10	0.293686	0.302968	0.376381	0.292593
12	0.292861	0.287989	0.212716	0.292593
14	0.292641	0.295304	0.390063	0.292593
16	0.292586	0.291221	0.237507	0.292593
18	0.292576	0.293337	0.145963	0.292593

Table 2.1: Results of the integration of the Breit-Wigner curve in Fig. 2.31 with a different number of evaluations of the integral, and the exact result.

	Trapezoidal	Simpson	Monte Carlo
1-dim	$\frac{1}{N_{\text{eval}}^2}$	$\frac{1}{N_{\text{eval}}^4}$	$\frac{1}{\sqrt{N_{\text{eval}}}}$
d -dim	$\frac{1}{N_{\text{eval}}^{2/d}}$	$\frac{1}{N_{\text{eval}}^{4/d}}$	$\frac{1}{\sqrt{N_{\text{eval}}}}$

Table 2.2: Asymptotic errors for our three methods of choice in one dimension and in d dimensions.

anti- k_T algorithm [59], is widely used, among other things, because the jets formed closely resemble actual cones.

2.3.6 Monte Carlo

The evaluation of observable quantities, Eq. (2.28), requires the calculation of high-dimensional integrals. In practice, the analytical calculation of these integrals is often not feasible and numerical methods to evaluate them are necessary. A number of algorithms have been developed to calculate integrals. Let us compare a few of the most used ones by computing the integral of the Breit-Wigner curve

$$f(E) = \frac{k}{(E^2 - m^2)^2 + m^2\Gamma^2}, \quad (2.31)$$

with $k = 0.01$, $m = 0.5$, $\Gamma = 0.2$, for which the result is known. To compare the different methods, we use the number of evaluations of the integrand, N_{eval} . In Table. 2.1, the value given for the one dimensional integral of Eq. (2.31) with different methods can be seen together with the exact result in the last column. The Trapezoidal and Simpson algorithms converge much faster to the exact result than the Monte Carlo one. This is confirmed in Fig. 2.8, where the error of each algorithm as a function of N_{eval} is presented. In navy blue, the error of the Simpson method scales as $\sim 1/N_{\text{eval}}^4$ for high values of N_{eval} , while, in brown, the Trapezoidal method goes as $\sim 1/N_{\text{eval}}^2$. Finally, in turquoise, the Monte Carlo Method, whose expected errors scale as $\sim 1/\sqrt{N_{\text{eval}}}$, is shown.

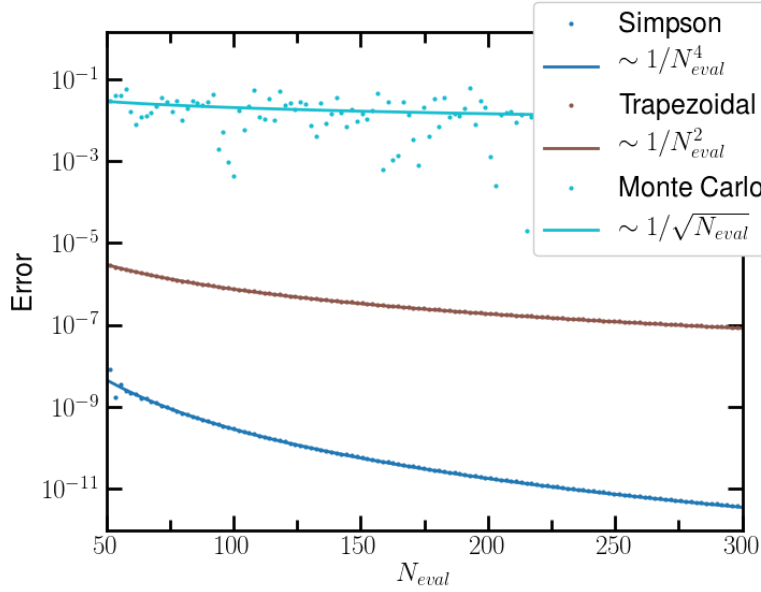


Figure 2.8: Integration errors for different number of integrand evaluations, N_{eval} , for three different methods and their asymptotic behavior.

The picture changes drastically for higher dimension integrals because the error of the Trapezoidal and the Simpson methods explicitly depends on the dimensionality of the integral, while the $1/\sqrt{N_{eval}}$ of the Monte Carlo method is independent of the dimension, see Table. 2.2. So, for $d = 4$ the Monte Carlo converges as fast as the Trapezoidal method, and for $d = 8$ as fast as the Simpson's method.

In the following, a brief exposition of the Monte Carlo method is given. The Monte Carlo method solves integrals like

$$I = \int_V d^d x f(x),$$

by sampling them. The mean value of a set of uniformly distributed points, x_i on V is calculated, such that the integral is given by

$$I \approx I_{MC} = \frac{V}{N_{eval}} \sum_i f(x_i).$$

For convenience, it is always possible to work in the unit hypercube with a proper change of variables.

$$I = \int_0^1 d^d y J(y) f(x(y)), \quad \text{and} \quad I_{MC} = \frac{V}{N_{eval}} \sum_i J(y_i) f(x(y_i)),$$

where $J(y)$ is the Jacobian factor of the transformation. The variance $V_I = \sigma_I^2$ is

$$\sigma_I^2 = \frac{1}{N_{eval}} \left(\int_0^1 d^d y J^2(y) f^2(x(y)) - I^2 \right).$$

We can also get a Monte Carlo estimate of the variance

$$\sigma_{MC}^2 = \frac{1}{N_{eval} - 1} \left(\frac{1}{N_{eval}} \sum_i J^2(y_i) f^2(x(y_i)) - I_{MC}^2 \right).$$

The Monte Carlo result is then given by

$$I = I_{MC} \pm \sqrt{\frac{V_I}{N_{\text{eval}}}}.$$

Importance sampling

Monte Carlo integration converges slow, as $1/\sqrt{N_{\text{eval}}}$. However, the error depends on the variance as well. For example, if the function to integrate is constant, the variance is zero, and only one point is needed to know the exact value of the integral. This suggests a strategy called **importance sampling** that consists on using our knowledge of the process to make the change of coordinates that reduces the variance of the integral.

In VBFNLO, we use a Monte Carlo algorithm called **Monaco** which is a modification of the popular Monte Carlo **VEGAS** [61, 62]. Monaco generates an array of random numbers r , which will be transformed into the appropriate kinematic variables using the knowledge of the process to write Eq. (2.18) as

$$\begin{aligned} \sigma(h_1 h_2 \rightarrow p_1 \dots p_n) = & \\ & \sum_{a,b} \int d^{3n+2} r \left| \frac{\partial(\Phi_n, x_a, x_b)}{\partial r} \right| f_{a/h_1}(x_a(r), \mu_F) f_{b/h_2}(x_b(r), \mu_F) \times \\ & \mathcal{O}^n(p_1(r), \dots, p_n(r)) \frac{1}{2\hat{s}} \sum_{\substack{\text{spins} \\ \text{colors}}} |\mathcal{M}(p_a(r), p_b(r), \Phi_n(r))|^2. \end{aligned}$$

In order to reduce the variance, the calculation can be separated into different iterations and the information obtained can serve to further optimize the grid automatically. This is known as **adaptive** importance sampling, which is the main feature of VEGAS. A problem to note with the adaptive importance sampling on VEGAS is that it changes the grid along the axis, hence, diagonal effects are not be properly considered, and the adaptation could be suboptimal.

2.3.7 Catani-Seymour Subtraction

In order to numerically evaluate the cross-section, the real and virtual contributions have to be integrated separately. This poses the problem that the divergences will only cancel from the sum between the real and virtual contributions after the integration. Methods to cancel the divergences before integrating have been developed, and are classified into two classes: **slicing methods** [63–66], and **subtraction methods** [67–70].

In this thesis, a widespread subtraction method developed by Catani and Seymour [69, 70] is used. Subtraction methods work by adding and subtracting a contribution that has the same IRC behavior as the real contribution in d-dimensions:

$$\sigma^{NLO} = \int_n d\sigma^B + \int_n d\sigma^V + \int_{n+1} (d\sigma^R - d\sigma^A) + \int_{n+1} d\sigma^A. \quad (2.32)$$

In particular, Catani-Seymour makes use of the known collinear and soft factorization properties of the scattering amplitudes to write the $d\sigma^A$ term as

$$d\sigma^A = \sum_{\text{dipoles}} d\sigma^B \otimes dV_{\text{dipole}}, \quad (2.33)$$

which is not a complete factorization of the Born cross-section due to helicity and color correlations represented symbolically by \otimes . The dV_{dipole} has to satisfy two main properties:

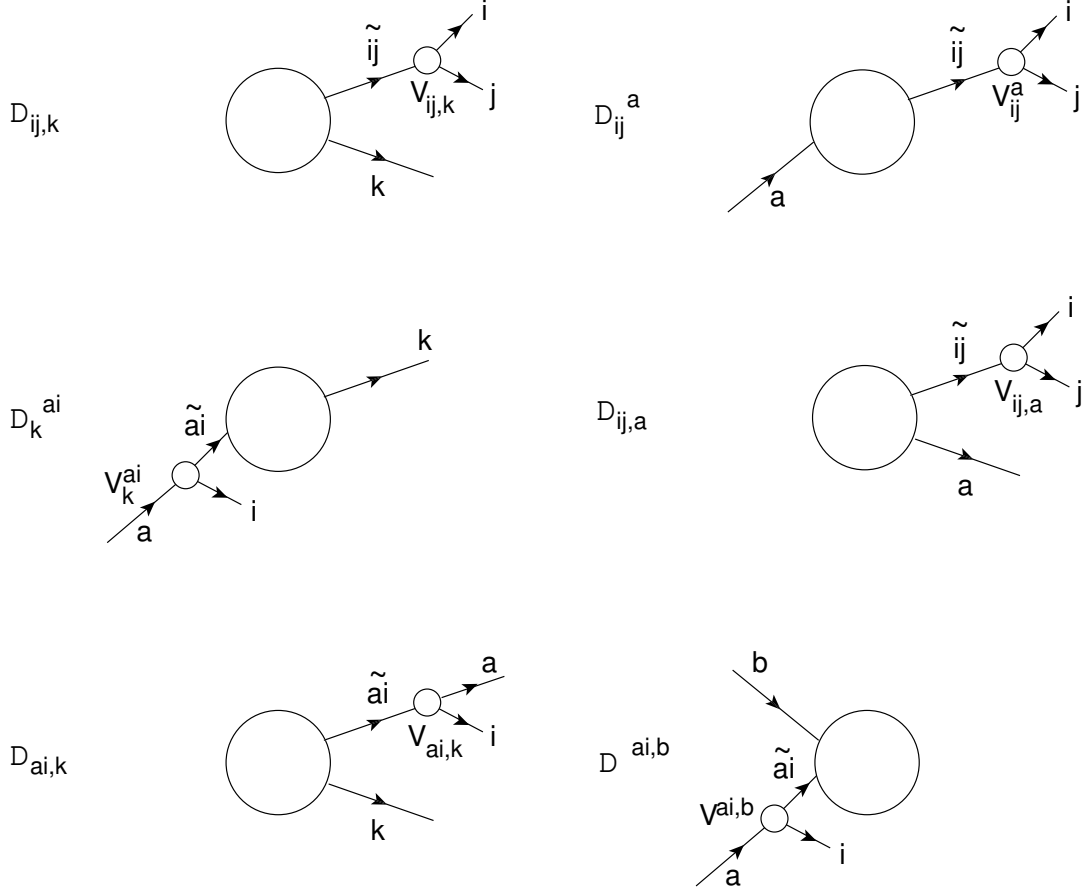


Figure 2.9: Possible kinematic configurations of the splitting partons and spectator particle with their corresponding dipoles.

it has to have the same divergent structure as the soft and collinear approximations of the real contribution, and it has to be integrable over the one emitted parton phase space. This is achieved starting from the Born configuration and making all possible splittings of the partons, each giving a kinematic configuration that corresponds to a real contribution one. In order to avoid double counting, the divergent parts are approached smoothly, and a choice of momentum in the splittings is made such that momentum is conserved and all particles, before and after the splitting, are on-shell. The choice of momenta is not unique and specific ones are made to each kinematic configuration, Fig. 2.9, to guarantee that the dipole is integrable over the one parton phase space. In order to have momentum conservation on the splitting, another parton have to absorb the recoil. The form of the dipole will only depend on the quantum numbers of the particles involved in the splitting, on the momenta of these particles, and on the momenta of the spectator particle.

The following notation is introduced to make easy the treatment of color and spin correlations. The amplitude is written as a vector in color-helicity space, like $|1, 2, \dots, n\rangle$, such that

$$|\mathcal{M}|^2 = \langle 1, 2, \dots, n | 1, 2, \dots, n \rangle,$$

where the numbers correspond to different particles. We write the generators of $SU(3)$ as operators acting on this vector space

$$\mathbf{T}_i |1, 2, \dots, i, \dots, n\rangle = T_R^{c_i} |1, 2, \dots, i, \dots, n\rangle,$$

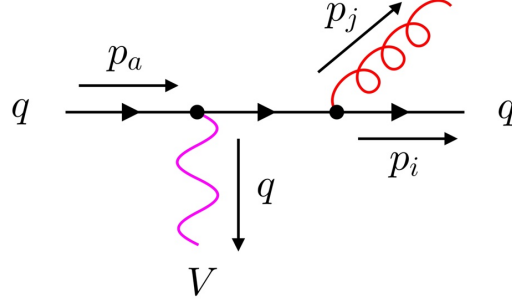


Figure 2.10: Kinematic configuration for a process with an initial-state parton and final-state singularity.

where c_i is the color charge of particle i , and R is the representation; fundamental if the particle i is a quark, adjoint if it is a gluon.

The color-charge algebra is defined by

$$(\mathbf{T}_i \cdot \mathbf{T}_j)|1, 2, \dots, n\rangle = \mathbf{T}_i(\mathbf{T}_j|1, 2, \dots, n\rangle),$$

and has the following property

$$\begin{aligned} \mathbf{T}_i \cdot \mathbf{T}_j &= \mathbf{T}_j \cdot \mathbf{T}_i \quad \text{if } i \neq j, \\ \mathbf{T}_i^2 &= C_i, \end{aligned}$$

where C_i is the quadratic Casimir in the corresponding representation. Moreover, color conservation implies that $|1, 2, \dots, n\rangle$ is a color singlet, which means that

$$\sum_i \mathbf{T}_i|1, 2, \dots, i, \dots, n\rangle = 0, \quad (2.34)$$

for i running over all particles.

As an example, we are going to describe the calculation of the dipole for a process with an initial-state quark and final-state gluon emission. The dipole corresponding to the kinematic configuration shown in Fig. 2.10 is given by

$$\mathcal{D}_{ij}^a = -\frac{1}{2p_i \cdot p_j} \frac{1}{x_{ij,a}} \langle 1, \dots, \tilde{i}j, \dots, m+1; \tilde{a} | \frac{\mathbf{T}_a \cdot \mathbf{T}_{ij}}{\mathbf{T}_{ij}^2} \mathbf{V}_{ij}^a | 1, \dots, \tilde{i}j, \dots, m+1; \tilde{a} \rangle, \quad (2.35)$$

where the **tilde kinematics**, defined to have exact momentum conservation, is

$$\tilde{p}_a^\mu = x_{ij,a} p_a^\mu, \quad \tilde{p}_{ij}^\mu = p_i^\mu + p_j^\mu - (1 - x_{ij,a}) p_a^\mu,$$

with

$$x_{ij,a} = \frac{p_i \cdot p_a + p_j \cdot p_a - p_i \cdot p_j}{(p_i + p_j) \cdot p_a},$$

where V_{ij}^a are the splitting functions. They could depend on the particle type, the helicity, or the Lorentz structure of the two particles involved in the splitting. In this case, it only depends on the particle type, and it is given by

$$V_{q_i g_j}^a = 8\pi\alpha_S C_F \left[\frac{2}{1 - \tilde{z}_i + (1 - x_{ij,a})} - (1 - \tilde{z}_i) \right],$$

where

$$\tilde{z}_i = \frac{p_i \cdot p_a}{p_i \cdot p_a + p_j \cdot p_a}.$$

The Born configuration in this case has only two colored particles, that makes the color algebra trivial due to color conservation Eq. (2.34)

$$\mathbf{T}_1 \cdot \mathbf{T}_2 |1, 2\rangle = -\mathbf{T}_1 \cdot \mathbf{T}_1 |1, 2\rangle = -\mathbf{T}_1^2 |1, 2\rangle = -\mathbf{T}_2^2 |1, 2\rangle = -C_F |1, 2\rangle.$$

Finally, Eq. (2.35) looks like

$$\mathcal{D}_{ij}^a = -\frac{1}{2p_i \cdot p_j} \frac{1}{x_{ij,a}} 8\pi\alpha_S C_F \left[\frac{2}{1 - \tilde{z}_i + (1 - x_{ij,a})} - (1 - \tilde{z}_i) \right] |\mathcal{M}_B(\tilde{p})|^2.$$

The dipole amplitude will be the sum of all the dipoles of the possible kinematic configurations of the process

$$|\mathcal{M}_{\mathcal{D}}|^2 = \sum_{kinematics} \mathcal{D}.$$

The dipoles cancel the soft and collinear divergences of the real contribution. Moreover, they can be integrated analytically over the one parton phase space canceling the infrared divergences of the virtual contribution. Hence, the cross-section can be written as,

$$\sigma^{NLO} = \int_n d\sigma^B + \int_{n+1} (d\sigma^R - d\sigma^A) + \int_n (d\sigma^V + \int_1 d\sigma^A). \quad (2.36)$$

If identified partons with specified momenta are present, the cancellation of the collinear divergences is spoiled, and they have to be absorbed into non-perturbative distribution functions, leaving a finite contribution. The integration over the one particle phase space is done analytically, and the result obtained is written symbolically as

$$\int_1 d\sigma^A = d\sigma^B(p) \otimes \mathbf{I} + \int_0^1 dx \left[d\sigma^b(xp) \otimes (\mathbf{P} + \mathbf{K} + \mathbf{H})(x) \right], \quad (2.37)$$

where the $d\sigma^B(p) \otimes \mathbf{I}$ cancels the infrared divergences of the virtual contribution and the rest of the right-hand side is the finite remainder of the identified partons collinear divergences. The insertion operator $\mathbf{I}(\epsilon)$ can be calculated with

$$\mathbf{I}(\epsilon) = -\frac{\alpha_S}{2\pi} \frac{1}{\Gamma(1-\epsilon)} \sum_i \frac{1}{\mathbf{T}_i^2} \mathcal{V}_i(\epsilon) \sum_{j \neq i} \mathbf{T}_i \cdot \mathbf{T}_j \left(\frac{4\pi}{2p_i \cdot p_j} \right)^\epsilon, \quad (2.38)$$

where

$$\mathcal{V}_i(\epsilon) = \mathbf{T}_i^2 \left(\frac{1}{\epsilon^2} - \frac{\pi^2}{3} \right) + \gamma_i \frac{1}{\epsilon} + \gamma_i + K_i + \mathcal{O}(\epsilon),$$

and

$$\gamma_q = \gamma_{\bar{q}} = \frac{3}{2} C_F, \quad \gamma_g = \frac{11}{6} C_A - \frac{2}{3} n_f T_F.$$

$$K_q = K_{\bar{q}} = \left(\frac{7}{2} - \pi^2 6 \right) C_F, \quad K_g = \left(\frac{67}{18} - \frac{\pi^2}{6} \right) C_A - \frac{10}{9} n_f T_F.$$

Taking this into account, the complete result of the Catani-Seymour subtraction can be written as

$$\begin{aligned} \sigma^{NLO} = & \int_n d\sigma^B + \int_{n+1} \left(d\sigma^R - \sum_{dipoles} d\sigma^B \otimes dV_{dipole} \right) \\ & + \int_n (d\sigma^V + d\sigma^B \otimes \mathbf{I}) + \int_0^1 dx \int_n \left[d\sigma^b(xp) \otimes (\mathbf{P} + \mathbf{K} + \mathbf{H})(x) \right]. \end{aligned} \quad (2.39)$$

2.3.8 Parton Shower

As mentioned in Sec. 2.3.5, in an LHC collision numerous final-state particles, clustered into jets, are produced. The hard process calculations can not reproduce this high particle multiplicity which is due to softer QCD radiation coming from the initial- or final-state colored particles. However, a comparison of the theoretical calculations for exclusive observables with experimental observations will require to simulate this radiation.

There are two different strategies to take into account the extra radiation. First, higher-order perturbative calculations include extra emissions needed to remove IR divergences coming from the loop diagrams. For example, at NLO, as explained in Sec. 2.3.4, we have to take into account the real contribution formed by diagrams with an extra QCD emission, these contributions are exact at a given α_S order. Considering higher-order contributions becomes very demanding. The second method, called **parton shower**, is to work in the soft-collinear approximation, where the extra emission contribution to the cross-section factorizes from the hard-process. This allows to systematically add emissions through a Markov process preserving unitarity, i.e. without changing the cross-section normalization given by the hard process calculation.

In the following, the details of the parton shower implementation is described, starting from final-state radiation and continuing with initial-state radiation. The reason that the initial-state radiation is explained separately is due to a complication in the evaluation of the PDFs. Adding radiation to the initial-state particles changes the energy and quantum numbers of the parton coming from the PDFs. Finally, the **matching** between NLO hard-process calculations and parton showers is shown, the difficulty in this case stems from the possibility of double counting due to some contributions of the parton shower already being taken into account by the real contribution.

Final-state radiation

Assuming a certain hard-process observable \mathcal{O} at LO, the parton shower gives us a new observable modifying \mathcal{O} by adding extra radiation to its colored particles, denoted by $I_{MC}(\mathcal{O})$.

In the soft-collinear approximation, the cross-section factorizes like

$$d\sigma_{n+1} \approx \sigma_n \sum_{partons} \frac{\alpha_S}{2\pi} \frac{d\rho}{\rho} dz P_{ij}(z), \quad (2.40)$$

where $P_{ij}(z)$ are the Altarelli-Parisi splitting functions, σ_n is the Born cross-section, and $d\rho/\rho$ is any scale of the process that serves to order the emissions

$$\frac{d\rho}{\rho} = \frac{d\theta^2}{\theta^2} = \frac{dq^2}{q^2} = \frac{dp_T^2}{p_T^2}.$$

Eq. (2.40) allows a **probabilistic interpretation**, since

$$\mathcal{P}_{em} = \int_{p_{T,min}}^{p_{T,max}} \frac{dp_T^2}{p_T^2} \frac{\alpha_S}{2\pi} \int_{z_{min}}^{z_{max}} dz P_{ij}(z), \quad (2.41)$$

can be understood as the probability for the emission of a parton with $p_T^2 \in [p_{T,min}, p_{T,max}]$ with energy fraction $z \in [z_{min}, z_{max}]$.

The parton shower will emit new partons from existing ones with probability given by Eq. (2.41), such that the quantum numbers and momentum are conserved, until some low

energy scale cut is achieved. Moreover, we must impose **unitarity**. To do that, we define the no-emission probability as

$$\mathcal{P}_{no-em} = 1 - \mathcal{P}_{em}. \quad (2.42)$$

We can calculate the no-emission probability between the scales ρ_1 and ρ_2 using Eq. (2.42) and Eq. (2.41) as

$$\begin{aligned} \mathcal{P}_{no-em}(\rho_1, \rho_2) &= \lim_{N \rightarrow \infty} \prod_n^N d\mathcal{P}_{no-em}[\rho_1 + n\Delta\rho, \rho_1 + (n+1)\Delta\rho] \\ &= \lim_{N \rightarrow \infty} \prod_n^N (1 - d\mathcal{P}_{em}[\rho_1 + n\Delta\rho, \rho_1 + (n+1)\Delta\rho]) \\ &= \exp\left(-\lim_{N \rightarrow \infty} \sum_n d\mathcal{P}_{em}[\rho_1 + n\Delta\rho, \rho_1 + (n+1)\Delta\rho]\right) \\ &= \exp\left(-\int_{\rho_1}^{\rho_2} \frac{d\rho}{\rho} \frac{\alpha_S}{2\pi} \int_{z_{min}}^{z_{max}} dz P_{ij}(z)\right). \end{aligned} \quad (2.43)$$

The right-hand function in the last line of Eq. (2.43) is called the **Sudakov form factor**, $\Delta(\rho_1, \rho_2)$ and gives the probability to **not** have an emission between the scales ρ_1 and ρ_2 ,

$$\Delta(\rho_1, \rho_2) = \exp\left(-\int_{\rho_1}^{\rho_2} \frac{d\rho}{\rho} \frac{\alpha_S}{2\pi} \int_{z_{min}}^{z_{max}} dz P_{ij}(z)\right).$$

Hence, we can define the probability to have an emission at an energy scale ρ assuming there has not been emissions before as

$$\mathcal{P}_{first}(\rho) = \mathcal{P}_{em}(\rho)\mathcal{P}_{no-em}(\rho_{max}, \rho) = \mathcal{P}_{em}(\rho)\Delta(\rho_{max}, \rho).$$

Initial-state radiation

When new emissions are added to the initial-state, keeping the kinematics of the hard process unchanged, the quantum numbers at which the PDF have to be evaluated are modified. Hence, the new emission probability can be written as

$$d\mathcal{P}_{em}(\rho) = \frac{d\rho}{\rho} \frac{\alpha_S}{2\pi} \int_{z_{min}}^{z_{max}} dz P_{ij}(z) \frac{\frac{x}{z} f_i(\frac{x}{z}, \rho)}{x f_j(x, \rho)},$$

and the Sudakov form factor as

$$\Delta(\rho_1, \rho_2) = \exp\left(-\int_{\rho_1}^{\rho_2} \frac{d\rho}{\rho} \frac{\alpha_S}{2\pi} \int_{z_{min}}^{z_{max}} dz P_{ij}(z) \frac{\frac{x}{z} f_i(\frac{x}{z}, \rho)}{x f_j(x, \rho)}\right).$$

This can be interpreted as a reverse evolution compared to the DGLAP equations. The DGLAP equations evolve the PDFs from a low energy scale to the energy scale of the hard process. The parton shower will add new emissions before the fixed parton entering the hard process lowering the energy scale at which the PDFs are evaluated.

Matching

Two different ways to introduce exclusive processes with an extra emission have been presented: calculating higher-order corrections at the partonic level, where the extra emission is considered exactly, and it is needed to remove the soft-collinear divergences

from the virtual contribution, and through the parton shower, adding emissions in the soft-collinear approximation to the Born process preserving unitarity. There are advantages and disadvantages to both methods. The higher-order correction contains the full result at order $\mathcal{O}(\alpha_S)$. On the other hand, higher-order calculations are difficult to do, and NNLO calculations and higher are currently out of reach for most processes.

In practice, the best strategy is to combine the advantages of both descriptions, higher-order calculations and parton showers. The first problem is the possibility of **double counting**. The parton shower contains an approximation to all real and virtual corrections, when we include the $\mathcal{O}(\alpha_S)$ exact result, part of this contribution is also taken into account in the parton shower. Different strategies have been developed at NLO to solve the problem. We are going to explain one of these methods, called MC@NLO, [71].

In the following, we are going to describe the implementation of the MC@NLO matching procedure in the case of a NLO calculation in which the soft-collinear singularities were removed using a subtraction scheme, i.e. Catani-Seymour. The subtracted NLO contribution can be written in the following way,

$$d\hat{\sigma}^{NLO} = d\hat{\sigma}^B + d\hat{\sigma}^{SV} + d\hat{\sigma}_{fin}^{coll} + d\hat{\sigma}^{SR}. \quad (2.44)$$

The first term, $d\hat{\sigma}^B$ is the Born contribution for a $2 \rightarrow n$ process; $d\hat{\sigma}^{SV}$ is the subtracted virtual contribution, Sec. 2.3.7, and it has the same phase space as the Born configuration; the finite remainder due to the absorption of the initial-state collinear divergences into the PDFs, $d\hat{\sigma}^{coll}$, which has an $n + 1$ particle phase space but with the extra emission collinear to the beam, a configuration that will be called quasi- n , [71]; and the subtracted real contribution, $d\hat{\sigma}^{SR}$ has an $n + 1$ particle phase space. All factors in Eq. (2.44) are independently finite. The subtracted real contribution can be written as

$$d\hat{\sigma}^{SR} = d\hat{\sigma}^R - d\hat{\sigma}^A,$$

while the collinear configuration is given by

$$d\hat{\sigma}_{fin}^{coll} = d\hat{\sigma}^{coll} - d\hat{\sigma}_{ct}^{coll}.$$

For simplicity, we absorb the partonic cross-section and the PDFs into one variable called Σ , such that

$$d\Sigma^i \equiv f^{h_1}(x_a, \mu_F) f^{h_2}(x_b, \mu_F) d\hat{\sigma}^i(p_a, p_b, \phi).$$

With this definition, the cross-section for an observable \mathcal{O} at NLO is given by

$$\begin{aligned} \langle \mathcal{O} \rangle = \sum_{ab} \int dx_a dx_b \int d\phi_{n+1} \left[\mathcal{O}(n+1) d\Sigma^R + \mathcal{O}(n) \frac{1}{I_n} (d\Sigma^B + d\Sigma^{SV}) + \right. \\ \left. \mathcal{O}(\tilde{n}) \frac{1}{I_{\tilde{n}}} d\Sigma^{coll} - \mathcal{O}(n) \frac{1}{I_{\tilde{n}}} d\Sigma_{ct}^{coll} - \{ \mathcal{O}(n), \mathcal{O}(\tilde{n}) \} d\Sigma^A \right]. \quad (2.45) \end{aligned}$$

The factors I_n and $I_{\tilde{n}}$ are needed to adjust the normalization of the n , and the $n + 1$ phase space when the integral is done over the $n + 1$ phase space,

$$\begin{aligned} \int d\phi_{n+1}(s) &= I_n \int d\phi_n(s), \\ \int d\phi_{n+1}(s) &= I_{\tilde{n}} \int d\phi_n(xs) dx. \end{aligned}$$

It is convenient to remove the configurations with partons collinear to the beam axis, i.e. $\mathcal{O}(\tilde{n})$. This can be achieved with a change of variables

$$(x_a, x_b) \rightarrow (z_a, z_b), \quad x_a = x_a^{(i)}(z_a, z_b, \phi_{n+1}), \quad x_b = x_b^{(i)}(z_a, z_b, \phi_{n+1}).$$

This change of variables is chosen such that $2(x_{a,b}) = \tilde{2}(\tilde{x}_{a,b})$, and adding the Jacobian factors to the partonic cross-section like

$$d\bar{\Sigma}^{(i)}(z_a, z_b, \phi_{n+1}) = \frac{\partial(x_a^{(i)}, x_b^{(i)})}{\partial(z_a, z_b)} d\Sigma^{(i)}(x_a^{(i)}(z_a, z_b, \phi_{n+1}), x_b^{(i)}(z_a, z_b, \phi_{n+1}), \phi_{n+1}),$$

the Eq. (2.45) reads

$$\begin{aligned} \langle \mathcal{O} \rangle = \sum_{ab} \int dx_a dx_b \int d\phi_{n+1} \left\{ \mathcal{O}(n+1) d\bar{\Sigma}^R + \mathcal{O}(n) \left[\frac{1}{I_n} (d\bar{\Sigma}^B + d\bar{\Sigma}^{SV}) \right. \right. \\ \left. \left. + \frac{1}{I_{\tilde{n}}} d\bar{\Sigma}^{coll} - \frac{1}{I_{\tilde{n}}} d\bar{\Sigma}_{ct}^{coll} - d\bar{\Sigma}^A \right] \right\}. \end{aligned} \quad (2.46)$$

Now, we could make the change $\mathcal{O}(n) \rightarrow I_{MC}(\mathcal{O}, n)$ in Eq. (2.46) which will give us the NLO cross-section with the event distributions given by the MC. As mentioned earlier, this naïve substitution double counts some contributions. To find and subtract the double counted contributions from Eq. (2.46), since the NLO contribution is exact at order $\mathcal{O}(\alpha_S)$, we expand in powers of α_S the result obtained from running only the MC at LO, denoting it by

$$d\bar{\Sigma}^{MC},$$

after adding and subtracting the MC contribution from the n and $n+1$ particle phase space, the explicit observable prediction is given by

$$\begin{aligned} \langle \mathcal{O} \rangle = \sum_{ab} \int dx_a dx_b \int d\phi_{n+1} \left\{ I_{MC}(\mathcal{O}, n+1) (d\bar{\Sigma}^R - d\bar{\Sigma}^{MC}) + \right. \\ \left. I_{MC}(\mathcal{O}, n) \left[\frac{1}{I_n} (d\bar{\Sigma}^B + d\bar{\Sigma}^{SV}) + \frac{1}{I_{\tilde{n}}} d\bar{\Sigma}^{coll} - \frac{1}{I_{\tilde{n}}} d\bar{\Sigma}_{ct}^{coll} - d\bar{\Sigma}^A + d\bar{\Sigma}^{MC} \right] \right\}. \end{aligned} \quad (2.47)$$

This MC@NLO master formula does not have double counting, and it implies that to calculate the matched cross-section for an observable \mathcal{O} two ingredients are necessary: the generation of parton shower events with initial conditions given by $n+1$ particle phase space and with weight $d\bar{\Sigma}^R - d\bar{\Sigma}^{MC}$, and the generation of events with initial conditions given by the n particle phase space with a weight given by the parenthesis accompanying $I_{MC}(\mathcal{O}, n)$ in Eq. (2.47).

2.3.9 Frixione Isolation

There are two different mechanisms that produce final-state photons. The photon could come from the hard collision or from the **parton fragmentation** that produces the hadronic shower. Photons generated during the hard collision, called **direct** or **prompt** photons, are of greater interest because they allow us to study the perturbative dynamics of the process. Mechanisms to reduce the contribution from fragmentation photons are used, and are generally classified into two approaches: the cone approach [72–77], where a cone is drawn around the photon axis and the event is rejected if inside it a significant amount of partonic content is found, and the democratic approach [78], where the photon

is treated like a parton and clustered using a jet algorithm. The photon will be considered prompt if the energy fraction of the photon inside the jet is greater than a certain fixed quantity.

The cone approach can be straightforwardly applied in an experimental setting. From the theoretical side, on the other hand, restricting completely the phase space in a region around the photon restricts the emission of soft gluons inside the cone, which are necessary to cancel the soft divergences coming from the virtual contribution.

The Frixione Isolation approach [79] is a cone algorithm which allows to completely remove the fragmentation component, that is a purely collinear effect, while allowing enough soft gluon radiation inside the cone to cancel the soft singularities.

The algorithm proceeds in the following manner. A cone with half-angle δ_0 is drawn, and the Euclidean distance to the photon in the $\eta - \phi$ plane, given by $R_{i\gamma} = \sqrt{(\eta_i - \eta_\gamma)^2 + (\phi_i - \phi_\gamma)^2}$, is calculated for all partons i inside the cone. If

$$\sum_i E_{T,i} \theta(\delta - R_{i\gamma}) \leq \chi(\delta) \quad \text{for all } \delta \leq \delta_0,$$

where

$$\chi(\delta) = \epsilon E_{T,\gamma} \left(\frac{1 - \cos \delta}{1 - \cos \delta_0} \right)^n,$$

the event is accepted, otherwise it will be rejected. From these definitions, we can see that the purely collinear contribution is completely removed due to $\chi(\delta) \rightarrow 0$ as $\delta \rightarrow 0$, but arbitrarily soft gluons can be found inside the cone which allow to cancel the virtual IR singularities.

Chapter 3

Di-photon production in the VBS channel

3.1 Introduction

In this chapter, the calculation and implementation in the Monte Carlo VBFNLO program of the di-photon production process associated with two jets, $pp \rightarrow \gamma\gamma jj$, in the **vector boson scattering** (VBS) approximation [80] is presented, which includes anomalous couplings based on an EFT approach.

The **triple gauge coupling** (TGC) and **quartic gauge coupling** (QGC) are fixed in the SM by the EW gauge group, $SU(2)_L \times U(1)_Y$, which makes them ideal candidates to study deviations from the SM predicted values. Physics BSM is embedded into operators of SM particles with mass dimension larger than four, see Sec. 2.2. The dimension-6 operators modify the TGC, this modification can be thought as an **anomalous** TGC (aTGC) value, while the dimension-8 operators generates anomalous QGC (aQGC). VBS processes give direct access to these couplings and has a clear signal, with highly boosted jets and the vector bosons in the central part of the detector, which makes them perfect candidates to study the EW structure of the SM, and the determination of dimension-6 and dimension-8 operators, see Refs. [81, 82].

There are two kinds of diagrams contributing to the $pp \rightarrow \gamma\gamma jj$ process depending on the coupling constants order. The gluon mediated diagrams (QCD), which can be seen in Fig. 3.1 are constructed from diagrams of order $\mathcal{O}(g_s^2 g^2)$. The process can have two initial-state quarks, shown in the first line and the last diagram in the second line, which are further classified into a t-channel or s-channel exchange depending on whether the gluon connects two quark lines or is generated from the merging of the initial-state quarks. Outside this classification is the last diagram in the second line, which has both gluons and photons attached to a single quark line. The first two diagrams in the second line show gluon initiated processes. The first one corresponds to a gluon fusion s-channel diagram while the second has both photons and gluon attached to a single quark line. The last line includes the diagrams with one initial-state gluon and one initial-state quark.

The diagrams with an intermediate vector-boson (EW), of order $\mathcal{O}(g_s^0 g^4)$, are presented in Fig. 3.2. The five diagrams in the first and second lines are the t/u-channel exchange, where a vector-boson connects the two quark lines generated by the initial and final-state quarks. The remaining five diagrams show the s-channel contributions, where two quarks merge into a vector-boson. These diagrams correspond to the tri-boson production process $V\gamma\gamma$ with a hadronic decay $V \rightarrow jj$, which is also implemented in VBFNLO including, with some approximations [83], the off-shell effects and spin correlations.

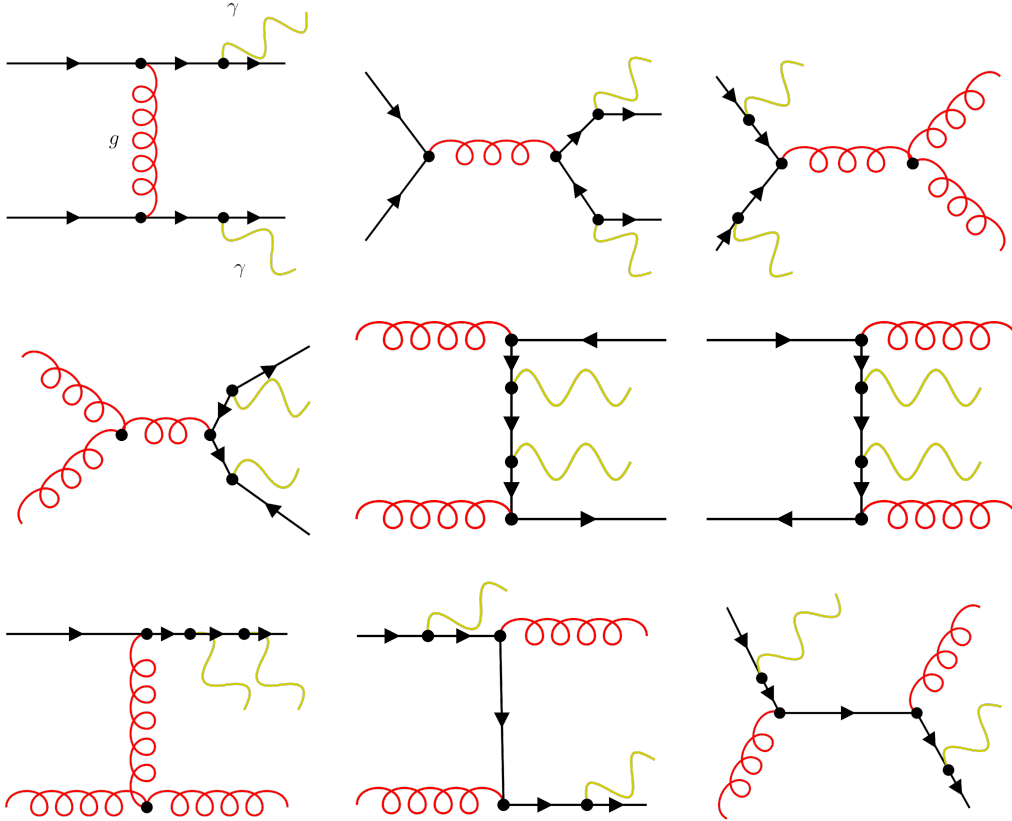


Figure 3.1: Diagrams contributing to the gluon mediated (QCD) $pp \rightarrow \gamma\gamma jj$ process at LO. The first line contains the diagrams with two quarks in the initial-state, the second line contains diagrams with two gluons in the initial-state and the last line contains diagrams with one gluon and one quark in the initial-state. The order of the diagrams in this figure is $\mathcal{O}(g_s^2 g^2)$.

The cross-section is constructed by squaring the amplitude. Three different amplitudes squared can be constructed from the diagrams in Fig. 3.1 and Fig. 3.2 depending on the order of the coupling constants. For example, an order $\mathcal{O}(\alpha_s^2 \alpha^2)$, called **QCD channel**, can be achieved from the product of QCD diagrams, and an order $\mathcal{O}(\alpha_s^0 \alpha^4)$, called **EW channel**, can be constructed from the product of EW diagrams. Moreover, there can be interference terms between the QCD and EW diagrams of order $\mathcal{O}(\alpha_s^1 \alpha^3)$ but these only affect identical quarks and are kinematically suppressed, see Ref. [84, 85].

The EW cross-section is constructed from the amplitude squared of the t/u-channel diagrams, the amplitude squared of the s-channel diagrams and the interference terms between t/u-channel and s-channel diagrams. In kinematic regions where the two jets are boosted along the beam axis with large invariant masses and the vector-bosons are in the central part of the detector, the so-called **VBS region**, the t/u-channel dominates while the s-channel and the interference terms are suppressed. The calculation of the process neglecting the s-channel diagrams and the interference terms is called the **VBS approximation**, which is a good approximation inside the VBS region, see [86]. The s-channel contribution without the interference terms can be recovered in VBFNLO using the tri-boson production process $V\gamma\gamma$ with a hadronic decay.

The QCD channel has the same final-state particles as the EW channel but does not

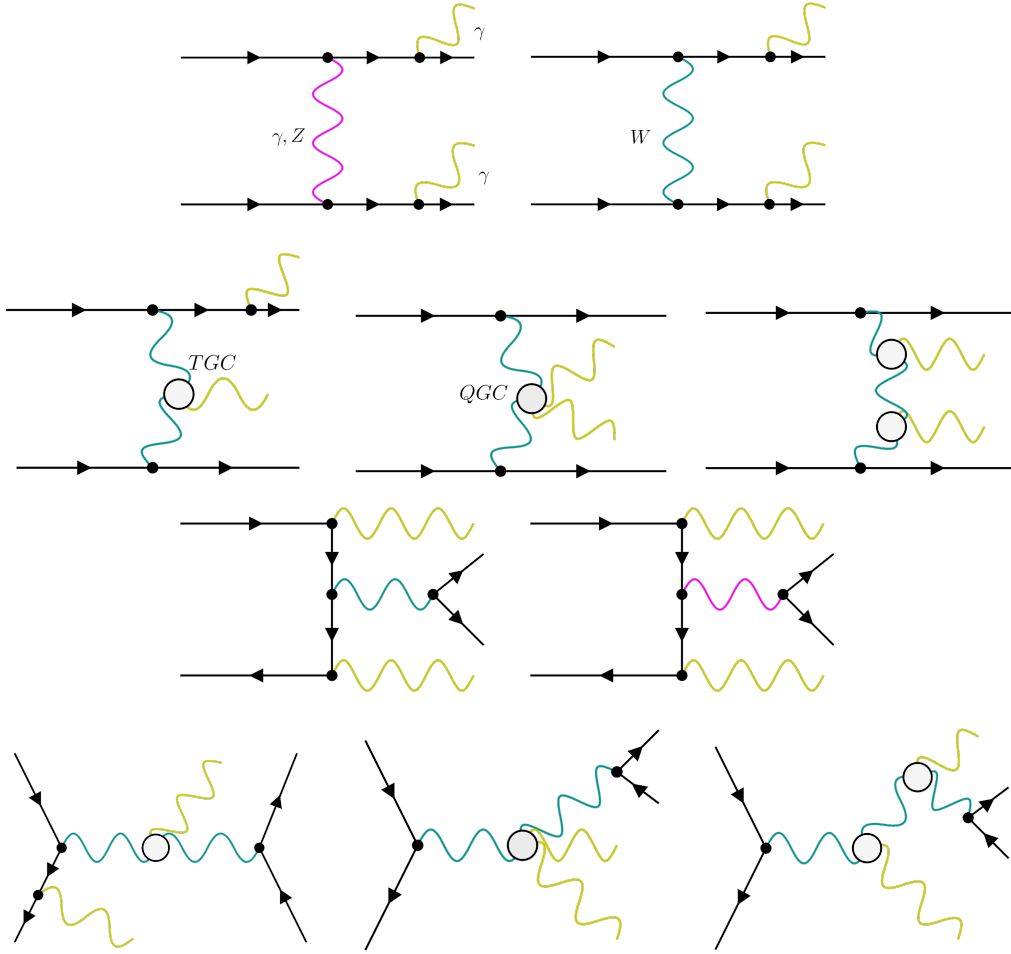


Figure 3.2: Diagrams contributing to the vector-boson (EW) mediated $pp \rightarrow \gamma\gamma jj$ process at LO. The first two lines contain the t/u-channel diagrams, where the quark lines are connected through a vector-boson exchange while the last two lines contains the s-channel diagrams where both initial-state quarks merge into a vector-boson. The order of the diagrams in this figure is $\mathcal{O}(g_S^0 g^4)$.

give us access to TGC or QGC. Thus, it is regarded as an unavoidable background for the EW channel. Precise predictions for the QCD channel have been attained previously in Refs. [87–89], the implementation in VBFNLO was introduced in Ref. [80] where a theoretical study of the EW $pp \rightarrow \gamma\gamma jj$ in the VBS approximation was presented for the first time.

The $pp \rightarrow \gamma\gamma jj$ in the VBS approximation is constructed from six different subprocesses. The first four consists of the flavor preserving subprocesses given by:

$$\begin{aligned} u_i u_j &\rightarrow \gamma\gamma u_i u_j, \\ u_i u_j &\rightarrow \gamma\gamma d_i d_j, \\ d_i d_j &\rightarrow \gamma\gamma u_i u_j, \\ d_i d_j &\rightarrow \gamma\gamma d_i d_j, \end{aligned}$$

which are constructed from the diagrams corresponding to a t/u-channel exchange mediated by a neutral boson, first diagram in Fig. 3.2.

	VBS	full EW	QCD	Interf.	All
σ_{LO} [fb]	24.929(6)	24.94(8)	21.664(10)	0.542(2)	47.15(8)
Δ [%]	52.8	52.9	46.0	1.1	100

Table 3.1: LO cross-sections for the different contributions to the $pp \rightarrow \gamma\gamma jj$ process with the amount in percentage that contributes to the total result.

The other two are the flavor changing subprocesses given by:

$$\begin{aligned} u_i d_j &\rightarrow \gamma\gamma d_i u_j, \\ d_i u_j &\rightarrow \gamma\gamma u_i d_j, \end{aligned}$$

which are t/u-channel with at least one W-boson between both quark lines, all diagrams in the second line and the second diagram in the first line in Fig. 3.2

In Table 3.1, the different contributions to the $pp \rightarrow \gamma\gamma jj$ process at LO are shown using the same cuts as in Sec. 3.4, which are selected such that the VBS approximation is valid and to improve the significance of the EW channel respect to the QCD channel. The interference term between the QCD- and EW-channels is only 1.1% of the total contribution at LO. The full EW and the QCD channels have cross-sections of the same order due to the kinematic cuts to improve the significance of the EW process. The difference between the full EW and the VBS channels is just 0.1% with these cuts. These observations confirm that our assumptions to neglect the interference terms and s-channel contributions inside the VBS region were correct at LO, and we expect them to hold at NLO.

The chapter is structured as follows. In the next section, a detailed explanation of the implementation of the process in VBFNLO is given. After that, the set of checks performed to ensure the correct implementation of the process are shown. Finally, we lay out a phenomenological analysis of the $pp \rightarrow \gamma\gamma jj$ process, highlighting the most important features. The main backgrounds will be also analyzed and cuts to improve the signal versus background ratio will be studied.

3.2 Implementation

VBFNLO [90–93] is a parton level Monte Carlo generator that uses the techniques explained in Sec. 2.3.6 to evaluate the phase space integral. The integrand includes the matrix elements of the process which is numerically calculated by computing the appropriate Feynman diagrams. VBFNLO uses a formalism that factorizes the different pieces contributing to a Feynman diagram, building up master subroutines from them which are re-used in several diagrams and/or processes.

At NLO QCD, the exclusive cross-section is calculated solving the integral in Eq. (2.28), which receives contributions from three different pieces. The Born contribution, with diagrams at the lowest order possible for the given external particles, and the real and virtual corrections.

The main difficulty in our implementation arises from the divergences appearing in the real and the virtual contributions being evaluated in two different phase space configurations, due to the extra emission appearing in the real correction. To separately cancel the IRC divergences, the Catani-Seymour subtraction [56] method, explained in Sec. 2.3.7, is used.

The virtual contribution is made of loop corrections to the quark lines. The quarks are the only colored particles in our process and the corrections involving a gluon between

the two quark lines are ignored in the VBS approximation, where both quark lines are considered as color independent. Considering that there can be one, two or three vector bosons attached to each quark line, the correction will include vertex, boxes and pentagons.

First, the Born contribution implementation is introduced, and it is used to present the construction of the partonic cross-section. After being familiarized with the technique used to calculate Feynman diagrams in VBFNLO, the implementation of the real contribution is shown. The dipole terms needed to cancel the IRC singularities are presented in detail, including the initial-state collinear singularities that are understood as modifications of the scale at which the PDFs are evaluated. Finally, the calculation of the virtual contributions is presented.

3.2.1 Born contributions

In the following, the basic pieces needed to build diagrams inside VBFNLO are described. Henceforth, the notation used is intended to facilitate the use of crossing relations, and it is explained in detail in Ref. [94]. The use of standard momenta p_i aligned with the charge flow lines, and sign factors S_i that distinguish particles from anti-particles make building all crossed diagrams straightforward, just changing the particles for anti-particles with the corresponding change in the sign factors. The physical momenta \bar{p}_i is defined as

$$p_i = S_i \bar{p}_i.$$

The fermion spinors are calculated in the Weyl representation, they are always evaluated with the physical momenta, and all fermions are considered massless. With these assumptions, the two component Weyl spinors of definite chirality τ can be written as

$$\psi(\bar{p}_i, h_i)_\tau = S_i \delta_{h_i, \tau} \sqrt{2\bar{p}_i^0} \chi_{h_i}(\bar{p}_i),$$

where S_i is the sign factor, and $h_i = S_i \bar{h}_i$, where \bar{h}_i is the helicity, normalized such that $h_i = \pm 1$. The $\chi_{h_i}(\bar{p})$ are given by

$$\begin{aligned} \chi_+(\bar{p}) &= [2|\vec{\bar{p}}|(|\vec{\bar{p}}| + \bar{p}_z)]^{\frac{1}{2}} \begin{pmatrix} |\vec{\bar{p}}| + \bar{p}_z \\ \bar{p}_x + i\bar{p}_y \end{pmatrix}, \\ \chi_-(\bar{p}) &= [2|\vec{\bar{p}}|(|\vec{\bar{p}}| + \bar{p}_z)]^{\frac{1}{2}} \begin{pmatrix} -\bar{p}_x + i\bar{p}_y \\ |\vec{\bar{p}}| + \bar{p}_z \end{pmatrix}. \end{aligned}$$

The subroutine used to create the external quark wave functions `psi0m` can be found in `VBFNLO/utilities/brackets.F`,

```
subroutine psi0m(nf, p_i, S_i, psi),
```

where n_f is the number of external fermions for which we want to calculate the wave functions, \bar{p}_i is an array containing the physical momentum of the fermions, and S_i is an array containing the sign factors. The output will be an array containing the outgoing, or incoming wave functions depending on whether the index in the array is even or odd respectively.

On the other hand, the external vector boson polarization vectors, in our case the two photons, are created using the **HELAS** [95] function

```
subroutine VXXXX(k, m_V, h, ±1, e_h^μ(k),
```

where k is the vector boson momentum vector, m_V is the mass of the vector boson, h is the polarization, and the fourth argument is $+1$ for a final state boson, and -1 for an initial state one. The output of the function is the polarization vector for the vector boson, $\epsilon_h^\mu(k)$.

A common repeated diagram is the one formed by a quark line with an off-shell vector boson, see Fig. 3.3. The current is given by

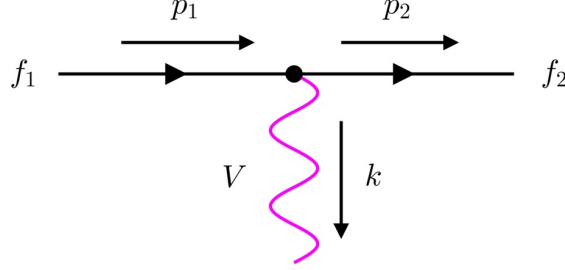


Figure 3.3: Quark line with an off-shell vector boson of momentum k attached to it.

$$j_{h_1}^\mu = -e S_1 S_2 \delta_{h_1 h_2} 2 \sqrt{\bar{p}_1^0 \bar{p}_2^0} g_{h_1}^{V f_1 f_2} \delta_{i_1 i_2} \chi_{h_2}^\dagger(\bar{p}_2) (\sigma^\mu)_{h_1} \chi_{h_1}(\bar{p}_1), \quad (3.1)$$

where the coupling constants, $g_h^{V f_1 f_2}$, are given by

$$\begin{aligned} g_\pm^{\gamma ff} &= Q_f, \\ g_+^{Z ff} &= -Q_f \tan \theta_W, \\ g_-^{Z ff} &= T_{3f} / (\sin \theta_W \cos \theta_W) - Q_f \tan \theta_W, \\ g_+^{W \nu e} &= g_-^{W \nu e} = 1 / (\sqrt{2} \sin \theta_W), \\ g_+^{W u_i d_j} &= (g_-^{W u_i d_j})^* = V_{ij} / (\sqrt{2} \sin \theta_W). \end{aligned}$$

In the code, these couplings are specified by `clr(fermion index, boson index, h)`. The convention of the fermions and bosons indices in VBFNLO can be seen in Table 3.2. The $D_h^\mu(\bar{p}_1, \bar{p}_2) \equiv$

fermion indices		boson indices	
1	$\nu_{e, \mu, \tau}$	1	γ
2	e, μ, τ	2	Z
3	u_i	3	W^+
4	d_i	4	W^-

Table 3.2: Index convention for the fermions and bosons in VBFNLO.

$\chi_h^\dagger(\bar{p}_2) (\sigma^\mu)_h \chi_h(\bar{p}_1)$ is calculated by the following subroutine

```
subroutine curr6(h_max, chi_h_i^\dagger(\bar{p}_2), p_2, chi_h_i(\bar{p}_1), p_1, D_h^\mu(\bar{p}_1, \bar{p}_2)).
```

The calculation only involve four complex multiplications such that, if the external spinors are given by

$$\chi_{h_1}(\bar{p}_i) = \begin{pmatrix} \xi_i \\ \eta_i \end{pmatrix},$$

then

$$\begin{aligned} D^0 &= \xi_2^* \xi_1 + \eta_2^* \eta_1, \\ D^1 &= h_1 (\xi_2^* \eta_1 + \eta_2^* \xi_1), \\ D^2 &= -i h_1 (\xi_2^* \eta_1 - \eta_2^* \xi_1), \\ D^3 &= h_1 (\xi_2^* \xi_1 - \eta_2^* \eta_1). \end{aligned}$$

From now on, we will write

$$\begin{aligned} |1\rangle &= \chi_{h_1}(\bar{p}_1), \\ \langle 2| &= \chi_{h_2}^\dagger(\bar{p}_2). \end{aligned} \quad (3.2)$$

The quark line with an on-shell photon and an off-shell vector boson, Fig. 3.4 is constructed from Eq. (3.1) by modifying the incoming or outgoing spinor to include the fermion propagator and the vector boson polarization vector. The modified spinors, in bra-ket notation, are written by

$$\begin{aligned} |k, 1\rangle &= (\not{p}_1 - \not{k})_{h_1} \not{\epsilon}_{h_1} \chi_{h_1}(\bar{p}_1) \frac{1}{(p_1 - k)^2}, \\ \langle k, 2| &= \chi_{h_2}(\bar{p}_2)^\dagger \not{\epsilon}_{h_2} (\not{p}_2 + \not{k})_{h_2} \frac{1}{(p_2 + k)^2}. \end{aligned} \quad (3.3)$$

These bras, or kets, are created in VBFNLO using the following subroutines

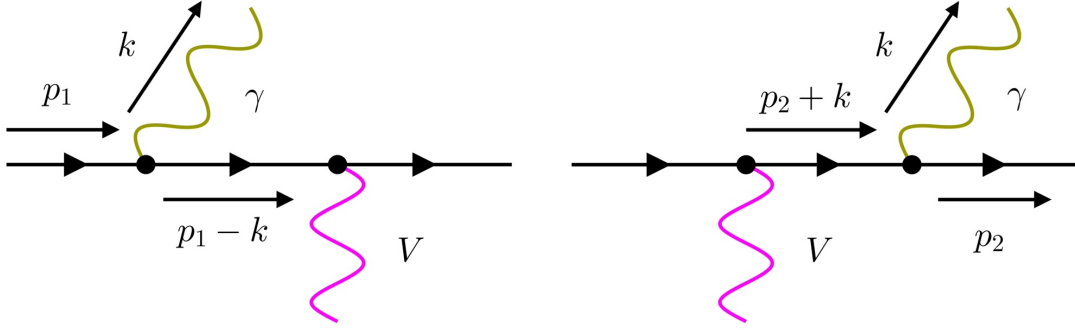


Figure 3.4: Emission of an on-shell photon from a quark line. Before the off-shell boson (left), and after the off-shell boson (right).

```
subroutine ket2c(|1>, .true., p1, h1, k, e_{h1}^\mu, |k, 1>, p1 - k),
subroutine bra2c(<2|, .true., p2, h2, k, e_{h2}^\mu, <k, 2|, p2 + k).
```

The `.true.` in the second argument implies that at least one component of $|1\rangle$, or $\langle 2|$, is real. If all components were complex, the second argument will be set to `.false.` Using Eq. (3.2), the quark line current, Fig. 3.3, can be written as

$$j_{h_1}^\mu = F_1 \delta_{i_1 i_2} \langle 2 | (\sigma^\mu)_{h_1} | 1 \rangle.$$

Likewise, using Eq. (3.3), the currents in Fig. 3.4 can be written as

$$j_{h_1}^\mu = F_1 \delta_{i_1 i_2} \langle 2 | (\sigma^\mu)_{h_1} | k, 1 \rangle, \quad (3.4)$$

$$j_{h_1}^\mu = F_1 \delta_{i_1 i_2} \langle k, 2 | (\sigma^\mu)_{h_1} | 1 \rangle, \quad (3.5)$$

depending on whether the on-shell vector boson is attached to the initial- or final- state parton, and the factor F_1 is given by $F_1 = -eg_{h_1}^{Vff} S_1 S_2 \delta_{h_1 h_2} 2\sqrt{\bar{p}_1^0 \bar{p}_2^0}$.

Alternatively, in VBFNLO to compute quark lines like

$$\langle 2|\psi_h|1\rangle,$$

we call the following subroutine

```
function sic(|2|, vμ, timeex, h, |1|),
```

where `timeex` is a boolean variable that will be set to `.false.` if the time component of v^μ is zero, `.true.` otherwise. The numerical calculation of a slashed vector, i.e. the contraction of the vector with γ^μ , is given by

$$\psi = v^\mu \gamma_\mu = \begin{pmatrix} v^0 \mp v^3 & \mp(v^1 - iv^2) \\ \mp(v^1 + iv^2) & v^0 \pm v^3 \end{pmatrix}.$$

There are parts of diagrams that need only to be calculated once per phase space point, its value being the same for all the crossed diagrams. Even if in our case the final state particles are not leptons, we refer to them as **leptonic tensors**, since this strategy was originally designed for EW $pp \rightarrow Hjjj$ and $pp \rightarrow WWjj$ production. For the $pp \rightarrow \gamma\gamma jj$ process, there are two leptonic tensors: $WW \rightarrow \gamma\gamma$ and $WW \rightarrow \gamma$. The $W^+W^- \rightarrow \gamma\gamma$ is composed by three different diagrams, Fig. 3.5, while only one diagram contributes to the

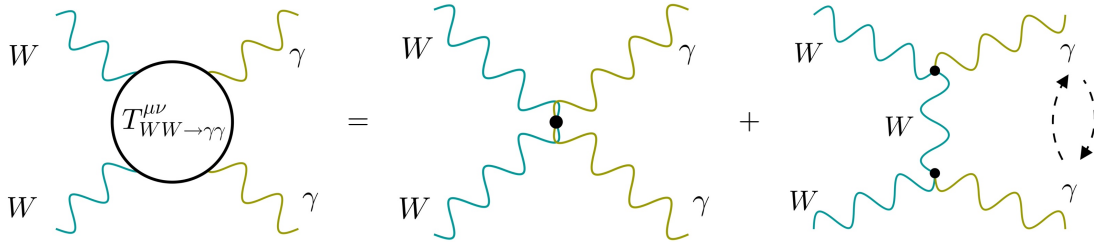


Figure 3.5: Diagrams that contribute to the leptonic tensor $W^+W^- \rightarrow \gamma\gamma$.

leptonic tensor $W^+W^- \rightarrow \gamma$, Fig. 3.6. The $W^+W^- \rightarrow \gamma\gamma$ leptonic tensor is calculated

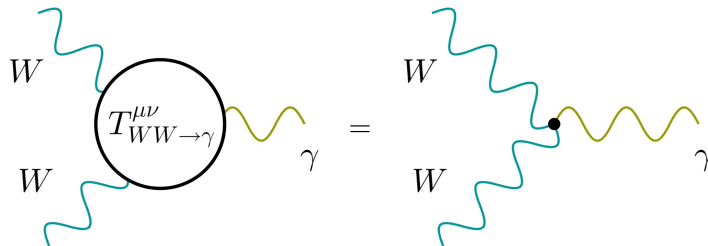


Figure 3.6: Only diagram contributing to the leptonic tensor $W^+W^- \rightarrow \gamma$.

with

```
subroutine wwtoaa(p1, p2, h, T_WW to gamma gamma),
```

and the leptonic tensor for the $W^+W^- \rightarrow \gamma$ with

```
subroutine calc_wvtoa2(idW, h, k, e_h^mu(k), p_idW, T_WW_to_gamma),
```

where $\text{id}_W = 1(2)$ specifies that the momentum p_{id_W} is the $W^+(W^-)$ one. Both subroutines, `wvtoa` and `calc_wvtoa2`, can be found inside `VBFNLO/amplitudes/vvjj/toaa.F`. The leptonic tensors are called only once inside `VBFNLO/amplitudes/vvjj/m2s_qzqq.F`, and its results saved in the corresponding arrays for later use.

In the following, we show a set of helper functions with their mathematical definitions:

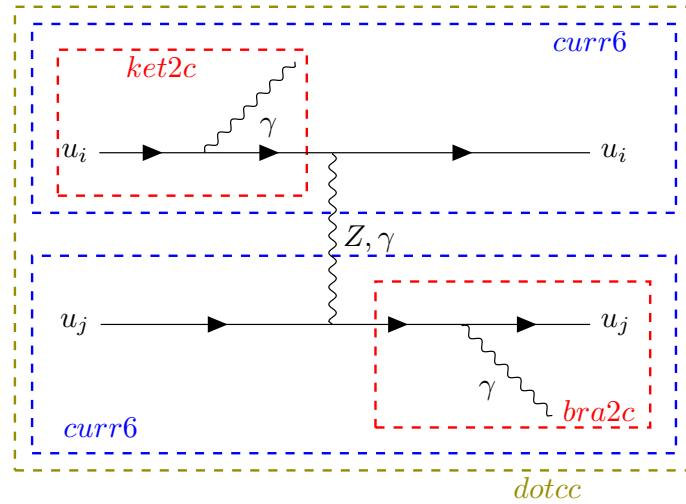
```
j1,mu,j2,nu,T^mu nu:      function contract_Tjj(T, j1, j2)
j_out^nu = j_c,mu T^mu nu:  subroutine contract_T1j(T, jc, jout)
j_out^mu = j_c,nu T^mu nu:  subroutine contract_T2j(T, jc, jout)
v1 . v2 = eta_mu nu v1^mu v2^nu: double complex function dotcc(v1, v2)
```

These pieces allow us to construct the Feynman diagrams as shown in the following section. First, for the neutral currents, and then for the charged currents.

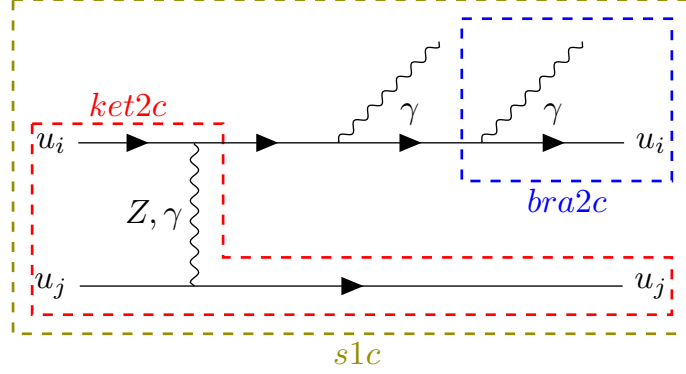
Neutral Currents

In the neutral currents, the photons can only be attached to the quark lines because the SM does not have fully neutral vector boson triple or quartic gauge couplings. The different topologies are given by the location of the on-shell photons. Then, the neutral currents are reduced to one photon in each quark line, which we will call box-box topologies, due to the virtual correction to those quark lines having at most box integrals; or pentagon topologies were one quark line has both photons.

Starting with the box-box topologies, the initial and final-state wave function of the four quarks involved are created with the `psi0m` subroutine. Then, the on-shell photon is attached to one of the quarks; depending on whether we have an initial- or final-state emission of the photon, it is done with the `ket2c` or `bra2c` subroutines, respectively. The quark line is created attaching both quarks to the vector boson between quark lines using `curr6`. Finally, we can attach both quark lines contracting the free indices with `dotcc`, and multiply by the suitable vector boson propagator factor and couplings:



Similarly, diagrams with two photons attached to the same quark line, which define the pentagon topologies, can be calculated. In the call to `ket2c`, or `bra2c`, instead of using the on-shell polarization vector, the off-shell polarization vector attached to the other quark line has to be used. Making use of the $\langle 2, k |$ generated by `bra2c` with an on-shell photon, and the $|1, k'\rangle$ generated by the previous call to `ket2c`, the function `s1c` creates the full diagram where we are only missing the vector boson propagator and the coupling constants.

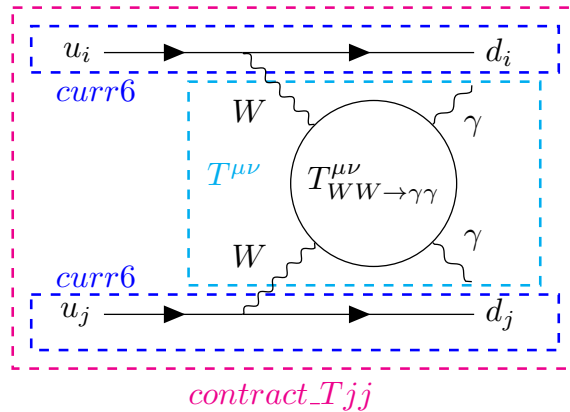


Finally, the vector boson propagator between the quark lines and the corresponding couplings are added.

Charged Currents

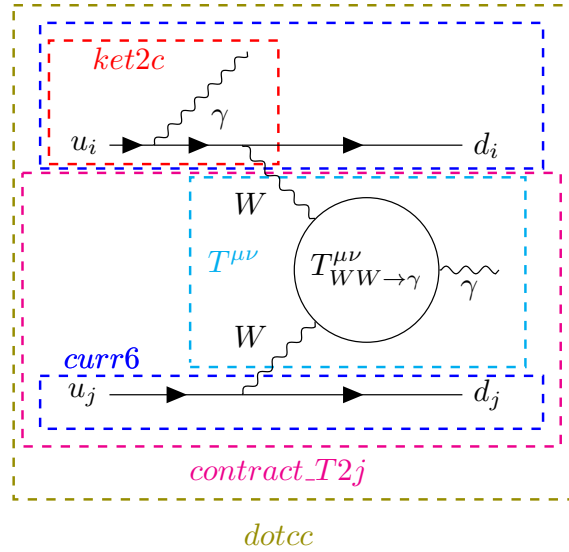
The charged currents also have box-box and pentagon topologies that are built exactly as in the neutral current case; with the only difference that the vector boson between the quark lines will be a W^+ , with the corresponding change in the propagator and coupling constants; and the change of quark flavor in the quark line.

Additionally, the charged current case has two new types of topologies involving the $T_{WW \rightarrow \gamma\gamma}^{\mu\nu}$ and $T_{WW \rightarrow \gamma}^{\mu\nu}$ leptonic tensors. The topology involving $T_{WW \rightarrow \gamma\gamma}^{\mu\nu}$ does not have photons attached to the quark lines. So, after creating the initial- and final-state wave functions with `psi0m`, we only need to create the quark lines with `curr6` and contract both with the leptonic tensor indices using `contract_Tjj`:



The topology involving the $T_{WW \rightarrow \gamma}^{\mu\nu}$ leptonic tensor has a photon emitted from one of the quark lines. The photon will be attached to the corresponding quark wave function with `ket2c` or `bra2c`, and the quark line created with `curr6`. In this case, we have to distinguish the quark line without a photon, which has to be contracted with the correct leptonic tensor index using `contract_T1j` or `contract_T2j` depending on whether it is the upper or lower quark

line, and the one with the photon, which will be attached to the remaining index using `dotcc`:



3.2.2 Real contributions

The real amplitudes are built analogously to the Born amplitudes. They are generated from the Born amplitude with an extra emission of a gluon, which is done inside `vBFNLO/amplitudes/vvjj/qqZjqq.F` in this process.

In the following, the implementation of the Catani-Seymour subtraction method to deal with the soft and collinear divergences is explained in detail.

Recall that in the VBS approximation, each quark line is considered to belong to a different color group. As an example, we focus on the upper quark line, however, the lower quark line is computed similarly. In Fig. 3.7, the real extra emission of a gluon from a

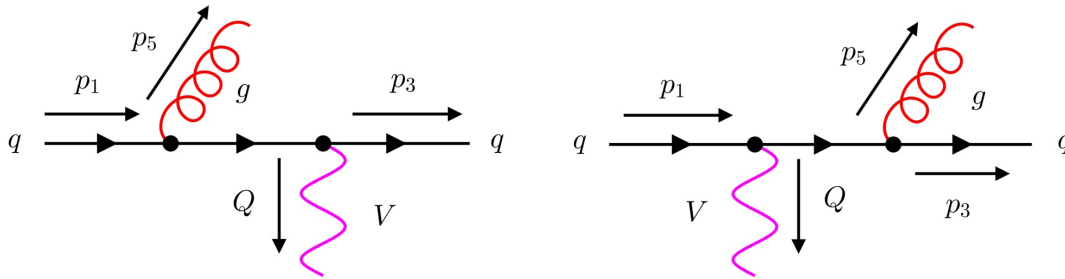


Figure 3.7: Feynman diagrams of a quark line with an emission of a gluon from the initial-state quark (left), and from the final-state quark (right).

quark initiated process is shown. The case of an anti-quark is identical. The dipole terms for the diagrams in Fig. 3.7 are, using the notation of Ref. [69],

$$\mathcal{D}_3^{15} = \frac{1}{2p_1 \cdot p_5} \frac{1}{x_{35,1}} 8\pi C_F \alpha_s \left(\frac{2}{1 - x_{35,1} + u_5} - (1 + x_{35,1}) \right) |\mathcal{M}_B|^2,$$

$$\mathcal{D}_{35}^1 = \frac{1}{2p_3 \cdot p_5} \frac{1}{x_{35,1}} 8\pi C_F \alpha_s \left(\frac{2}{1 - \tilde{z}_3 + (1 - x_{35,1})} - (1 + \tilde{z}_3) \right) |\mathcal{M}_B|^2,$$

where

$$x \equiv x_{35,1} = \frac{p_1 \cdot p_3 + p_1 \cdot p_5 - p_3 \cdot p_5}{(p_3 + p_5) \cdot p_1},$$

$$z \equiv \tilde{z}_3 = 1 - u_5 = \frac{p_1 \cdot p_3}{p_1 \cdot p_3 + p_1 \cdot p_5}.$$

The sum of these two dipoles give the dipole amplitude for diagrams with a final-state gluon,

$$|\mathcal{M}_D^{gf}|^2 = \mathcal{D}_3^{15} + \mathcal{D}_{35}^1 = 8\pi\alpha_s C_F \frac{1}{Q^2} \frac{x^2 + z^2}{(1-x)(1-z)} |\mathcal{M}_B^q(\tilde{p})|^2.$$

Note the evaluation of the Born amplitude in the called tilde kinematics, \tilde{p} , given by

$$\tilde{p}_1 = xp_1, \quad \tilde{p}_3 = p_3 + p_5 - (1-x)p_1.$$

Subtracting the dipole term from the real amplitude,

$$\sigma_{real}^{NLO} = \int_0^1 dx_a dx_b f_{q/p_1}(x_a, \mu_f) f_{q/p_2}(x_b, \mu_f) \frac{1}{2\hat{s}} d\Phi_5 \left[|\mathcal{M}_R^q|^2 F_J^{(3)} - |\mathcal{M}_D^{gf}|^2 F_J^{(2)} \right],$$

where the $F_J^{(n)}$ is an infrared-collinear safe algorithm with n final-state partons, the finite real cross-section with a final-state gluon for this process is obtained.

The dipoles for the crossed diagram, where the gluon is in the initial state, Fig. 3.8, are given by

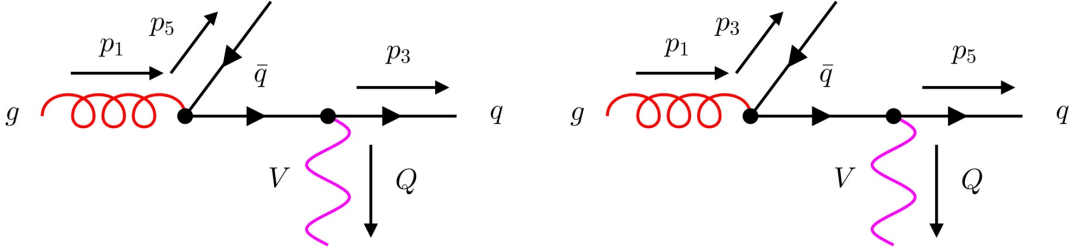


Figure 3.8: Feynman diagrams for the real emission with an initial-state gluon

$$\mathcal{D}_3^{15} = \frac{1}{2p_1 \cdot p_5} \frac{1}{x} 8\pi\alpha_s T_F (1 - 2x(1-x)),$$

$$\mathcal{D}_5^{13} = \frac{1}{2p_1 \cdot p_3} \frac{1}{x} 8\pi\alpha_s T_F (1 - 2x(1-x)),$$

whose sum reads

$$\begin{aligned} |\mathcal{M}_D^{g_i}| &= \mathcal{D}_3^{15} + \mathcal{D}_5^{13} \\ &= 8\pi\alpha_s T_F \frac{1 - 2x(1-x)}{x} \left(\frac{1}{2p_1 \cdot p_5} |\mathcal{M}_B^q(\tilde{p})|^2 + \frac{1}{2p_1 \cdot p_3} |\mathcal{M}_B^{\bar{q}}(\tilde{p})|^2 \right) \\ &= 8\pi\alpha_s T_F \frac{x^2 + (1-x)^2}{Q^2} \left(\frac{1}{1-z} |\mathcal{M}_B^q(\tilde{p})|^2 + \frac{1}{z} |\mathcal{M}_B^{\bar{q}}(\tilde{p})|^2 \right). \end{aligned}$$

Initial-state collinear divergences

Initial-state partons spoil the cancellation of the collinear divergences due to the fixed momentum of the initial parton. In the Catani-Seymour formalism, these are interpreted as renormalization factors of the PDF's, and are absorbed into them. The cross-section is then written as

$$\sigma_C = \int_0^1 dx_a \int_0^1 dx_b f_{q/p_1}^c(x_a, \mu_F, \mu_{Ra}) f_{q/p_2}(x_b, \mu_F) \times \quad (3.6)$$

$$\frac{\alpha_s}{2\pi} \int_{x_a}^1 \frac{dx}{x} \frac{1}{2\hat{s}} \int d\Phi_4 |\mathcal{M}_B^q|^2 F_J^{(2)}(p_2, p_3),$$

where the redefinition of the PDF's is given by

$$f_{q/p}^c(x_a, \mu_F, \mu_R) = f_{g/p}\left(\frac{x_a}{x}, \mu_F\right) A(x) +$$

$$\left[f_{q/p}\left(\frac{x_a}{x}, \mu_F\right) - x f_{q/p}(x_a, \mu_F) \right] B(x) + f_{q/p}\left(\frac{x_a}{x}, \mu_F\right) C(x)$$

$$+ f_{q/p}(x_a, \mu_F) \frac{D(x_a)}{1-x_a},$$

with

$$A(x) = T_F \left[x^2 + (1-x)^2 \right] \ln \frac{Q^2(1-x)}{\mu_F^2 x} + 2T_F x(1-x)$$

$$B(x) = C_F \left[\frac{2}{1-x} \ln \frac{Q^2(1-x)}{\mu_F^2} - \frac{3}{2} \frac{1}{1-x} \right]$$

$$C(x) = C_F \left[1-x - \frac{2}{1-x} \ln x - (1+x) \ln \frac{Q^2(1-x)}{\mu_F^2 x} \right]$$

$$D(x_a) = C_F \left[\frac{3}{2} \ln \frac{Q^2}{\mu_F^2(1-x_a)} + 2 \ln(1-x_a) \ln \frac{Q^2}{\mu_F^2} + \ln^2(1-x_a) + c_{real} \right].$$

Eq. (3.6) is integrated over the final state particles of the Born configuration. In VBFNLO, this integration is performed in the real amplitude phase space. These can be achieved noting that

$$\int d\Phi_{n+1} = \int_0^1 dx \int_0^1 dz \int d\Phi_n \frac{Q^2}{16\pi^2 x},$$

allowing us to write the final amplitude for the initial-state collinear configuration as

$$\sigma_C = \int_0^1 dx_a \int_0^1 dx_b \int d\Phi_5 f_{q/p_1}^c(x_a, x, \mu_F, \mu_{Ra}) f_{q/p_2}(x_b, \mu_F) \frac{4\pi\alpha_s}{Q^2} \frac{1}{2\hat{s}} |\mathcal{M}_B^q|^2 F_J^{(2)}.$$

In the code, this is done in the file `VBFNLO/amplitudes/vvjj/m2s_qqZjqq.F`.

3.2.3 Virtual contributions

In the following, the one-loop virtual contributions are described. The VBS approximation simplifies the one-loop corrections since loop diagrams connecting the upper and lower quark lines are discarded. Hence, we have to compute loop corrections to the quark line with one, two or three vector bosons attached.

The topology with one vector boson attached to the quark line results in a vertex one-loop correction. Likewise, corrections involving the quark line with two vector bosons,

one on-shell photon and the off-shell vector boson connecting both quark lines, give rise up to one-loop box corrections. Finally, up to pentagon corrections appear when two on-shell photons are attached to the same quark line.

Similarly to the Born and Real contributions, these diagrams are computed using universal in-house VBFNLO routines which can be used for different processes. To be comprehensive, we explain in detail how the one-loop corrections are calculated in the case when one photon is attached to the quark line.

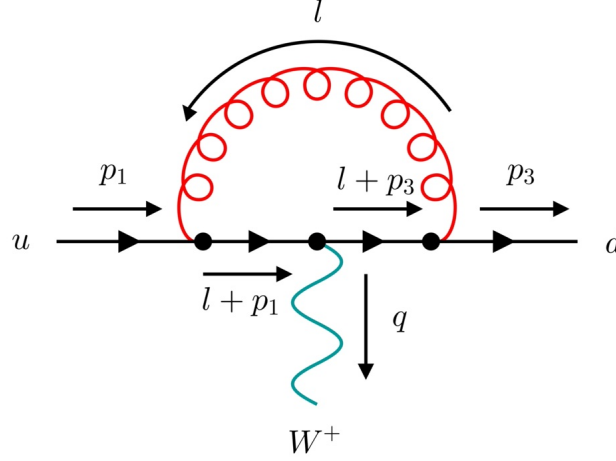


Figure 3.9: Feynman diagram representing the one-loop correction to the qqW^+ vertex.

Using the Feynman rules, we can write the amplitude corresponding to Fig. 3.9 as

$$i\mathcal{M}_\mu = \int \frac{d^d l}{(2\pi)^d} \bar{u}(p_3) (-i\mu^{\frac{d-4}{2}} g_s \gamma^\nu T_{ij}^a) \frac{i(p_3 + l)}{(p_3 + l)^2 + i\epsilon} \\ \times (-i\frac{g_W}{\sqrt{2}} \gamma_\mu P_L) \frac{i(p_1 + l)}{(p_1 + l)^2 + i\epsilon} \frac{-ig_{\sigma\nu}}{l^2 + i\epsilon} (-i\mu^{\frac{d-4}{2}} g_s \gamma^\sigma T_{ji}^a) u(p_1),$$

which after factoring out the couplings and color factors becomes

$$\mathcal{M}_\mu = i\frac{g_W}{\sqrt{2}} \mu^{d-4} g_s^2 C_F \int \frac{d^d l}{(2\pi)^d} \bar{u}(p_3) \frac{\gamma^\nu (p_3 + l) \gamma_\mu P_L (p_1 + l) \gamma_\nu}{(l^2 + i\epsilon)[(p_3 + l)^2 + i\epsilon][(p_1 + l)^2 + i\epsilon]} u(p_1). \quad (3.7)$$

The numerator can be simplified using the γ^μ properties. In particular,

$$\gamma^\nu \gamma^\alpha \gamma^\mu P_L \gamma^\beta \gamma_\nu = -2\gamma^\beta \gamma^\mu \gamma^\alpha P_L + 2a^{CDR} \gamma^\alpha \gamma^\mu \gamma^\beta P_L, \quad (3.8)$$

where $P_L = 1/2(1 - \gamma_5)$ is the projector onto the left-handed component of the spinors, and $a^{CDR} = 1$ in **conventional dimensional regularization** (DR) where the momenta and Dirac matrices dimension are taken to d -dimensions, and $a^{CDR} = 0$ in **dimensional reduction** (DREG) where only the momenta of the particles is d -dimensional and everything else is 4-dimensional. Then, using Eq. (3.8) in Eq. (3.7), factorizing out the Dirac structures, and removing the $i\epsilon$ to simplify the notation, the amplitude is given by

$$\mathcal{M}_\mu = i\frac{g_W}{\sqrt{2}} \mu^{d-4} g_s^2 C_F \bar{u}(p_3) (-2\gamma_\beta \gamma_\mu \gamma_\alpha P_L + 2a^{CDR} \gamma_\alpha \gamma_\mu \gamma_\beta P_L) u(p_1) \times \\ \left[p_3^\alpha p_1^\beta \int \frac{d^d l}{(2\pi)^d} \frac{1}{l^2 (p_3 + l)^2 (p_1 + l)^2} + p_3^\alpha \int \frac{d^d l}{(2\pi)^d} \frac{l^\beta}{l^2 (p_3 + l)^2 (p_1 + l)^2} + \right. \\ \left. p_1^\beta \int \frac{d^d l}{(2\pi)^d} \frac{l^\alpha}{l^2 (p_3 + l)^2 (p_1 + l)^2} + \int \frac{d^d l}{(2\pi)^d} \frac{l^\alpha l^\beta}{l^2 [(p_3 + l)^2 (p_1 + l)^2]} \right],$$

which after substituting the integrals in the Passarino-Veltman decomposition

$$\begin{aligned} \frac{1}{i\pi^2} \int \frac{1}{l^2(p_3+l)^2(p_1+l)^2} &= C_0(0, 0, -2p_1 \cdot p_3, 0, 0, 0), \\ \frac{1}{i\pi^2} \int \frac{l^\alpha}{l^2(p_3+l)^2(p_1+l)^2} &= (p_1 + p_3)^\alpha C_1(0, -2p_1 \cdot p_3, 0, 0, 0, 0), \\ \frac{1}{i\pi^2} \int \frac{l^\alpha l^\beta}{l^2(p_3+l)^2(p_1+l)^2} &= \\ &g^{\alpha\beta} C_{00}(0, -2p_1 \cdot p_3, 0, 0, 0, 0) + (p_1^\alpha p_1^\beta + p_3^\alpha p_3^\beta) C_{11}(0, -2p_1 \cdot p_3, 0, 0, 0, 0) \\ &+ (p_1^\beta p_3^\alpha + p_1^\alpha p_3^\beta) C_{12}(0, -2p_1 \cdot p_3, 0, 0, 0, 0) \end{aligned}$$

and using the Dirac equation, results in

$$\begin{aligned} \mathcal{M} &= -\frac{\pi^2 C_F g_s^2}{(2\pi)^d} \mathcal{M}_B \times \\ &[2q^2 C_0(0, 0, q^2, 0, 0, 0) - (a^{CDR}(d-4) + 2) ((d-2)C_{00}(0, q^2, 0, 0, 0, 0) \\ &- q^2 C_{12}(0, q^2, 0, 0, 0, 0)) + 4q^2 C_1(0, q^2, 0, 0, 0, 0)]. \end{aligned} \quad (3.9)$$

The coefficients C_1 , C_{00} , C_{11} and C_{12} corresponding to the decomposition of the tensor integrals can be reduced using the method explained in Sec. 2.3.4 to the bubble, B_0 , and triangle, C_0 , scalar integrals as

$$\begin{aligned} C_1(0, q^2, 0, 0, 0, 0) &= \frac{B_0(q^2, 0, 0)}{q^2} - \frac{B_0(0, 0, 0)}{q^2}, \\ C_{00}(0, q^2, 0, 0, 0, 0) &= -\frac{B_0(q^2, 0, 0)}{2(2-d)}, \\ C_{11}(0, q^2, 0, 0, 0, 0) &= \frac{B_0(0, 0, 0)}{2q^2} - \frac{B_0(q^2, 0, 0)}{2q^2}, \\ C_{12}(0, q^2, 0, 0, 0, 0) &= -\frac{(4-d)B_0(q^2, 0, 0)}{2(2-d)q^2}. \end{aligned} \quad (3.10)$$

In VBFNLO, the tensor integral coefficients are calculated numerically using recursion relations such that tensor integrals with rank N and M particles attached to the loop, $T^{\mu_1 \dots \mu_N}(x_1, \dots, x_M)$, are computed in terms of $T^{\mu_1 \dots \mu_{N-1}}(x_1, \dots, x_M)$, following the method in Sec. 2.3.4. The inversion of the Gram matrix, Eq. (2.26), is performed numerically using the LU decomposition, which provides a more reliable method to invert a matrix.

After the substitution of the reduced coefficients, Eq. (3.10), into Eq. (3.9), the matrix element is given by

$$\begin{aligned} \mathcal{M} &= \frac{\pi^2 C_F g_s^2}{(2\pi)^{4-2\epsilon}} \mathcal{M}_B \times \\ &[-(a^{CDR} + 1)\epsilon - 3) B_0(q^2, 0, 0) + 4B_0(0, 0, 0) - 2q^2 C_0(0, 0, q^2, 0, 0, 0)]. \end{aligned} \quad (3.11)$$

The scalar integrals B_0 and C_0 are analytically calculated. The scaleless bubble integral $B_0(0, 0, 0)$ formally vanishes in d -dimension, but it is separately divergent in the infrared and ultraviolet regimes. These two regions can be separated using an intermediate scale Λ and its poles calculated, which gives

$$B_0(0, 0, 0) = \frac{(4\pi)^{\epsilon_{UV}}}{\Gamma(1 - \epsilon_{UV})} \frac{1}{\epsilon_{UV}} - \frac{(4\pi)^{\epsilon_{IR}}}{\Gamma(1 - \epsilon_{IR})} \frac{1}{\epsilon_{IR}}. \quad (3.12)$$

The bubble integral with momentum q is ultraviolet divergent but infrared finite and reads

$$B_0(q^2, 0, 0) = \left(\frac{4\pi\mu^2}{-q^2} \right)^{\epsilon_{UV}} \frac{1}{\Gamma(1 - \epsilon_{UV})} \left(\frac{1}{\epsilon_{UV}} + 2 \right). \quad (3.13)$$

Finally, the scalar triangle integral is ultraviolet finite but infrared divergent,

$$C_0(0, 0, q^2, 0, 0, 0) = \left(\frac{4\pi\mu^2}{-q^2} \right)^{\epsilon_{IR}} \frac{1}{\Gamma(1 - \epsilon_{IR})} \frac{1}{q^2} \frac{1}{\epsilon_{IR}^2}. \quad (3.14)$$

Substituting Eq. (3.12), Eq. (3.13) and Eq. (3.14) into Eq. (3.11), the amplitude reads

$$\mathcal{M}_V = \frac{\alpha_s^2}{4\pi} C_F \left(\frac{4\pi\mu^2}{-q^2} \right)^\epsilon \frac{1}{\Gamma(1 - \epsilon)} \mathcal{M}_B \left[-\frac{2}{\epsilon_{IR}^2} - \frac{4}{\epsilon_{IR}} + \frac{1}{\epsilon_{UV}} - (a^{CDR} + 7) \right], \quad (3.15)$$

which is IR and UV divergent, with the UV divergent part given by

$$\mathcal{M}_{UV} = \frac{\alpha_s^2}{4\pi} C_F \mathcal{M}_B \frac{(4\pi)^{\epsilon_{UV}}}{\Gamma(1 - \epsilon_{UV})} \frac{1}{\epsilon_{UV}}.$$

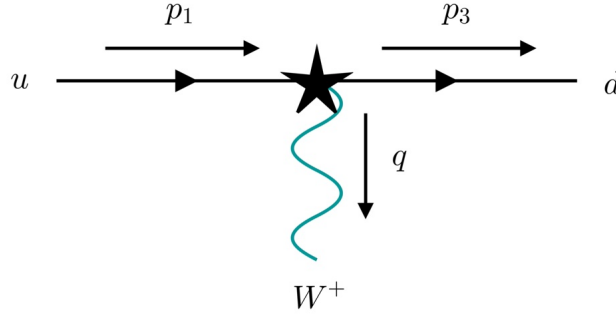


Figure 3.10: Vertex counterterm.

To remove the ultraviolet divergent part from the amplitude, Eq. (3.15), we need to renormalize the parameters involved in the vertex. This is done introducing the counterterm diagram Fig. 3.10 which gives

$$\mathcal{M}_{CT} = - \left(\frac{Z_{gW}}{Z_q \sqrt{Z_W}} - 1 \right) \mathcal{M}_B = - \left(\delta_{gW} - \delta_q - \frac{\delta_W}{2} \right) \mathcal{M}_B.$$

The electroweak coupling, g_W and the W wave function do not receive corrections at NLO QCD, so their counterterms are zero,

$$\delta_{gW} = \delta_W = 0.$$

The quark wave function counterterm in $\overline{\text{MS}}$ is given by

$$\delta_q = -\frac{\alpha_s}{4\pi} C_F \mathcal{M}_B B_0(0, 0, 0)$$

The renormalized result reads

$$\mathcal{M}_{V+CT} = \frac{\alpha_s^2}{4\pi} C_F \left(\frac{4\pi\mu^2}{-q^2} \right)^{\epsilon_{IR}} \frac{1}{\Gamma(1 - \epsilon_{IR})} \mathcal{M}_B \left[-\frac{2}{\epsilon_{IR}^2} - \frac{3}{\epsilon_{IR}} - (a^{CDR} + 7) \right],$$

which is UV finite but IR divergent. Contracting the result with the Born amplitude, we get the one-loop virtual correction of the W^+ vertex as

$$2 \operatorname{Re}(\mathcal{M}_{V+CT}\mathcal{M}_B^*) = |\mathcal{M}_B|^2 \frac{\alpha_s}{2\pi} C_F \left(\frac{4\pi\mu^2}{Q^2} \right)^\epsilon \Gamma(1+\epsilon) \left[-\frac{2}{\epsilon^2} - \frac{3}{\epsilon} + c_{virt} \right],$$

where we have written $\epsilon = \epsilon_{IR}$; $Q^2 = -q^2$, due to $q^2 < 0$; and multiplied by $\Gamma(1-\epsilon)\Gamma(1+\epsilon)$ to adjust to the VBFNLO convention; and the c_{virt} are defined as

$$c_{virt} = \frac{\pi^2}{3} - 7 \quad (\text{DREG}), \quad c_{virt} = \frac{\pi^2}{3} - 8 \quad (\text{DR}).$$

To remove the remaining IR-singularities, we have to integrate the dipoles calculated in the real contribution over the emitted parton phase space. Using Eq. (2.38),

$$\langle \mathbf{I}(\epsilon) \rangle = |\mathcal{M}_B|^2 \frac{\alpha_s(\mu)}{2\pi} C_F \left(\frac{4\pi\mu^2}{Q^2} \right)^\epsilon \Gamma(1+\epsilon) \left[\frac{2}{\epsilon^2} + \frac{3}{\epsilon} + 9 - \frac{4\pi^2}{3} \right],$$

and summing the corrections over the two quarklines independently, the result for the vertex correction is given by

$$\begin{aligned} \sigma^{B+V} = & \int_0^1 dx_a \int_0^1 dx_b f_{u/p_1}(x_a, \mu_F) f_{d/p_2}(x_b, \mu_F) \frac{1}{2\hat{s}} d\Phi_4 \\ & \times |\mathcal{M}_B|^2 F_J^{(2)} \left[1 + \frac{\alpha_s(\mu_a) + \alpha_s(\mu_b)}{2\pi} C_F \left(9 - \frac{4\pi^2}{3} + c_{virt} \right) \right], \end{aligned}$$

where $F_J^{(2)}$ is an infrared-collinear safe jet algorithm with two final-state partons.

There are corrections to the quark line with two or three vector bosons attached. We group together all possible loop corrections to a given leading order diagram in a given fixed leg permutation. i.e. for a quark line with two vector bosons attached, $V_1 V_2$, we built the so-called boxline routine, Fig. 3.11, which contains one box, two vertices, and one self-energy diagram. Similarly, the penline routine, Fig. 3.12, comprises eight one-loop diagrams: one pentagon, two boxes, three vertices and two self-energy diagrams containing all possible loop diagrams to a quark line with three vector bosons emitted in a fixed order permutation.

The IR poles are exactly the same that in the vertex case since the $\mathbf{I}(\epsilon)$ -operator, from QCD origin, is blind to the number of electroweak particles attached to the quark line. Also, the vertex correction in each of these sets give the dominant contribution. So, we will split the calculation of these sets into the vertex contribution, including the poles, and a finite remainder as seen in Eq. (3.16).

The contribution from the box quark line virtual corrections was calculated using a Mathematica code, whose detailed explanation can be found in Ref. [54], which exploits the techniques explained for the calculation of the vertex correction and the helicity amplitude method. It writes the amplitude to a FORTRAN code in terms of tensor integrals which are evaluated numerically using the Passarino-Veltman recursion relations explained in Sec. 2.3.4. The result for the boxline correction is written as

$$\begin{aligned} \mathcal{M}_V^{(i)} = & \mathcal{M}_B^{(i)} \frac{\alpha_s(\mu_R)}{4\pi} C_F \left(\frac{4\pi\mu_R^2}{Q^2} \right)^\epsilon \Gamma(1+\epsilon) \left[-\frac{2}{\epsilon^2} - \frac{3}{\epsilon} + c_{virt} \right] \\ & + \frac{\alpha_s(\mu_R)}{4\pi} C_F \tilde{\mathcal{M}}_{V_1 V_2, \tau}^{(i)}(q_1, q_2) e^2 g_\tau^{V_1 f_1} g_\tau^{V_2 f_2} + \mathcal{O}(\epsilon). \end{aligned} \quad (3.16)$$

The following FORTRAN subroutine

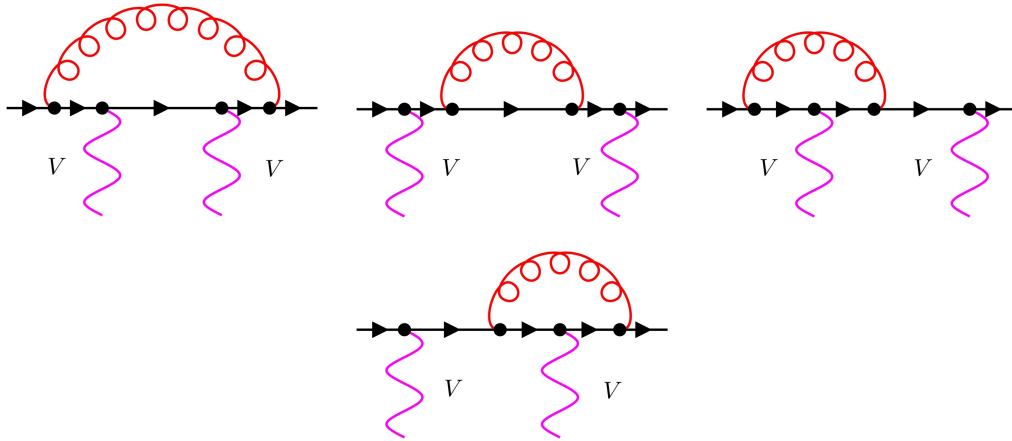


Figure 3.11: Diagrams contributing to the box corrections of the quark-line. These diagrams are implemented in VBFNLO and used in our process through the `boxlineABETotal` subroutine.

```
subroutine boxlineABETotal
```

which is located inside `VBFNLO/amplitudes/vvjj/VBF_BOX_ABE_CURRENT.F`, calculates all diagrams with two vector bosons emitted from a quark line, Fig. 3.11. Then, the one-loop correction is given by replacing the tree-level diagrams with the corresponding one-loop subroutine.

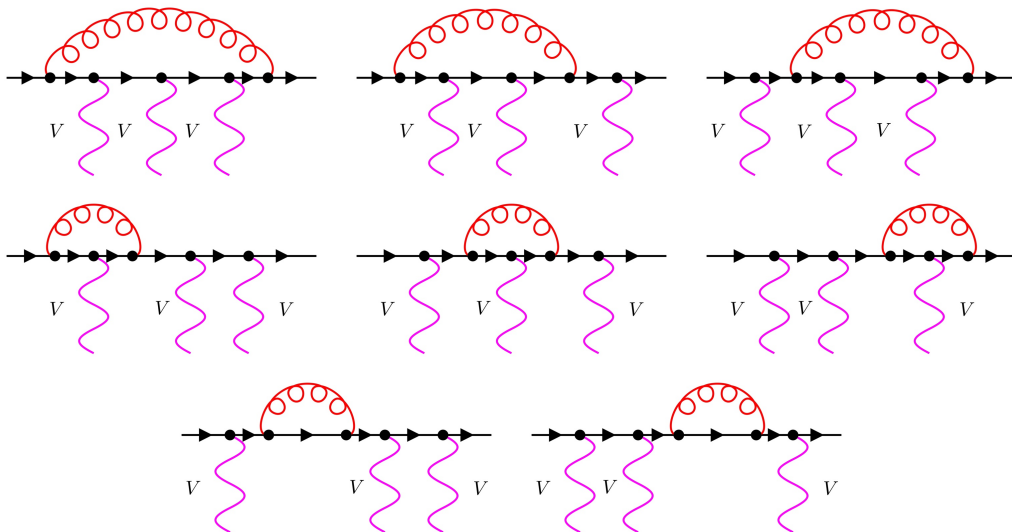


Figure 3.12: Diagrams contributing to the Penline subroutine that gives the one-loop corrections to a quark line with three vector bosons attached.

The penline contribution, seen in Fig. 3.12 is calculated using the Denner-Dittmaier reduction procedure [52, 54], which avoids the problem of small Gram determinants occurring in pentagons with planar configurations of the external momenta, and the result can be

written as:

$$\begin{aligned} \mathcal{M}_V^{(i)} = & \mathcal{M}_B^{(i)} \frac{\alpha_s(\mu_R)}{4\pi} C_F \left(\frac{4\pi\mu_R^2}{Q^2} \right)^\epsilon \Gamma(1+\epsilon) \left[-\frac{2}{\epsilon^2} - \frac{3}{\epsilon} + c_{virt} \right] \\ & + \frac{\alpha_s(\mu_R)}{4\pi} C_F \tilde{\mathcal{M}}_{V_1 V_2 V_3, \tau}^{(i)}(q_1, q_2) e^2 g_\tau^{V_1 f_1} g_\tau^{V_2 f_2} g_\tau^{V_3 f_3} + \mathcal{O}(\epsilon). \end{aligned}$$

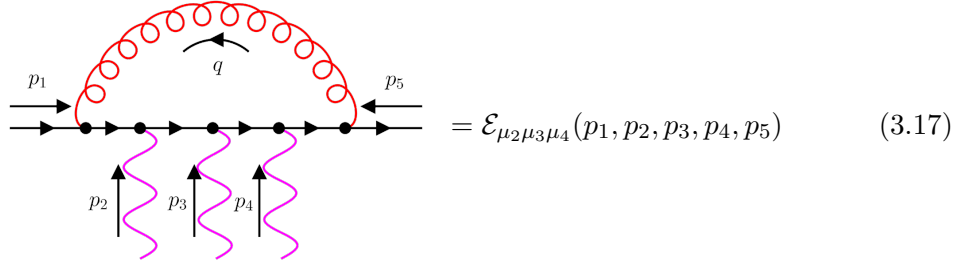
Analogously, all diagrams with three vector bosons attached can be computed at one-loop level by replacing the tree amplitude by the corresponding one-loop subroutine

`subroutine penlineABETotal`

The numerical instabilities due to the presence of small Gram determinants in degenerate kinematical configurations is controlled using **Ward-Takahashi identities**. The pentagon correction to a quark line, Eq. (3.17), with three off-shell vector bosons is given by:

$$\mathcal{E}_{\mu_2 \mu_3 \mu_4}(p_1, p_2, p_3, p_4, p_5) = \int \frac{d^d q}{(2\pi)^d} \left[\frac{1}{q^2} \gamma^\nu \frac{1}{\not{q} + \not{p}_{14}} \gamma_{\mu_4} \frac{1}{\not{q} + \not{p}_{13}} \gamma_{\mu_3} \frac{1}{\not{q} + \not{p}_{12}} \gamma_{\mu_2} \frac{1}{\not{q} + \not{p}_1} \gamma_\nu \right],$$

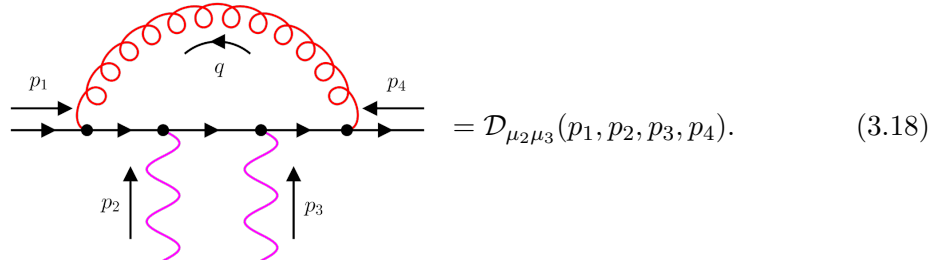
where global constants have been omitted for simplicity.



If any of the free indices is contracted with its corresponding momentum vector, the pentagon correction becomes the difference of two boxes with different momentum assignments:

$$\begin{aligned} p_2^{\mu_2} \mathcal{E}_{\mu_2 \mu_3 \mu_4}(p_1, p_2, p_3, p_4, p_5) &= [(q + p_{12})^{\mu_2} - (q + p_1)^{\mu_2}] \mathcal{E}_{\mu_2 \mu_3 \mu_4}(p_1, p_2, p_3, p_4, p_5) \\ &= \int \frac{d^d q}{(2\pi)^d} \left[\frac{1}{q^2} \gamma^\nu \frac{1}{\not{q} + \not{p}_{14}} \gamma_{\mu_4} \frac{1}{\not{q} + \not{p}_{13}} \gamma_{\mu_3} \left(\frac{1}{\not{q} + \not{p}_1} - \frac{1}{\not{q} + \not{p}_{12}} \right) \gamma_\nu \right] \\ &= \mathcal{D}_{\mu_3 \mu_4}(p_1, p_2 + p_3, p_4, p_5) - \mathcal{D}_{\mu_3 \mu_4}(p_1 + p_2, p_3, p_4, p_5), \end{aligned}$$

where the box contribution $\mathcal{D}_{\mu\nu}$ is defined in Eq. (3.18),



Similarly, contracting the other free indices with its corresponding momentum vector, the following relations are obtained:

$$\begin{aligned} p_3^{\mu_3} \mathcal{E}_{\mu_2\mu_3\mu_4}(p_1, p_2, p_3, p_4, p_5) &= \mathcal{D}_{\mu_2\mu_4}(p_1, p_2, p_3 + p_4, p_5) - \mathcal{D}_{\mu_2\mu_4}(p_1, p_2 + p_3, p_4, p_5), \\ p_4^{\mu_4} \mathcal{E}_{\mu_2\mu_3\mu_4}(p_1, p_2, p_3, p_4, p_5) &= \mathcal{D}_{\mu_2\mu_3}(p_1, p_2, p_3, p_4 + p_5) - \mathcal{D}_{\mu_2\mu_3}(p_1, p_2, p_3 + p_4, p_5). \end{aligned}$$

The boxes are decomposed in an analogous manner to the difference of vertex corrections, which are calculated analytically with the procedure shown in this section.

These relations are calculated in VBFNLO, and they are required to be satisfied with a certain accuracy, ϵ , typically 10^{-2} for VBS processes. Large deviations in these relations are due to numerical instabilities, mainly to the appearance of small Gram determinants. The identification of unstable points using these relations allows us to set the event weight to zero, maintaining the stability of the code, if the error induced is small, or to set up rescue procedures recalculating the scalar and tensor coefficient integrals in quadruple precision and/or using dedicated subroutines for small Gram determinants.

3.2.4 Anomalous Couplings

In VBFNLO, the implementation of the operators discussed in Sec. 2.2 is done through a modification of the EW gauge couplings, which are then called **anomalous couplings** (AC). The dimension-6 operators modify the TGC which in the code is carried out in the file `VBFNLO/helas/anoma13.F`, while the dimension-8 operators modify the QGC and their implementation can be found in the file `VBFNLO/helas/anoma14.F`. The combination of leptonic tensors and anomalous couplings makes the implementation of the effective theory operators straightforward, changing the existing leptonic tensors by the anomalous ones. In our case, we use

```
subroutine wwtoa_anomal(p1, p2, h, TWW→γγμν)
```

instead of `wwtoa`, and

```
subroutine calc_wwtoa2_anomal(idW, h, k, εhμ(k), pidW, TWW→γγμν)
```

instead of `calc_wwtoa2`, both found in the file `VBFNLO/amplitudes/vvjj/toaa_anomal.F`.

3.3 Checks

In this section, the tests used to ensure the correct implementation of the different parts of the process are introduced.

Comparison between Sherpa and VBFNLO

The LO cross-section has been checked comparing it to the result given by the MC event generator Sherpa. The SM parameters in the comparison runs used were:

$$\begin{aligned} E_{CM} &= 14 \text{ TeV}, & \alpha_s &= 0.129783, \\ G_F &= 1.16637 \cdot 10^{-5} \text{ GeV}^{-2}, & m_W &= 80.398 \text{ GeV}, & m_Z &= 91.1876 \text{ GeV}. \end{aligned}$$

The EWSCHEME is set to 3 in VBFNLO, which means that G_F , m_Z , and m_W are input parameters, and the rest are calculated using tree-level relations to ensure consistency. The jets were defined using the anti- k_T algorithm from partons with $|y_{parton}| < 4.5$. Additionally, we used the following cuts for the jets and the photons

$$\begin{aligned} p_{T,j} &> 30 \text{ GeV}, & |y_j| &< 4.5, \\ p_{T,\gamma} &> 20, 30 \text{ GeV}, & |y_\gamma| &< 2.5, \\ \Delta R_{jj} &> 0.4, & \Delta R_{\gamma\gamma} &> 0.4, & \Delta R_{j\gamma} &> 0.7. \end{aligned}$$

Since the process in VBFNLO has been implemented in the VBS approximation, the following VBS cuts were used to ensure the validity of the approximation, see Ref. [86].

$$\begin{aligned} m_{j_1 j_2} &> 600 \text{ GeV}, \\ |y_{j_1} - y_{j_2}| &> 4, \\ y_{j_1} \cdot y_{j_2} &< 0. \end{aligned}$$

The results at LO for two different values of the $p_{T,\gamma}$ cut are shown in Table [3.3] where we

Process	VBFNLO σ [fb]	SHERPA σ [fb]	Deviation
$pp \rightarrow \gamma\gamma jj$ ($p_T = 20\text{GeV}$)	60.631 ± 0.017	60.60 ± 0.03	0.04%
$pp \rightarrow \gamma\gamma jj$ ($p_T = 30\text{GeV}$)	31.668 ± 0.010	31.656 ± 0.017	0.04%

Table 3.3: Comparison of the LO cross-section between VBFNLO and Sherpa of the $pp \rightarrow \gamma\gamma jj$ for two different values of the $p_{\gamma,T}$.

can see an agreement below the per-mille level for both values of the transverse momentum. For the real contribution, the same analysis was done, and the results are shown in Table [3.4] with an agreement of about 2%. The discrepancy is due to the neglected s-channel

Process	VBFNLO σ [fb]	SHERPA σ [fb]	Deviation
$pp \rightarrow \gamma\gamma jjj$ ($p_T = 20\text{GeV}$)	12.84 ± 0.02	13.097 ± 0.010	2%
$pp \rightarrow \gamma\gamma jjj$ ($p_T = 30\text{GeV}$)	7.195 ± 0.004	7.325 ± 0.004	1.77%

Table 3.4: Comparison of the cross-section at LO of the real contribution $pp \rightarrow \gamma\gamma jjj$ between VBFNLO and Sherpa for two different values of the $p_{\gamma,T}$.

contributions. We can use Sherpa to calculate all s-channel contributions, and subtract them from the complete result. The different s-channel contributions calculated with Sherpa can be seen in Table [3.5]. The subtracted result, Table [3.6], shows now a much better agreement.

Dipole subtraction

To test the correct implementation of the Catani-Seymour dipole subtraction, we checked the real contribution behavior near the divergent regions. The subtracted real contribution must have a finite value while the unsubtracted contribution will diverge in the collinear and soft regions, meaning the quotient of the subtracted versus unsubtracted contributions will go to zero. This is shown in Fig. [3.13], where the ratio goes to zero when p_1 is collinear to p_5 , with p_5 the momentum of the emitted gluon, or E_g goes to zero.

Process	SHERPA σ [fb]
$pp \rightarrow \gamma(\gamma)^*j; (\gamma)^* \rightarrow jj$ ($p_T = 20\text{GeV}$)	$(5.910 \pm 0.002) \cdot 10^{-4}$
$pp \rightarrow \gamma(\gamma)^*j; (\gamma)^* \rightarrow jj$ ($p_T = 30\text{GeV}$)	$(3.3309 \pm 0.0010) \cdot 10^{-4}$
$pp \rightarrow \gamma(W^+)^*j; (W^+)^* \rightarrow jj$ ($p_T = 20\text{GeV}$)	$(8.31 \pm 0.02) \cdot 10^{-2}$
$pp \rightarrow \gamma(W^+)^*j; (W^+)^* \rightarrow jj$ ($p_T = 30\text{GeV}$)	$(4.599 \pm 0.015) \cdot 10^{-2}$
$pp \rightarrow \gamma(W^-)^*j; (W^-)^* \rightarrow jj$ ($p_T = 20\text{GeV}$)	$(8.86 \pm 0.03) \cdot 10^{-2}$
$pp \rightarrow \gamma(W^-)^*j; (W^-)^* \rightarrow jj$ ($p_T = 30\text{GeV}$)	$(4.80 \pm 0.02) \cdot 10^{-2}$
$pp \rightarrow \gamma(Z)^*j; (Z)^* \rightarrow jj$ ($p_T = 20\text{GeV}$)	$(8.824 \pm 0.002) \cdot 10^{-2}$
$pp \rightarrow \gamma(Z)^*j; (Z)^* \rightarrow jj$ ($p_T = 30\text{GeV}$)	$(4.9154 \pm 0.0015) \cdot 10^{-2}$

Table 3.5: s-channel of the real contribution, $pp \rightarrow \gamma\gamma jjj$, at LO calculated using Sherpa for two different values of $p_{\gamma,T}$.

Process	VBFNLO σ [fb]	SHERPA σ [fb](no s-channel)	Deviation
$pp \rightarrow \gamma\gamma jjj$ ($p_T = 20\text{GeV}$)	12.84 ± 0.02	12.837 ± 0.010	0.02%
$pp \rightarrow \gamma\gamma jjj$ ($p_T = 30\text{GeV}$)	7.195 ± 0.004	7.181 ± 0.004	0.19%

Table 3.6: Comparison at LO of the real contribution, $pp \rightarrow \gamma\gamma jjj$, subtracting the s-channel contributions from the Sherpa cross-section for two different values of $p_{\gamma,T}$.

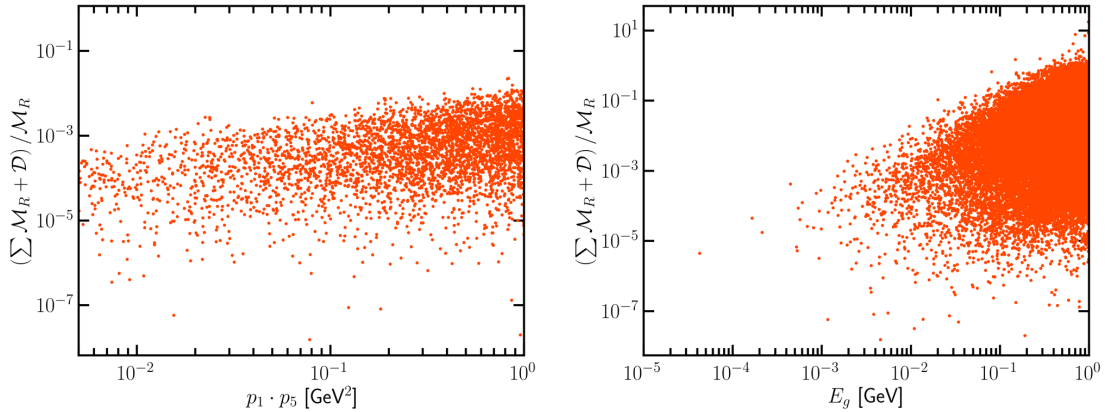


Figure 3.13: Figures showing the dipole subtraction in two problematic phase space regions; gluon getting collinear to a parton (left), soft gluon region (right).

Pole values

In the implementation section, we saw that the coefficients of the poles are $-2\mathcal{M}^B$ for the ϵ^2 pole and $-3\mathcal{M}^B$ for the ϵ pole in the calculation of the virtual contribution. The subroutines `boxlineABETotal` and `penlineABETotal` can also evaluate these poles numerically. If we divide the pole coefficient value given by the subroutines `boxlineABETotal` and `penlineABETotal` by \mathcal{M}^B the result should diverge from -2 or -3 , respectively, by the numerical errors due to the finite double precision.

The double precision floating point numbers allow approximately 16 decimal digits of precision. Rounding errors in the calculations, mainly due to the small Gram determinant instabilities, will decrease the number of significant decimal digits. In Fig. 3.14, the power in base 10 of the distance between the analytical and numerical value of the pole is given. There, we can see Poissonian curves around different negative values of the powers, which

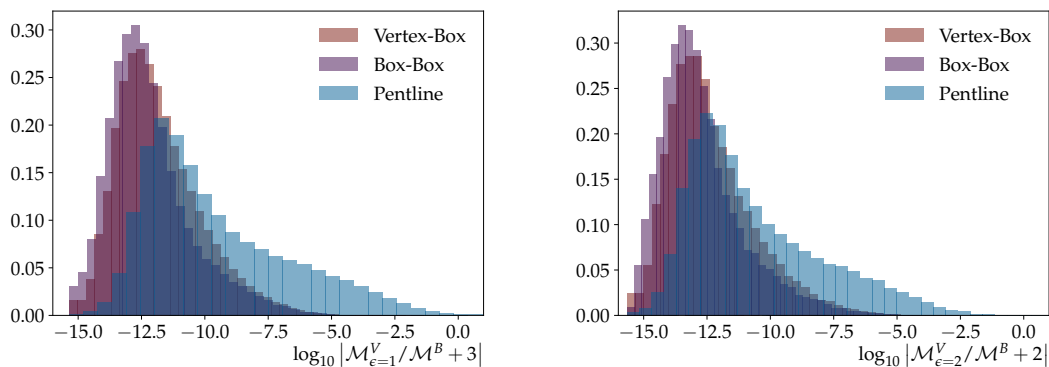


Figure 3.14: Normalized distributions showing the accuracy of the numerical calculation of the IR poles. Left figure shows the precision of the $1/\epsilon$ Laurent coefficient numerical calculation, while the right figure shows the $1/\epsilon^2$.

are related to different topologies. The curves are centered around -13 for the vertex-box and box-box topologies, and around -12 for the pentagon topologies. The behavior of the curves and their shape are similar for both poles, with the tail of the $1/\epsilon$ pole slightly longer. The long tail of the penline corrections is due to the larger number of small Gram determinant instabilities. As explained in Sec. 3.2, these are treated in VBFNLO using Ward-Takahashi identities. However, for these figures, the tests using the Ward-Takahashi identities have been deactivated.

Scale variation comparison

The process $pp \rightarrow e^+e^-\gamma jj$, where the electron positron pair come from the decay of a Z or γ boson, includes our process but with an off-shell photon. If we impose a cut allowing only events below the Z mass, the two processes will differ mainly by a factor due to the $\gamma \rightarrow e^+e^-$ vertex. If we normalize the cross-section, we expect to see the same scale dependency. This is demonstrated in Fig. 3.15, where there is a complete agreement between the normalized cross-section scale dependencies for both processes.

Ward identities

The gauge invariance of processes with final-state photons can be tested using the Ward identity

$$p^\mu \mathcal{M}_\mu = 0,$$

where p^μ is the momentum of one of the photons with polarization vector ϵ^μ , and \mathcal{M}_μ is defined such that

$$\mathcal{M} = \epsilon^\mu \mathcal{M}_\mu,$$

where \mathcal{M} is the matrix element of a gauge invariant subset of diagrams.

In Fig. 3.16, we show the value of the cross-section obtained by substituting the polarization vector corresponding to the photon labeled 1 by its momentum. The Born and Real contributions have distributions with a peak around -15 , and -13.5 , respectively, while the virtual corrections peak around -12.5 . These values are consistent with the double precision used in the calculation, which has 16 significant decimal digits. The loss of precision is due to rounding errors during the calculations, including the small Gram determinants. Analogously to the determination of the pole coefficient, the Ward-Takahashi

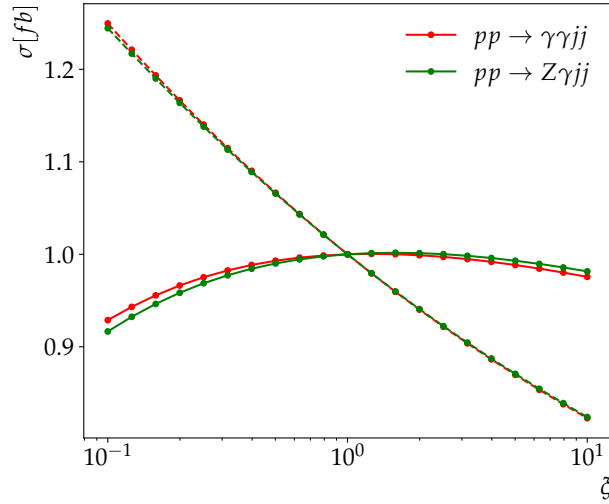


Figure 3.15: Scale variation dependency comparison between the $pp \rightarrow \gamma\gamma jj$ and $pp \rightarrow Z\gamma jj$ following the cuts described in the text. Both distributions have been normalized to the corresponding central value scale in order to correct for the different total cross-section due to the leptonic decay attached to the photon in the $pp \rightarrow Z\gamma jj$ process. The $pp \rightarrow \gamma\gamma jj$ process is represented in red with a continuous line for the NLO cross-section and a dashed line for the LO. Analogously, the $pp \rightarrow Z\gamma jj$ process is shown in green.

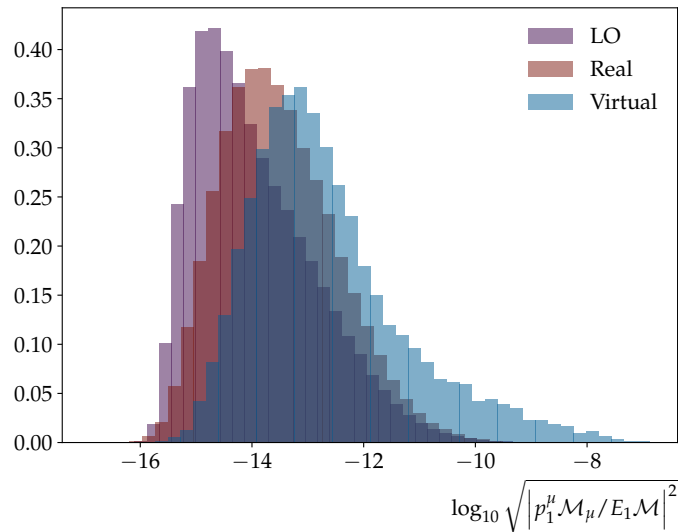


Figure 3.16: Distributions of the powers in base 10 of the Ward identity numerical errors.

tests have been deactivated for this check, which can be seen in the tail extending up to -7.5 in the virtual corrections.

3.4 Phenomenological Results

3.4.1 Parameters and cuts

In the following, the parameters and cuts used for the runs are presented, the Frixione Isolation and VBS cuts studied, and the scale variation for different scales shown. As SM input parameters, we use the values from the PDG, Ref. [33]:

$$m_t = 172.9 \text{ GeV}, \quad m_Z = 91.1876 \text{ GeV}, \quad m_W = 80.379 \text{ GeV}, \\ G_F = 1.1663787 \times 10^{-5} \text{ GeV}^{-2}.$$

The rest of the parameters are obtained from LO relations.

The jets are reconstructed from partons with $|y_{parton}| < 5$ using an anti-kt algorithm with $R = 0.4$. The jets and photons are required to have $p_T > 30 \text{ GeV}$, while the jets must have $|y| < 4.5$:

$$p_{T,j} > 30 \text{ GeV}, \quad |y_j| < 4.5, \\ p_{T,\gamma} > 30 \text{ GeV}, \quad |y_\gamma| < 2.5, \\ \Delta R_{\gamma\gamma} > 0.4, \quad \Delta R_{j\gamma} > 0.8.$$

The final-state particles are two jets and two photons at LO. These same final-state could also be achieved from the tri-boson process where the W^\pm or the Z decay hadronically; $pp \rightarrow W^\pm \gamma \gamma$, $W^\pm \rightarrow jj$ and $pp \rightarrow Z \gamma \gamma$, $Z \rightarrow jj$. To remove this phase space region, the following cut was implemented

$$\left| m_{jets} - \frac{M_W + M_Z}{2} \right| > 15 \text{ GeV}.$$

For our choice of scale, we use $H_T/2$ where H_T is defined as

$$H_T = \sum_{i \in partons} p_{T,i} + p_{T,\gamma_1} + p_{T,\gamma_2}. \quad (3.19)$$

The PDFs set used is PDF4LHC15 [96] obtained via the LHAPDF [97] library.

The VBS approximation cuts

The invariant mass of the two tagging jets and their rapidity separation have to be chosen such that the VBS approximation holds. We analyzed the impact of these cuts on the significance of our process for a luminosity of $L = 1 \text{ fb}^{-1}$, i.e. $\sigma_{EW}/\sqrt{\sigma_{QCD}}$. In Fig. 3.17, the maximum is located around $m_{j_1 j_2}^{cut} = 1280 \text{ GeV}$ and $\Delta y_{j_1 j_2}^{cut} = 2.6$, and variations of $\Delta y_{j_1 j_2}^{cut}$ has a mild effect on the significance, while the $m_{j_1 j_2}^{cut}$ has a major impact for values close to the maximum, between $m_{j_1 j_2}^{cut} = 800 \text{ GeV}$ and $m_{j_1 j_2}^{cut} = 2000 \text{ GeV}$ the significance is over 4 for $\Delta y_{j_1 j_2}^{cut} \leq 3$.

In Table 3.7, the total cross-section and significance for a discrete set of cut values are shown, where we see that changing $m_{j_1 j_2}^{cut} = 800 \text{ GeV}$ to $m_{j_1 j_2}^{cut} = 1000 \text{ GeV}$ has a minor impact on the significance but affects considerably the total cross-section. Thus, for our phenomenological analysis, we stick to the following values

$$m_{j_1 j_2} > 800 \text{ GeV}, \\ |y_{j_1} - y_{j_2}| > 3, \\ y_{j_1} y_{j_2} < 0. \quad (3.20)$$

The choice of $|y_{j_1} - y_{j_2}| > 3$ is to guarantee the validity of the VBS approximation Ref. [86]. These final values are tighter cuts than the ones usually used in the rest of VBS's processes, where the invariant mass of the two jets cut is usually around $m_{j_1 j_2}^{cut} = 400 \text{ GeV}$.

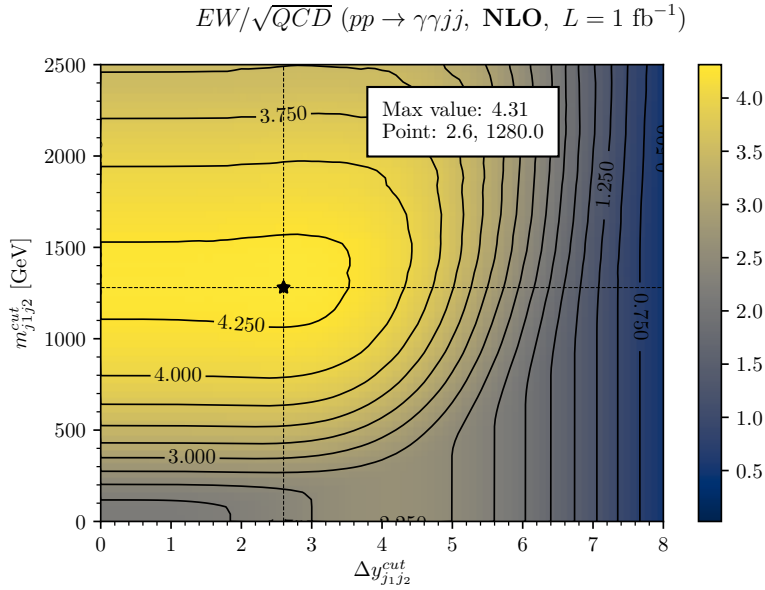


Figure 3.17: Significance, EW/\sqrt{QCD} , as a function of the VBS cuts: m_{j1j2}^{cut} and Δy_{j1j2}^{cut} .

m_{j1j2}^{cut} [GeV], Δy_{j1j2}^{cut}	EW	QCD	EW/\sqrt{QCD}
800, 2	25.41(2)	40.68(10)	3.98
800, 3	24.62(1)	38.53(3)	3.97
800, 4	21.29(1)	33.23(8)	3.69
600, 3	30.69(2)	72.8(2)	3.60
1000, 3	19.36(2)	21.66(6)	4.16

Table 3.7: Total cross-sections of the EW- and QCD-channel, and the significance, EW/\sqrt{QCD} , for a selected choice of values for the VBS cuts.

Scale dependence

In the calculation of the hadronic cross-sections at NLO, two unphysical scales appear: the factorization scale, μ_F , and the renormalization scale μ_R . The dependence on these two scales, being unphysical, must drop from physical observables if the full perturbative series is considered. However, the truncation of the series at a given order leaves a residual dependence which can be used to estimate the size of higher order corrections. To give an estimate of the theoretical uncertainty due to the missing terms, the upper and lower errors bounds are defined as the value of the cross-section for two times some central value scale and half the central value scale respectively.

The renormalization and factorization scale dependence of our process can be seen in Fig. 3.18 for four different scales, where we have set $\mu_F = \mu_R$ for simplicity. These four scales are: A fixed scale set at the Z mass, M_Z ; the square root of the two tagging jets p_T product, $\sqrt{p_{T,j1} p_{T,j2}}$; the momentum transfer at each quark line vertex, Q_i , where i enumerates the quark lines; and $H_T/2$ where H_T is given by Eq. (3.19).

We observe a reduction of the cross-section scale dependence at NLO. The difference between the maximum and minimum values of the cross-section in the full range is less at NLO than at LO. Also, the spread of the cross-sections for different choices of the scales are smaller for the NLO. The fixed scale M_Z has the largest difference between LO and

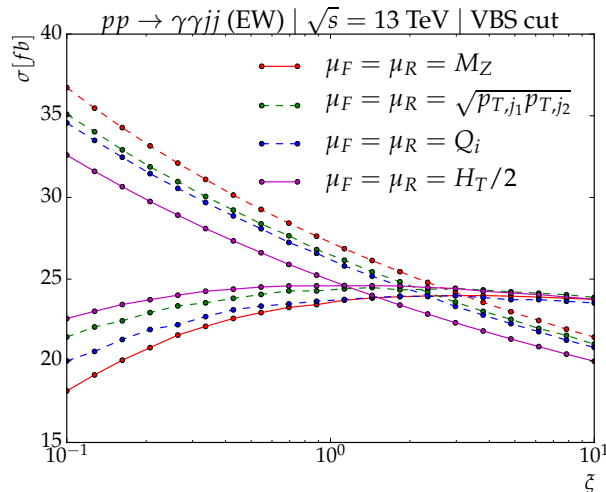


Figure 3.18: Scale dependence plots for four different scale choices with $\mu_R = \mu_F$. The upper curves are the scale dependence at LO, while the lower ones are at NLO.

NLO with a stronger scale dependency. The $H_T/2$ scale has almost the same value for LO and NLO at the central scale value, which means that we will get the smaller QCD corrections with this scale, with a little smaller LO cross-section and a bit bigger NLO cross-sections than the rest of the scales. Also, $H_T/2$ has the smaller scale dependency.

Frixione isolation cut

The Frixione isolation cut, used to remove the fragmentation photon component safely i.e. without spoiling the IR pole cancellation between the real and virtual contributions, has two different parameters: the efficiency, ϵ , and the cone angle, δ_0 . In the following, we study how changes in these parameters affect the total cross-section.

In Figure 3.19, we can see the cross-section and K-factors for the QCD and EW channels as a function of the efficiency for two different values of the cone radius. At LO, the two jets are just the two partons emitted in the hard process. Due to the generation cut allowing only events with $\Delta R_{j\gamma} > 0.8$, there is no dependency on the photon-isolation efficiency for $\delta_0 < 0.8$. At NLO an extra emission allows for the partons to be inside the isolation cone and the jets to fulfill $\Delta R_{j\gamma} > 0.8$. The cross-section is smaller for the bigger δ_0 because only the events where the parton is inside the photon-isolation cone can be thrown away. So, the bigger the cone, the bigger the chance for an event rejection.

In Table 3.8, the cross-sections for some selected values of ϵ is shown. In the VBS channel, the K-factor only changes by 0.02 for $\delta_0 = 0.4$ and by 0.05 for $\delta_0 = 0.7$, for efficiency variations between 0.01 and 1. For the QCD channel, the K-factor variation is much larger, being 0.57 for $\delta_0 = 0.4$ and 0.95 for $\delta_0 = 0.7$, with K-factors closer to one for small values of the efficiency.

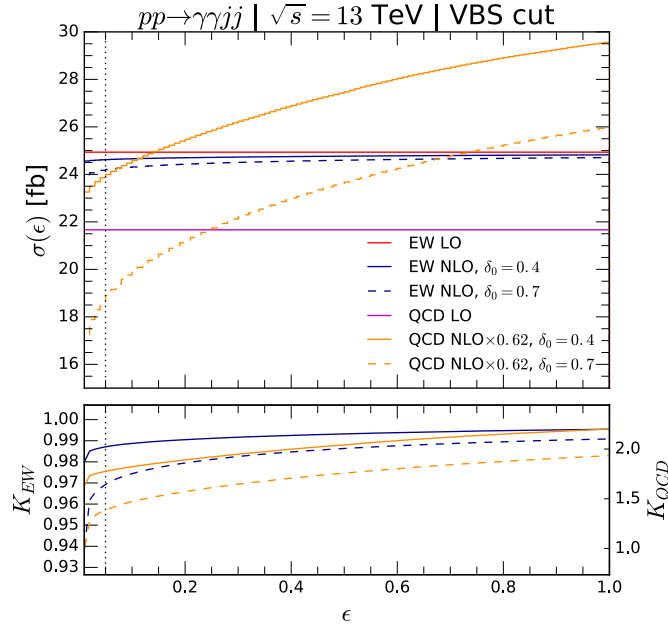


Figure 3.19: Frixione isolation cut study. The impact of the efficiency, ϵ , on the cross-sections for the QCD and EW channels. We can see the value of the LO, and NLO cross-sections for two different values of the cone radius, δ_0 .

δ_0	ϵ	EW NLO [fb]	K_{EW}	QCD NLO [fb]	K_{QCD}
0.4	0.01	24.4	0.98	35	1.63
	0.05	24.6	0.99	39	1.78
	0.5	24.8	0.99	44	2.04
	1.0	24.82(1)	1.00	47.7(1)	2.20
0.7	0.01	23.4	0.94	21	0.98
	0.05	24.2	0.97	30	1.39
	0.5	24.6	0.99	38	1.76
	1.0	24.705(9)	0.99	41.9(1)	1.93

Table 3.8: Frixione isolation cut study. We can see the value of the NLO cross-sections for the EW and QCD channels and their K -factors for four different values of the efficiency, ϵ , and two different values of the cone radius, δ_0 .

3.4.2 Comparisons with other VBS processes

In this subsection, we show a comparison with other VBS processes. Specifically, the processes with one on-shell photon and two leptons:

$$\begin{aligned}
 pp &\rightarrow Z\gamma jj \rightarrow l^+l^-jj; \\
 pp &\rightarrow W^+\gamma jj \rightarrow l^+\nu_l jj; \\
 pp &\rightarrow W^-\gamma jj \rightarrow l^-\bar{\nu}_l jj.
 \end{aligned}
 \tag{3.21}$$

We refer to the processes by the vector bosons involved and the number of jets, i.e. $Z\gamma jj$, but, despite this notation, all the off-shell effects and spin-correlations are taken into account.

Process	EW	QCD	EW/ $\sqrt{\text{QCD}}$
$\gamma\gamma jj$	24.62(1) $^{+0}_{-0.59\%}$	38.53(3) $^{+19\%}_{-16\%}$	4.0
$l^+l^-\gamma jj$	1.786(1) $^{+0}_{-0.84\%}$	0.883(2) $^{+10\%}_{-10\%}$	1.9
$l^+\nu_l\gamma jj$	9.009(7) $^{+0}_{-0.79\%}$	8.87(3) $^{+10\%}_{-33\%}$	3.0
$l^-\bar{\nu}_l\gamma jj$	5.401(4) $^{+0}_{-0.61\%}$	6.53(2) $^{+6\%}_{-24\%}$	2.1

Table 3.9: Total cross-section results for the processes in Eq. (3.21). In the first column, we can see the cross-section for the corresponding EW channel. In the second one, the total cross-section for the corresponding QCD channel. The last column has the significance for the EW channel, assuming as only background the QCD channel, with $L = 1 \text{ fb}^{-1}$.

The cuts for the leptons and neutrinos are:

$$p_{T,l} > 30 \text{ GeV}, \quad |y_l| < 2.5,$$

$$\Delta R_{j,l} > 0.4, \quad \Delta R_{l,\gamma} > 0.8.$$

To remove the contribution from an off-shell photon, $\gamma^* \rightarrow l^+l^-$, we introduce the following cut,

$$m_{l+l^-} > 15 \text{ GeV},$$

and to enhance the quartic gauge coupling sensitivity, we suppress the $Z \rightarrow l^+l^-\gamma$, and $W \rightarrow l\nu_l\gamma$ contributions applying the following cuts:

$$m_{l+l^-\gamma} > 120 \text{ GeV},$$

$$m_{l\nu\gamma}^T > 90 \text{ GeV}.$$

Finally, to take into account the vector boson masses, we define a modified transverse scalar sum

$$H_T^{V\gamma} = \sum_{i \in \text{partons}} p_{T,i} + p_{T,\gamma} + E_{T,V},$$

where $E_{T,V} = \sqrt{m_V^2 + p_{T,V}^2}$, and m_V is the reconstructed vector boson mass.

In Table. 3.9, one can observe that the $pp \rightarrow \gamma\gamma jj$ has a smaller EW cross-section compared to the QCD one. The $Z\gamma jj$ and $W^+\gamma jj$ have even larger cross-sections for the EW channel with the VBS cuts. Despite this, the $pp \rightarrow \gamma\gamma jj$ has a greater significance due to the larger EW total cross-section.

3.4.3 Differential distributions

We start looking at the distributions which are affected by the VBS cuts. The invariant mass of the two tagging jets is shown in Fig. 3.20. The impact of the QCD corrections on the EW channel is modest, with K_{EW} ¹ ranging between 0.97 and 1.03 between $m_{j_1j_2} \in [900, 3000] \text{ GeV}$, but the reduction on the scale variation uncertainty is clearly visible. The QCD channel receives a larger correction with K_{QCD} between 1.8 and 2.0 in the same range. Also, the scale variation uncertainty of the QCD channel is larger. The QCD channel has a larger variation in $m_{j_1j_2}$, it starts with a bigger cross-section than the EW channel, but this changes around $m_{j_1j_2} \approx 1500 \text{ GeV}$. This tendency explains why the $m_{j_1j_2}^{cut}$ had that much impact on the significance of the process.

¹The K-factors are defined as $K = \sigma_{NLO}/\sigma_{LO}$ where the σ_{NLO} is the cross-section at NLO in α_s . The EW and QCD subscripts indicate the channel of the K-factor, **not** the type of the correction.

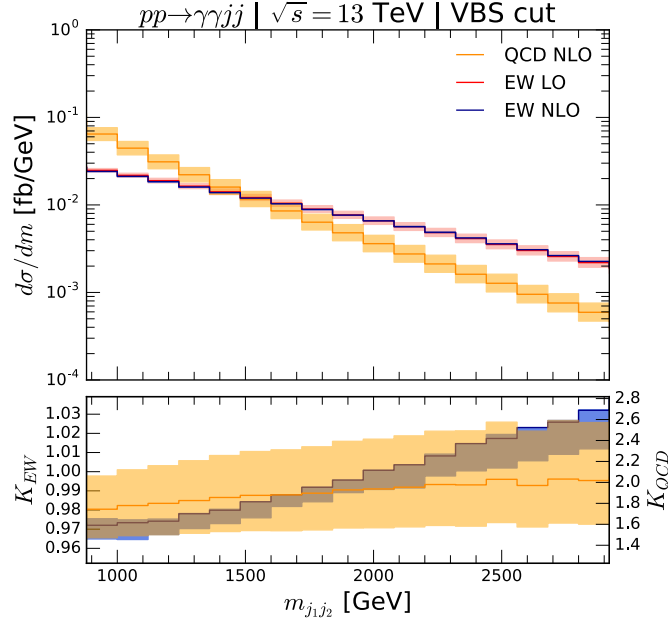


Figure 3.20: Invariant mass of the two tagging jets. The jets are numbered by their p_T , the jet with highest p_T is j_1 .

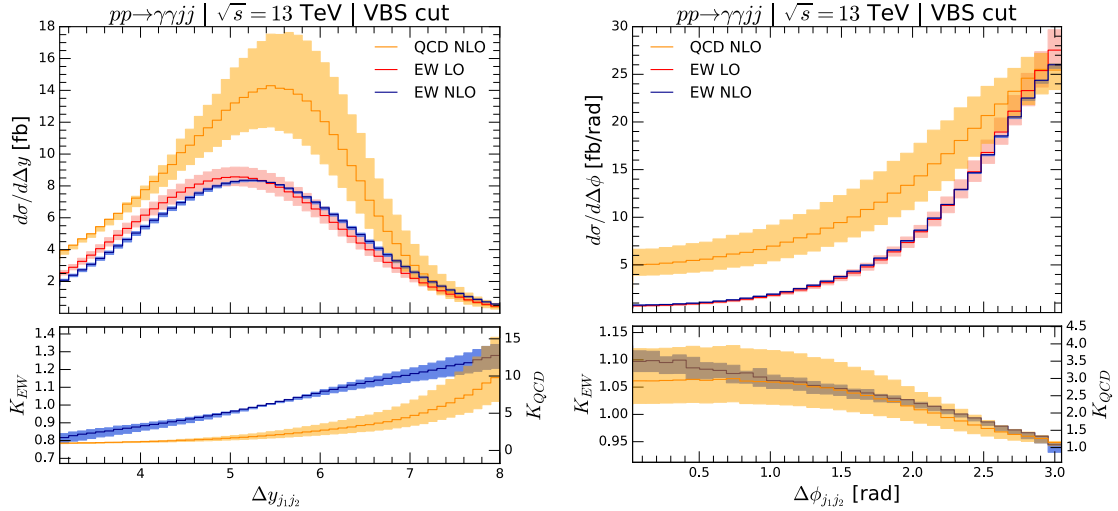


Figure 3.21: Angular separations between the two tagging jets. Rapidity separation (left). Azimuthal angle separation (right).

In the rapidity separation between the two tagging jets, Fig. 3.21, we can see that both, the QCD and the EW channels, prefer high rapidity separations, with a peak around $\Delta y_{j_1 j_2} \approx 5.5$, but the QCD channel has a bit more separated jets, peaking at $\Delta y_{j_1 j_2} \approx 5.8$. The NLO QCD corrections to the EW channel pushes both jets apart in the rapidity coordinate. Moreover, the K_{EW} in this case is bigger than in the $m_{j_1 j_2}$, specially in the high rapidity separation region. The reason for this is probably due to the new emission opening higher rapidity regions. It explains the small change in rapidity separation and the

higher K -factor and scale uncertainty, due to this region being mainly the real contribution which is calculated only at LO. Note that, the differential cross-section of the QCD channel is higher than the EW one in the full range which explains why this cut did not have almost any impact on the significance.

The separation of the jets in the ϕ -coordinate, Fig. 3.21, shows that the tagging jets appear mainly back-to-back. Both distributions peak at $\Delta\phi_{j_1 j_2} \approx \pi$, but the QCD has a smoother distribution.

The position of the photons relative to the jets is studied through the observable z^* defined as

$$z_X^* = \frac{y_X - (y_{j_1} + y_{j_2})/2}{y_{j_1} - y_{j_2}}.$$

Note that for $y_X = y_{j_1}$, one obtains

$$z_{j_1}^* = \frac{y_{j_1} - (y_{j_1} + y_{j_2})/2}{y_{j_1} - y_{j_2}} = \frac{(y_{j_1} - y_{j_2})/2}{y_{j_1} - y_{j_2}} = \frac{1}{2},$$

and when $y_X = y_{j_2}$, $z_{j_2}^* = -1/2$. So, this observable gives us a normalized rapidity distance between the particle X and one of the jets, so that when X has the same rapidity of one of the jets the value of z^* is $1/2$ or $-1/2$.

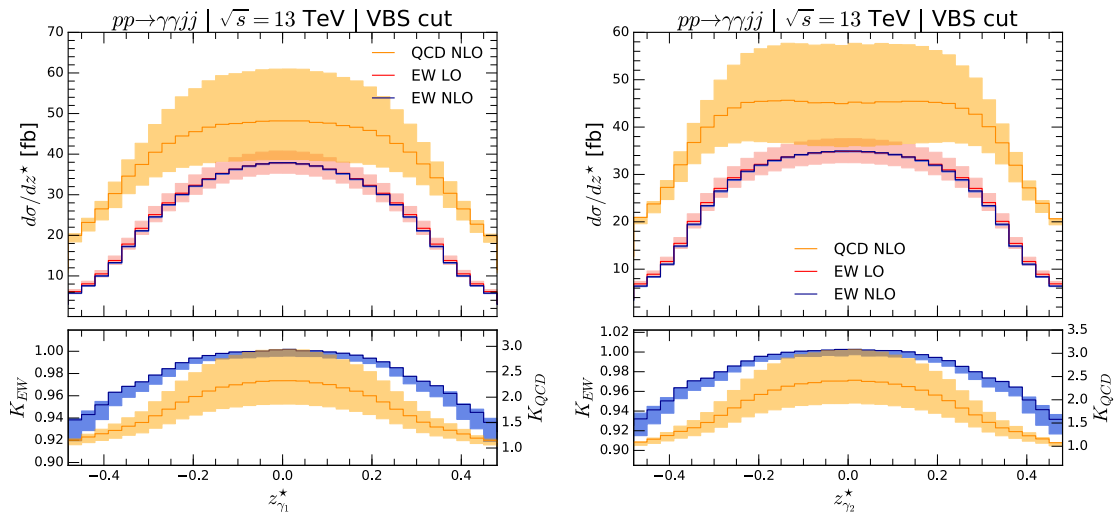


Figure 3.22: Relative position of the photons respect to the jets using z^* . The z^* for the photon with highest p_T (left), and for the photon with lowest p_T (right).

Fig. 3.22 shows the distribution for both photons, which are produced between the two jets with small rapidity separations. The two jets are produced close to the beam direction, with high rapidities, while the photons will be found at the center part of the detector. Furthermore, the QCD channel cross-section is larger than the EW one in the full range. The NLO QCD corrections are negligible for the EW channel in this distribution, and are only significant when the photons are close to the jets, while for the QCD channel, they produce large correction in the central region, note the different scales for K_{EW} and K_{QCD} .

The rapidity and azimuthal angle separation between the photons, Fig. 3.23, shows that both processes prefer photons with close rapidities, which is consistent with what we found in the z^* observable in Fig. 3.22. The QCD channel has a higher peak for small

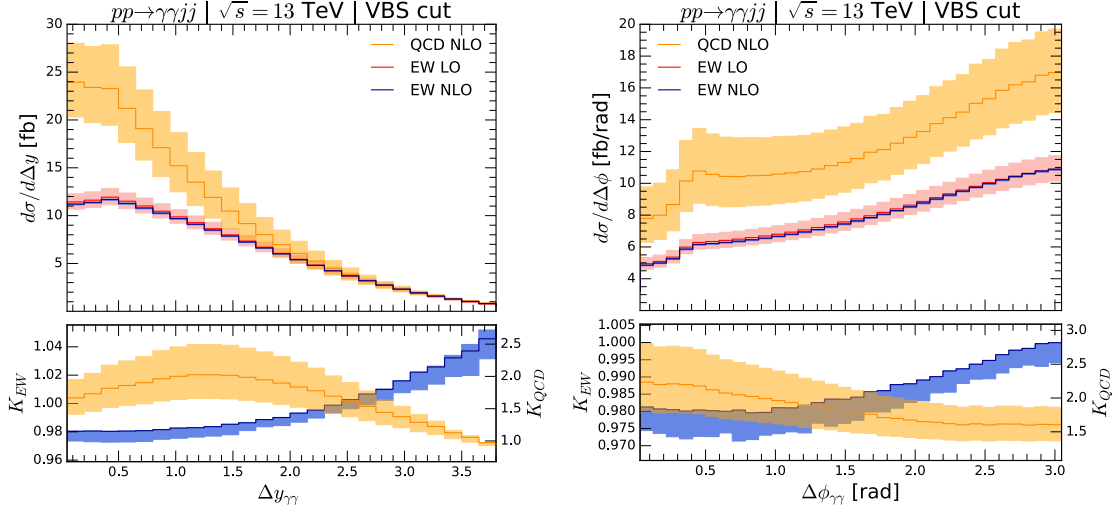


Figure 3.23: Angular distributions between the two photons. Rapidity separation (left), azimuthal angle separation (right).

rapidity separations but falls faster, it reaches the EW distribution when $\Delta y_{\gamma\gamma} \approx 2$. In the ϕ -separation, both distributions have similar shapes, with a higher value of the cross-section for the QCD channel in all the range. The distribution is also smoother in this case, with a small preference for back-to-back photons. For the K -factors, they are consistently higher for the QCD channel.

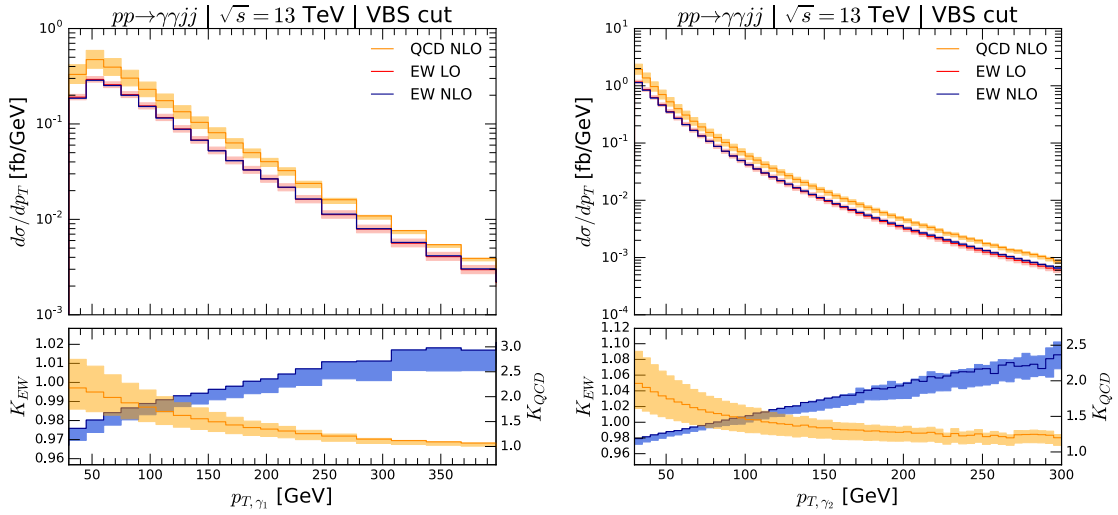


Figure 3.24: p_T distribution for both photons. The hardest photon (left), the softest photon (right).

The $p_{T,\gamma}$ distributions are almost identical for the two channels but the QCD channel is higher in the whole spectrum. For the hardest photon, γ_1 , the distribution peaks around $p_{T,\gamma_1} \approx 55$ GeV. Then there is an exponential decay from $p_{T,\gamma_1} \approx 55$ GeV to $p_{T,\gamma_1} \approx 400$ GeV that can be seen as a line in the logarithmic plot. The K -factor again shows a larger correction for the QCD channel, that is higher in the high p_T region, while the

EW channel has smaller corrections with a K -factor $\in [1.00, 0.97]$ for $p_{T,\gamma_1} \in [45, 400]$ GeV. For the softest photon, the distribution peak cannot be seen, and the distribution has a decay that is less than exponential. The K -factor for the EW channel grows linearly for $p_{T,\gamma_2} \in [45, 300]$ GeV, while for the QCD channel most of the change of the QCD correction is in the low p_{T,γ_2} region.

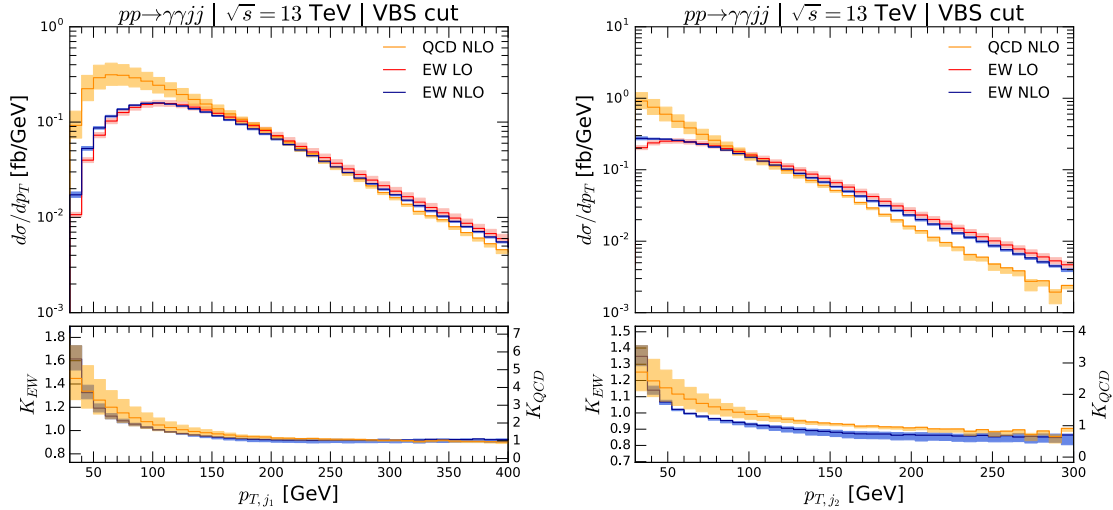


Figure 3.25: p_T distribution for both tagging jets. The hardest jet (left), the second-hardest jet (right).

Fig. 3.25 shows that the QCD channel prefers jets with smaller p_T compared to the EW channel. For the hardest jet, the distribution peaks at $p_{T,j_1} \approx 60$ GeV in the QCD channel, while it peaks around $p_{T,j_1} \approx 110$ GeV in the EW channel, with the p_T in the QCD channels falling faster than in the EW channel. The NLO QCD corrections for both processes are higher in the low p_{T,j_1} region, where the K -factors blow up, which is due to the new jet in the NLO QCD correction opening the small p_T regions. At LO, this small p_T regions are highly constrained due to momentum conservation. The distribution for j_2 is similar but with the expected shift to lower p_T . Also, the introduction of a new jet allows for higher cross-section in the lower p_T regions.

Finally, in Fig. 3.26 the azimuthal angle separation between the hardest photon and softest tagging jet, $\Delta\phi_{j_2\gamma_1}$, is presented. There, a large deviation between the QCD channel and the EW channel can be seen at NLO for large $\Delta\phi_{j_2\gamma_1}$ values. At $\Delta\phi_{j_2\gamma_1} \approx \pi$, large K -factors appear, $K_{QCD} \approx 4$ and $K_{EW} \approx 1.6$, since this region is dominated by three jet events, whose contribution is calculated at LO, making it sensitive to further QCD emissions taken into account in higher-order corrections or parton shower matched calculations. This also explains the large scale uncertainties in this region. The combination of the large difference between the QCD- and EW-channel cross-sections and K -factors, motivates the introduction of a $\Delta\phi_{j_2\gamma_1}$ cut that controls the problematic region.

In Fig. 3.27, the impact of the $\Delta\phi_{j_2\gamma_1}^{cut}$ on the significance is studied. The optimal value of the significance is given by $\Delta\phi_{j_2\gamma_1}^{cut} = 2.5$, which means that only events with $\Delta\phi_{j_2\gamma_1} \leq 2.5$ are considered. Nevertheless, for the range of invariant jet masses $m_{j_1j_2}^{cut} \in [800, 2000]$ GeV the sensitivity of the significance on the $\Delta\phi_{j_2\gamma_1}^{cut}$ is small and values of $S > 4$ can be seen for any value of $\Delta\phi_{j_2\gamma_1}^{cut} > 2$. On the other hand, the $\Delta\phi_{j_2\gamma_1}^{cut}$ not only slightly improves the significance, it also removes a region of phase space dominated by three jet events, affected by large uncertainties due to being effectively calculated at LO, which improves

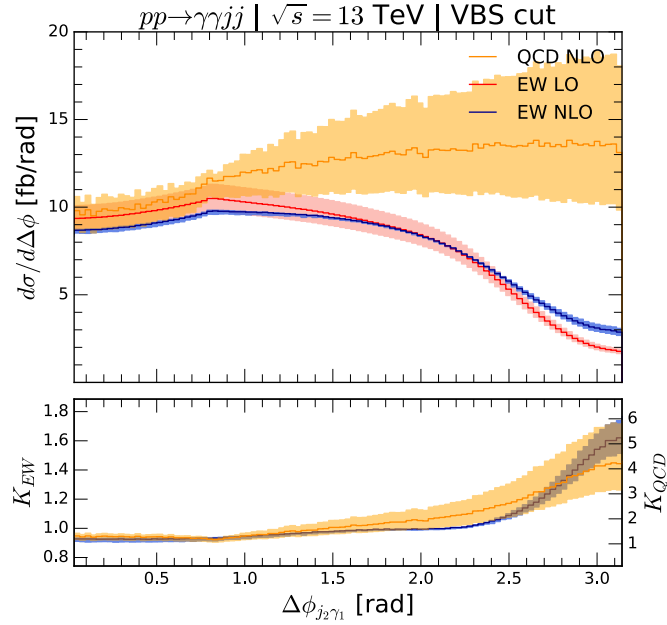


Figure 3.26: Differential cross-section as a function of the azimuthal angle between the second-hardest jet and the hardest photon. This observable shows a large difference between the QCD- and EW-channel for large values of $\Delta\phi_{j_2\gamma_1}$. Moreover, this region also shows large K-factors and large scale uncertainties.

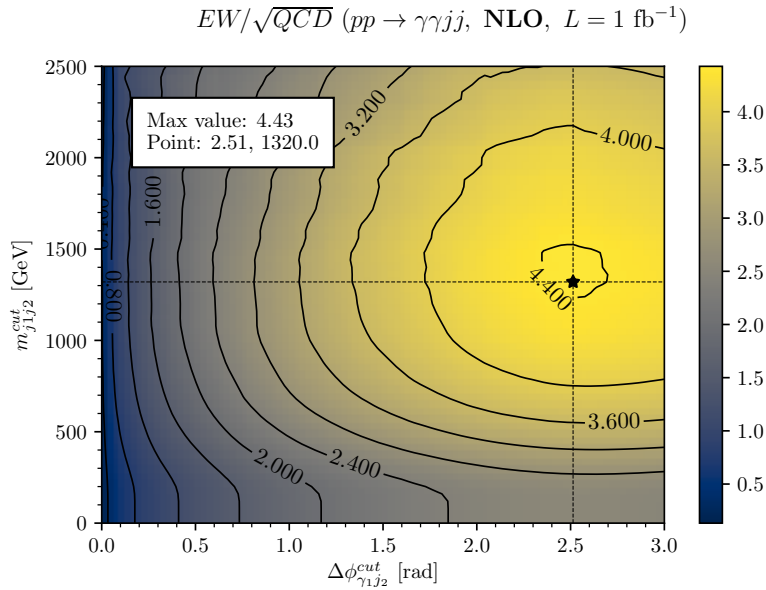


Figure 3.27: Significance, EW/\sqrt{QCD} , for the invariant mass jet cut and the proposed cut, $\Delta\phi_{j_2\gamma_1}$.

the accuracy of the prediction.

3.4.4 Anomalous couplings

As an example of the possible effects of anomalous couplings on differential distributions, in Fig. 3.28 we show the differential distributions of the invariant mass of the di-photon system for the operator $L_{T,8}$ and compare it against the SM predictions. We chose this operator because it involves the interaction between four neutral bosons, and it is absent in the SM. In Fig. 3.28 we see that the effect of the operator is mainly modifying the

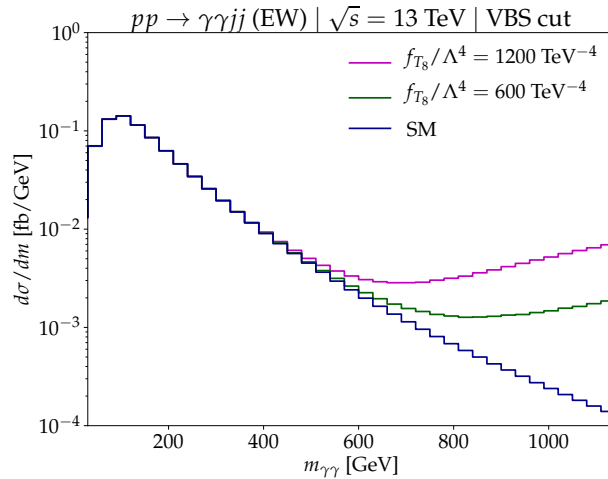


Figure 3.28: Invariant mass of the two photons for two different values of the Wilson coefficient $f_{T,8}/\Lambda^4$ compared to the SM result.

high invariant mass region while the values of the cross-section for small invariant mass $m_{\gamma\gamma} \lesssim 400$ GeV are given by the SM ones. We see hints of the unitarity violation due to the non-renormalizable operator and the lack of form factor. A more comprehensive study on AC effects will involve multi-dimensional analysis including all operators participating in this process, and it is left for future work.

Chapter 4

Parton Shower in Di-boson and Tri-boson processes

4.1 Introduction

Processes with final-state particles coming from two or three electroweak vector bosons are known as **di-boson and tri-boson production processes**, respectively. Each of the vector bosons can decay leptonically or hadronically. As mentioned in Sec. 3.4 the specific tri-boson process where one of the vector bosons decay hadronically and the other two leptonically is an s-channel contribution to the corresponding VBS process.

Throughout run 1 and 2 of the LHC, the measurement of di-boson production processes has been a major focus. They give access to TGC, see Fig. 4.1 fixed in the SM by the non-Abelian gauge symmetry $SU(2)_L \times U(1)_Y$, and contribute to the Higgs background, whose couplings measurement have been a priority in run 1 and 2. Di-boson production processes have been measured by ATLAS, see [98–114], and CMS, see [115–124]. A comparison of the measurement results with the best theoretical predictions using the SM is shown in Fig. 4.2.

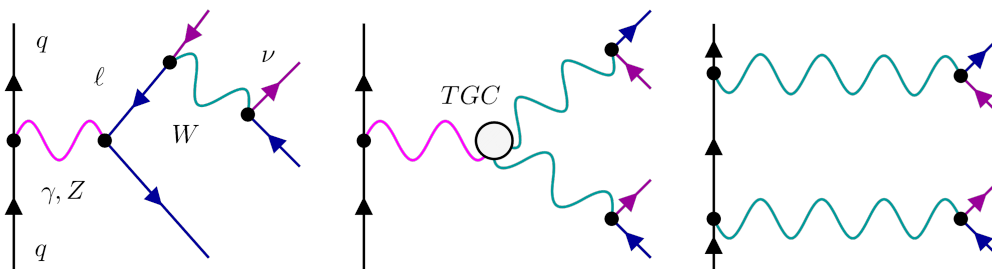


Figure 4.1: Representative diagrams contributing to the $pp \rightarrow l^+ \nu l^- \bar{\nu}$ process at LO. The only QCD component in the process is the initial-state quark line. The middle figure shows that the process gives access to TGC.

Tri-boson production processes are also of great importance to test the EW parameters and study the Higgs sector, giving access to TGC and QGC, see Fig. 4.3. Recently, the CMS collaborations has detected for the first time tri-boson production processes with three massive vector bosons, see [125], this adds to the previous efforts of ATLAS and CMS, see [126–128], and to the tri-boson production processes with at least one on-shell photon that had been already measured, see [129]. As more statistics is collected, tri-boson

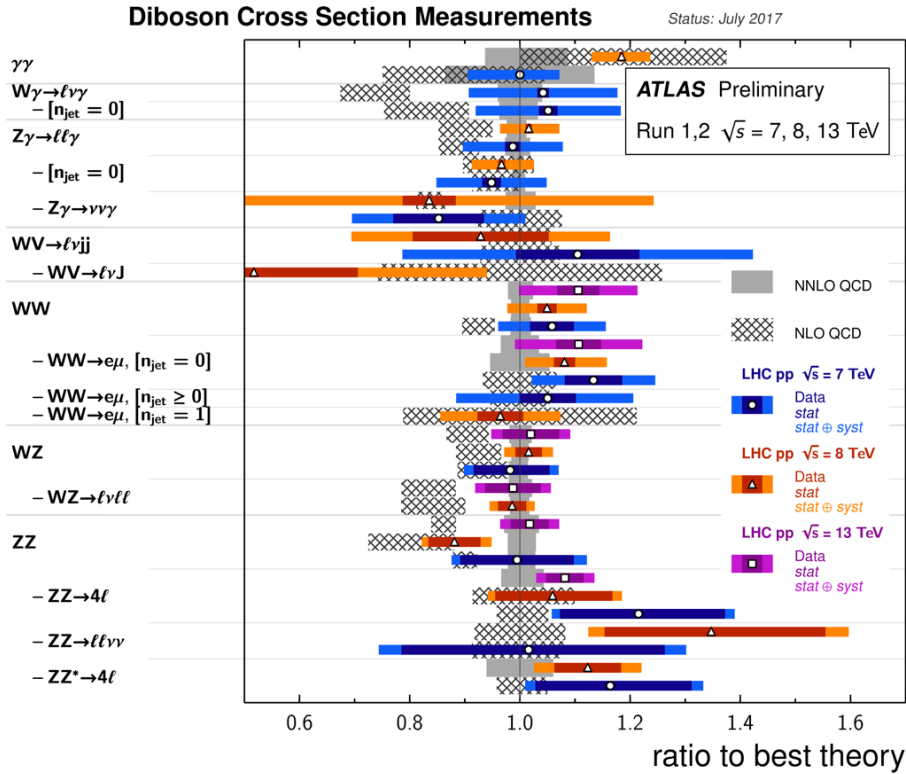


Figure 4.2: Ratio between the di-boson cross-section measurements during runs 1 and 2 of the LHC and the best theoretical predictions.

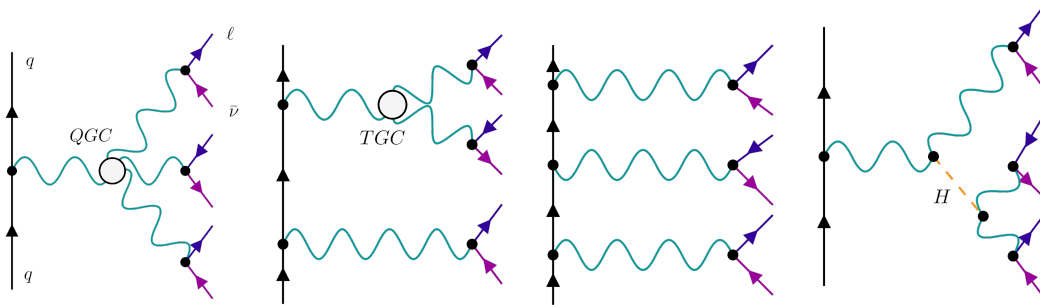


Figure 4.3: Representative diagrams contributing to the $pp \rightarrow l^+ \bar{\nu} l^- \nu^+ \bar{\nu}$ process at LO. The only QCD component in the diagrams is the initial-state quark line, which can have one, two or three vector bosons attached. The TGC and QGC are highlighted in the diagrams.

processes are going to become more important to determine the EW parameters and to search for small deviations in QGC, which require precision calculations at least of NLO QCD.

We are going to discuss di-boson and tri-boson production process with a fully leptonic final-state. All di-boson [83,130] and tri-boson [131–136] processes have been implemented in VBFNLO at NLO QCD, including also the off-shell diagrams and all spin-correlations, with the possibility of using anomalous couplings to parametrize BSM effects in an EFT approach. As can be seen from Fig. 4.1 and Fig. 4.3, the only QCD component in the diagrams is the initial-state quark line, which can have one, two or three vector bosons

attached to it. This allows us to implement the NLO QCD corrections in a manner analogous to the explanation in Sec. 3.2. The dipoles are the same we found in Sec. 3.2.2, and the boxed and pentagons are calculated with calls to the boxline and penline subroutines, see 54.

On the other hand, as discussed in section 2.3, any full calculation that has to be compared to experiment will require to properly treat the high final-state multiplicity due to the QCD radiation. This is taken into account with parton showers, Sec. 2.3.8, adding QCD emissions to fixed-order processes, which is accomplished via **Monte Carlo event generators** like Herwig [137, 138], Pythia [139, 140] or Sherpa [141], called from now on only MC for brevity. The state-of-the-art prediction for tri-boson production processes involve the Matching of NLO QCD fixed-order calculations with parton showers. Event generators are usually able to calculate themselves some LO amplitudes, but today standard requires the splitting of tasks between the MC, which performs the parton shower, and NLO amplitude providers, also called **One-loop providers** (OLP), which supply the MC with the appropriate amplitude.

In the early days of MC and OLP, the communication between the programs was internal and different for each program. In order to standardize how this communication should be established, a convention was created in the Les Houches workshop in 2010, **Binoth Les Houches Accord** (BLHA), with an update in the same workshop in 2013 (BLHA2).

In this chapter, we are going to implement an interface following the Les Houches Accord for the di-boson and tri-boson production processes between the MC Herwig and the OLP VBFNLO. It will allow us to make calculations at NLO QCD precision and include parton shower effects, multi-particle interactions and hadronization, providing us with observables that can be directly compared with experiment, after including the detector effects. Moreover, we can make use of the anomalous couplings implemented in VBFNLO to study BSM physics systematically.

In section 4.2 we will explain the implementation of the interface in detail. Explaining the different conventions used and clearly indicating the extra features that are not in the BLHA standard. The explanation of the implementation will be separated in different subsections, each corresponding to a different step in the evaluation of the program.

In section 4.3 we will expose the different checks done to ensure the correct implementation of the interface. The interface has been implemented for all di-boson and tri-boson processes with fully leptonic final-state.

Finally, section 4.4 will contain a phenomenological study of parton shower effects. First, we will start with an analysis of the scale variations, including the parton shower hard scale, of two different processes: $pp \rightarrow e^+ \nu_e \mu^- \bar{\nu}_\mu \tau^+ \nu_\tau + X$ and $pp \rightarrow e^- \bar{\nu}_e \mu^+ \nu_\mu \gamma + X$. Then, we will study the cross-section changes due to migration effects. The different cuts can be set at the generator or analysis level, both having its advantages and inconveniences. Parton showers modify the kinematics of the process allowing an accepted event, that has passed the generation cuts, to be thrown by the analysis which changes the total cross-section and the differential distributions. In particular, we will study the migration effects due to the Frixione isolation cut on the photon in the $pp \rightarrow e^- \bar{\nu}_e \mu^+ \nu_\mu \gamma + X$ production process.

4.2 Interface Implementation

The interface works in three different phases. In the first phase, an order file is created by the MC and read by the OLP to check if it can provide the required amplitudes. In the second phase, the parameters for the run are initialized, and in the case that an active

interchange of a parameter is needed, a communication is set between the MC and OLP. In the third phase, the MC passes the kinematics to the OLP, and after the calculation of the phase space point, the OLP returns an array containing the Laurent coefficients of the virtual contribution, A_2, A_1, A_0 ; and the Born amplitude squared, $|\mathcal{M}_B|^2$, where the conventions are shown in Eq. (4.1), and Eq. (4.2).

$$\mathcal{I}(\{k_j\}, R.S, \mu_R^2, \alpha_s(\mu_R), \alpha, \dots) = C(\epsilon) \left(\frac{A_2}{\epsilon^2} + \frac{A_1}{\epsilon} + A_0 \right), \quad (4.1)$$

$$C(\epsilon) = \frac{(4\pi)^\epsilon}{\Gamma(1-\epsilon)} \left(\frac{\mu^2}{\mu_R^2} \right)^\epsilon. \quad (4.2)$$

In VBFNLO, the implementation of the interface is through the functions defined in `VBFNLO/utilities/BLHAInterface.cpp`. They can be classified depending on the phase of the calculation they are involved. But first, for clarity, we assort all the functions depending on where they were originally proposed.

```
void OLP_Order(char* inname, char* outname, int* ierr)
```

`OLP_Order` is an extra function, that takes care of the order-contract file management. The following two functions were originally proposed in Ref. [142],

```
void OLP_Start(char* fname, int* ierr)
void OLP_EvalSubProcess(int i, double* pp, double mu, double* alphas, double*
    rval)
```

while the following ones were proposed in the update of Ref. [143].

```
void OLP_Info(char olp_name[15], char olp_version[15], char message[255])
void OLP_SetParameter(char* line, double* re, double* im, int* ierr)
void OLP_EvalSubProcess2(int* i, double* pp, double* mu, double* rval, double*
    acc)
void OLP_Polvec(double* p, double* q, double* eps)
```

There are also two functions that are not part of the BLHA:

```
void OLP_PhaseSpacePoint(int* proc, double* rpsnum, double* r, double* p,
    double* weight)
void OLP_GetParameter(char* line, double* re, double* im, int* ierr)
```

`OLP_PhaseSpacePoint` and `OLP_GetParameter` allow to use the OLP phase space generator instead the MC's one. All these functions are wrappers for FORTRAN subroutines inside `VBFNLO/utilities/BLHAHelper.F90` that do the main part of the calculation.

In the following, a detailed explanation of each function is given following the different phases of the process in chronological order, Fig. 4.4.

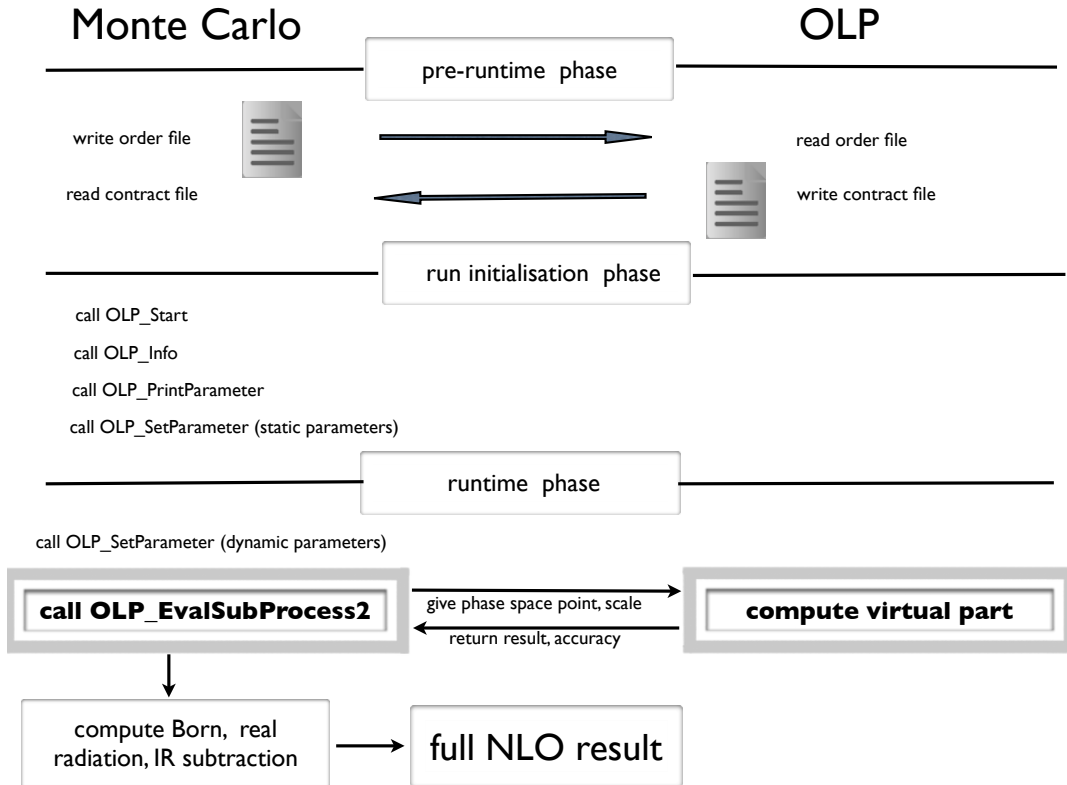


Figure 4.4: A flowchart illustrating how the interface operates, Ref. [143].

4.2.1 Pre-runtime phase

In the pre-runtime phase, the MC generator creates an order file, like the one shown in Fig. 4.5, where two different types of keywords with different values can be seen. The first kind are the **required keywords**: `InterfaceVersion`, `Model`, `CorrectionType`, `IRregularisation`, `AlphasPower`, and `AlphaPower`; while the second kind are **optional keywords**: `HelAvgInitial`, `ColAvgInitial`, `MCSymmetrizeFinal`, and `AmplitudeType`.

- `InterfaceVersion` is needed because the update of the interface is not backwards compatible. Hence, this keyword can have two values, `BLHA` or `BLHA2`, depending on whether the standard or updated interface has to be used.
- `Model` is the physical model in which the calculation is taking place, i.e. `SM`, `MSSM`.
- `CorrectionType` tells the OLP which kind of NLO correction we are asking for, i.e. `QCD`, `EW`.
- `IRregularisation` sets the IR regularization scheme that the OLP should use, i.e. `Conventional Dimensional Regularization`, `CDR`; `Dimensional Reduction`, `DREG`.
- `AlphasPower` and `AlphaPower` are the powers of α_s and α respectively, for the particular subprocess the MC is asking for.

The OLP will read this file using a call to the following function

```
void OLP_Order(char* inname, char* outname, int* ierr)
```

where `iname` is a pointer to the order file name, `outname` is a pointer to the contract file name, and `ierr` is an integer pointer with value +1 if the OLP could sign the contract and any other number otherwise. The contract file will be a copy of the order file where the OLP will have appended `| OK` after a line if it can provide that particular item, or `| Error` if it can not provide it. An example of the contract signed by VBFNLO for the process $d\bar{d} \rightarrow \gamma\gamma$ can be seen in Fig. 4.6.

In the contract file, we can also see lines defining a particular subprocess the MC is asking for, i.e. `1 -1 → 22 22 22`. In this case, the OLP, instead of writing `| OK` or `| Error`, writes two numbers separated by a space. The first number is the quantity of subprocesses of that particular process, and the second number is a label the OLP assigns to that particular subprocess. In case there were more than one subprocess, the OLP will write the numbers as a list separated by spaces.

4.2.2 Initialization phase

The initialization phase starts with a call to the `OLP_Start` wrapper, that initializes VBFNLO, and prepares it to start the run.

```
void OLP_Start(char* fname, int* ierr)
```

A couple of issues appears in this part. VBFNLO uses process identifiers instead of PDG numbers to select the process, which means, that setting up the process, VBFNLO has also to translate between the PDG numbers, and the internal process identifier. Another difficulty is that VBFNLO calculates all crossings in each call, using crossing relations, while in the contract file these are different subprocesses. Hence, we have to find the correct momentum mappings and crossing signs to relate the particular subprocess to the appropriate call inside VBFNLO. This is carried out during the pre-runtime phase by a call inside `OLP_Start` to

```
SUBROUTINE VBFNLO_SetupProcess(nparticles, pdgprocess, orderAlphas, orderAlpha,
    amptype, procok)
```

where, depending on the values of α_S and α , a helper subroutine will be called inside `VBFNLO/utilities/BLHAMommmapping.F90` that will find the process identifier from the number of reconstructed external vector bosons and partons in the process, and the correct momentum mapping for the crossings.

The `OLP_Info` keeps track OLP's information: version, and papers for proper citation.

```
void OLP_Info(char olp_name[15], char olp_version[15], char message[255])
```

In the first proposed interface, Ref. 142, there was not a standardized way to pass parameters. These should be sorted out between the particular MC and OLP. In the update, Ref. 143, a new way to pass parameters was proposed. It involves a call to

```
void OLP_SetParameter(char* line, double* re, double* im, int* ierr)
```

```

# OLP order file created by Herwig/Matchbox

InterfaceVersion      BLHA2

Model                 SM
CorrectionType        QCD
IRregularisation      CDR
Extra HelAvgInitial   no
Extra ColAvgInitial   no
Extra MCSymmetrizeFinal no

AlphasPower           0
AlphaPower            3
AmplitudeType         tree
1 -1 -> 22 22 22
-1 1 -> 22 22 22
AmplitudeType         loop
1 -1 -> 22 22 22
AmplitudeType         cctree
1 -1 -> 22 22 22
AmplitudeType         loop
-1 1 -> 22 22 22
AmplitudeType         cctree
-1 1 -> 22 22 22
AlphasPower           1
AmplitudeType         tree
1 -1 -> 21 22 22 22
1 21 -> 1 22 22 22
-1 1 -> 21 22 22 22
-1 21 -> -1 22 22 22
21 1 -> 1 22 22 22
21 -1 -> -1 22 22 22

```

Figure 4.5: Example of an order card created by Herwig for the process $d\bar{d} \rightarrow \gamma\gamma\gamma$.


```

# OLP order file created by Herwig/Matchbox

InterfaceVersion          BLHA2 | OK

Model                     SM | OK
CorrectionType            QCD | OK
IRregularisation         CDR | OK
Extra HelAvgInitial      no | OK
Extra ColAvgInitial      no | OK
Extra MCSymmetrizeFinal  no | OK

AlphasPower              0 | OK
AlphaPower               3 | OK
AmplitudeType            tree | OK
1 -1 -> 22 22 22 | 1 1
-1 1 -> 22 22 22 | 1 2
AmplitudeType            loop | OK
1 -1 -> 22 22 22 | 1 3
AmplitudeType            cctree | OK
1 -1 -> 22 22 22 | 1 4
AmplitudeType            loop | OK
-1 1 -> 22 22 22 | 1 5
AmplitudeType            cctree | OK
-1 1 -> 22 22 22 | 1 6
AlphasPower              1 | OK
AmplitudeType            tree | OK
1 -1 -> 21 22 22 22 | 1 7
1 21 -> 1 22 22 22 | 1 8
-1 1 -> 21 22 22 22 | 1 9
-1 21 -> -1 22 22 22 | 1 10
21 1 -> 1 22 22 22 | 1 11
21 -1 -> -1 22 22 22 | 1 12

```

Figure 4.6: Example of a contract card signed by VBFNLO from the order card created by Herwig for the process $d\bar{d} \rightarrow \gamma\gamma\gamma$.

where `line` is a string pointer to the name of the parameter; `re` and `im` are the real and imaginary part of the parameter, we set `im` to zero if the parameter is real; and `ierr` is a pointer to an integer, that will have value 1 if the parameter could be set successfully by the OLP, or any other integer if not.

4.2.3 Runtime phase

After the contract file is signed by the OLP, and the parameters are set, the runtime phase starts. If we are using the standard BLHA, not the updated version, it basically involves the call to the function

```
void OLP_EvalSubProcess(int i, double* pp, double mu, double* alphas, double*
    rval)
```

where `i` is the number assigned to the subprocess in the contract file; `pp` is an array with the kinematic information; `mu` is the scale, μ ; `alphas` is a pointer to the value of the strong coupling evaluated at the scale μ , $\alpha_s(\mu)$; and `rval` is a pointer to an array including the three Laurent coefficients and the Born matrix element square as $\{A_0, A_1, A_2, |\mathcal{M}_B|^2\}$.

In the updated version, the function call reads

```
void OLP_EvalSubProcess2(int* i, double* pp, double* mu, double* rval, double*
    acc)
```

There are a couple of changes: First, $\alpha_s(\mu)$ is no longer passed through this function call, instead it is passed through the `OLP_SetParameter` explained in the initialization phase. Second, there is a new pointer to an estimation of the accuracy of the calculation, if the OLP can provide it, or zero if it passed the internal stability test of the OLP, and it can not provide an accuracy estimation. In case, the point failed the stability test it will be set to a very large value.

The standard amplitude returned by the OLP is color and helicity summed, but in some cases, the MC can ask for color-correlated, or spin-correlated amplitudes through the optional keyword `AmplitudeType`, which will be set to `cctree`, or `scctree`, respectively. The standard value of `AmplitudeType` is `loop`. Other flags can also be passed, for example, `AmplitudeType tree` will make `EvalSubProcess2` to pass only the Born squared amplitude. When the MC ask for a color/spin-correlated amplitude, this is no more a number, but a vector in color-helicity space. So, in this case, it is important to have a convention for the order in which the matrix elements are passed.

Color-correlated amplitudes

If we write the amplitude as a vector in color-helicity space, $|\mathcal{M}\rangle$. Then, the color-correlated amplitude is given by

$$C_{ij} = \langle \mathcal{M} | \mathbf{T}_i \cdot \mathbf{T}_j | \mathcal{M} \rangle, \quad (4.3)$$

where \mathbf{T}_i are the generators of $SU(3)$; in the fundamental representation if i is a quark, and in the adjoint representation if i is a gluon.

To have complete information of the matrix Eq. (4.3), we need

$$\frac{n(n-1)}{2},$$

numbers, where n is the number of particles in the corresponding process. Consequently, the `rval` returned by `OLP_EvalSubProcess2` will be an array of length $n(n-1)/2$, starting at index 0, and having element C_{ij} , at position $i+j(j-1)/2$ for $i < j$.

Spin-correlated amplitude

The spin-correlated amplitude is given by

$$S_{ij} = \langle \mathcal{M}_{i,+} | \mathbf{T}_i \cdot \mathbf{T}_j | \mathcal{M}_{i,-} \rangle,$$

where i, \pm indicates the value of the helicity of the gluon at position i , and j is any other colored particle in the process. In this case, the matrix is a complex matrix that is not symmetric, which means that a total of $2n^2$ real parameters should be passed between the OLP and the MC. The convention is that the OLP passes an array starting at zero index, with $\text{Re}(S_{ij})$ at position $2i + 2nj$, and $\text{Im}(S_{ij})$ at position $2i + 2nj + 1$. Moreover, the MC needs to know the polarization vector used by the OLP, which will be passed through a call to

```
void OLP_Polvec(double* p, double* q, double* eps)
```

where `p` is a pointer to the gluon momentum, `q` is a pointer to the reference momentum, and `eps` is the polarization vector as

$$\epsilon_{\pm}^{\mu}(p, q) = \pm \frac{1}{\sqrt{2}} \frac{\langle q^{\mp} | \gamma^{\mu} | p^{\pm} \rangle}{\langle q^{\mp} | p^{\pm} \rangle},$$

which is transferred as an array where real and imaginary part alternate.

OLP phase space

The standard interface is designed such that the MC manages the computation and the OLP only gives the amplitudes the MC ask for. But in the case between Herwig and VBFNLO, an extension of the interface have been done, such that the phase space used can be specified by VBFNLO instead. The momenta are given to the OLP through a call to the following function

```
void OLP_PhaseSpacePoint(int* proc, double* rpsnum, double* r, double* p,
double* weight)
```

where `proc` is the number of the process, `rpsnum` is a random number used by VBFNLO to select the phase space, `r` is an array of random numbers to generate the kinematics, `p` are the momenta generated by VBFNLO, and `weight` is the corresponding weight of the phase space point generated by VBFNLO.

Using the OLP phase space generator has the problem that the MC now has no access to certain information, i.e. the phase space dimension of the generated point. To solve this problem, the extra function

```
void OLP_GetParameter(char* line, double* re, double* im, int* ierr)
```

is created. It works similarly to `OLP_SetParameter`, but this time it allows the MC to get the parameters from the OLP.

4.3 Checks

In this section, the checks done to ensure the correct implementation of the interface are presented.

Di-boson

A comparison between Herwig interfaced with VBFNLO as an OLP and Herwig interfaced with MadGraph [144] as an OLP, without parton shower, hadronization or multi-particle interactions, was performed. Comparing against an external OLP, like MadGraph, is a stronger test than necessary because the correct implementation of the di-boson processes in VBFNLO was already tested in Refs. [83, 130].

The following cuts were used for the final-state photons and leptons:

$$\begin{aligned} p_{T,\ell} &\geq 20 \text{ GeV}, & -2.5 \leq y_\ell \leq 2.5; \\ p_{T,\gamma} &\geq 20 \text{ GeV}, & -2.5 \leq y_\gamma \leq 2.5; \\ \Delta R_{\ell\gamma} &\geq 0.5, & m_{\ell\ell} \geq 15 \text{ GeV}. \end{aligned}$$

To remove the photon fragmentation component, the Frixione Isolation Cut was used with the following parameters:

$$\delta_0 = 0.7, \quad \epsilon = 1.$$

Furthermore, the tests were done using only two flavors and a unit CKM matrix. Since we are considering massless quarks in the calculation of the matrix elements, two flavors are enough to test the correctness of the implementation.

As explained in Sec. 2.3.4 the NLO contribution divides into three components; the Born, the Reals and the Virtual contributions. This separation is arbitrary because contributions can be moved between the Reals and the Virtuals, only their sum is physical and independent of the conventions used. The Herwig interface for VBFNLO and MadGraph uses the same conventions, so we can compare each component separately. The results can be seen in Table. 4.1 where we can see an agreement at the 0.5% for all the components.

Tri-boson

After the tests performed in the di-boson case, which includes a cross-check against an independent OLP for the different components, the cross-check for tri-boson production processes can be simplified since the di-boson and tri-boson production modes inside VBFNLO, and at the level of the interface, have the same structure (QCD is blind to the number of EW particles attached to the quark line). Moreover, the implementation of these processes inside VBFNLO was already tested in Refs. [83, 130–136].

To test the tri-boson production processes, a comparison between the cross-section given by Herwig + VBFNLO and VBFNLO standalone was performed. The parameters and cuts used for the comparison between Herwig+VBFNLO and VBFNLO standalone for the tri-boson production processes are the same used for the di-boson production processes, with the difference that four-flavors were used instead of two.

The reason to test just the interface instead of doing a new comparison with an external OLP was due to time constraints. For the tri-boson processes with two on-shell photons this comparison was done at LO, finding a complete agreement, but even at LO, for four and six final-state leptons, the time required to reach a reasonable precision made this test unreasonable due to time limitations.

Process	Component	Herwig + VBFNLO		Herwig + MadGraph		RD [%]
		σ [pb]	ϵ/σ [%]	σ [pb]	ϵ/σ [%]	
$pp \rightarrow e^+ \nu_e \mu^- \bar{\nu}_\mu$	Born	0.3055(4)	0.14	0.3048(4)	0.13	0.25
	Reals	0.05564(15)	0.28	0.0554(3)	0.45	0.47
	Virtual	0.08933(17)	0.2	0.08934(16)	0.18	0.016
$pp \rightarrow e^+ \nu_e \mu^- \mu^+$	Born	0.01873(4)	0.2	0.01866(3)	0.16	0.36
	Reals	0.00803(4)	0.53	0.008010(16)	0.19	0.26
	Virtual	0.006332(18)	0.28	0.006336(12)	0.19	0.066
$pp \rightarrow e^- \bar{\nu}_e \mu^- \mu^+$	Born	0.01136(2)	0.18	0.011335(16)	0.14	0.19
	Reals	0.005833(6)	0.11	0.005840(8)	0.14	0.12
	Virtual	0.003663(10)	0.28	0.003667(7)	0.20	0.11
$pp \rightarrow e^- e^+ \mu^- \mu^+$	Born	0.006915(12)	0.18	0.006937(9)	0.12	0.31
	Reals	0.000592(2)	0.38	0.000589(2)	0.39	0.44
	Virtual	0.001846(4)	0.23	0.001840(3)	0.16	0.33
$pp \rightarrow e^+ \nu_e \gamma$	Born	1.739(8)	0.44	1.742(6)	0.37	0.20
	Reals	1.893(9)	0.50	1.883(2)	0.12	0.48
	Virtual	0.2730(12)	0.45	0.2736(6)	0.21	0.23
$pp \rightarrow e^- \bar{\nu}_e \gamma$	Born	1.316(5)	0.41	1.32(5)	0.36	0.49
	Reals	1.585(7)	0.46	1.5858(19)	0.12	0.074
	Virtual	0.195776(8)	0.43	0.1951(4)	0.22	0.35
$pp \rightarrow e^- e^+ \gamma$	Born	1.227(4)	0.34	1.225(3)	0.26	0.10
	Reals	0.380(3)	0.16	0.3843(6)	0.9	1.0
	Virtual	0.1436(6)	0.38	0.1443(4)	0.29	0.51
$pp \rightarrow \gamma\gamma$	Born	35.04(3)	0.092	35.00(3)	0.092	0.11
	Reals	17.81(3)	0.19	17.78(3)	0.19	0.17
	Virtual	-0.054(11)	20.75	-0.049(11)	22.52	11.12

Table 4.1: Comparison of the different components contributing to the NLO cross-section between the OLPs VBFNLO and MadGraph, both interfaced through Herwig.

Process	Herwig + VBFNLO		VBFNLO standalone		RD [%]
	σ [pb]	ϵ/σ [%]	σ [pb]	ϵ/σ [%]	
$pp \rightarrow \gamma\gamma\gamma$	60.07(4)	0.06	60.03(3)	0.05	0.07
$pp \rightarrow e^+\bar{\nu}_e\gamma\gamma$	7.98(3)	0.39	7.9809(7)	0.009	0.04
$pp \rightarrow e^-\nu_e\gamma\gamma$	6.79(2)	0.35	6.8080(7)	0.010	0.28
$pp \rightarrow e^-\bar{\nu}_e\mu^+\nu_\mu\gamma$	2.902(10)	0.35	2.9139(3)	0.010	0.42
$pp \rightarrow e^+\nu_e\mu^-\bar{\nu}_\mu\tau^+\nu_\tau$	0.2623(6)	0.23	0.2621(2)	0.08	0.05
$pp \rightarrow e^-\bar{\nu}_e\mu^+\nu_\mu\tau^-\bar{\nu}_\tau$	0.1626(3)	0.16	0.16261(16)	0.10	0.010
$pp \rightarrow e^+\nu_e\mu^-\bar{\nu}_\mu\tau^-\tau^+$	0.04174(8)	0.20	0.041750(10)	0.02	0.03
$pp \rightarrow e^+\nu_e\mu^+\mu^-\gamma$	0.3142(15)	0.47	0.31283(4)	0.012	0.44
$pp \rightarrow e^-e^+\mu^-\mu^+\tau^+\nu_\tau$	0.003549(10)	0.28	0.0035499(9)	0.03	0.04
$pp \rightarrow e^-e^+\mu^-\mu^+\tau^-\bar{\nu}_\tau$	0.002135(4)	0.18	0.0021311(6)	0.03	0.16
$pp \rightarrow e^-e^+\gamma\gamma$	4.764(16)	0.33	4.7708(6)	0.012	0.14
$pp \rightarrow \nu_e\bar{\nu}_e\gamma\gamma$	4.498(10)	0.23	4.4939(6)	0.013	0.09
$pp \rightarrow e^-e^+\mu^-\mu^+\gamma$	0.1133(4)	0.36	0.11349(2)	0.02	0.19
$pp \rightarrow e^-e^+\mu^-\mu^+\tau^-\tau^+$	0.001214(6)	0.46	0.001219(3)	0.24	0.42

Table 4.2: Results of all the tri-boson production processes at NLO QCD without parton shower. The results in the first column were obtained using Herwig through the interface with VBFNLO to obtain the one-loop amplitude, while the results in the second column are obtained using VBFNLO standalone.

The results of the comparison between Herwig+VBFNLO and VBFNLO standalone can be seen in Table 4.2, where an agreement under the 0.5% is shown for all the tri-boson processes with leptonic decays.

The tests performed for di-boson and tri-boson production processes guarantees the validity of the interface implementation.

4.4 Phenomenological Results

This section is organized in two parts. In the first part, the factorization, renormalization and hard scale variations are analyzed for two different tri-boson production processes: One including a high multiplicity leptonic final-state, $pp \rightarrow e^+\nu_e\mu^-\bar{\nu}_\mu\tau^+\nu_\tau + X$, and another including one on-shell photon, $pp \rightarrow e^-\bar{\nu}_e\mu^+\nu_\mu\gamma + X$. In the second part, the impact of the Frixione isolation cut is analyzed, comparing the difference between the cut set in the event generation and in the analysis.

4.4.1 Scale Variations

Subsequently, an analysis of the different scale variation is presented for two different processes: $pp \rightarrow e^+\nu_e\mu^-\bar{\nu}_\mu\tau^+\nu_\tau + X$ and $pp \rightarrow e^-\bar{\nu}_e\mu^+\nu_\mu\gamma + X$. The runs were performed in the four flavor scheme, the MMHT2014 [145] PDF set was used and the CKM matrix was set to the identity matrix. Up to four jets were allowed, and they were defined using the anti- k_T algorithm with a radius parameter of $\delta = 0.4$. Moreover, the following cuts were used on all jets

$$p_{T,j} \geq 20 \text{ GeV}, \quad -2.5 \leq y_j \leq 2.5.$$

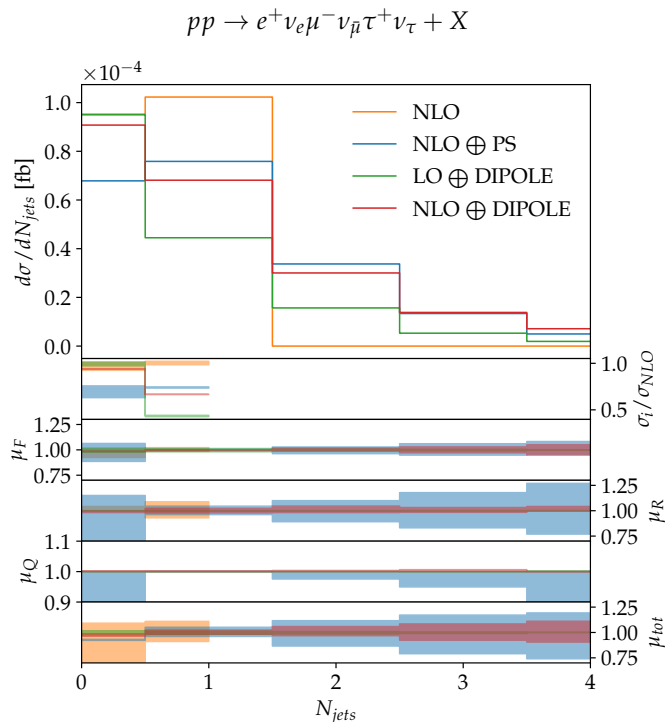


Figure 4.7: Cross-section as a function of the exclusive jet number. The NLO, in orange, only has events with 0 and 1 jet, as expected. The matched NLO plus parton shower, in blue for an angular ordered shower and in red for a dipole based one, shows up to four jets. The LO+dipole shower is shown in green.

Also, the following cuts were used on the final-state leptons

$$\begin{aligned}
 p_{T,\ell} &\geq 20 \text{ GeV}, & -2.5 \leq y_\ell \leq 2.5, \\
 m_{\ell\ell} &\geq 15 \text{ GeV}, & \Delta R_{\ell j} \geq 0.4, \quad \Delta R_{\ell\gamma} \geq 0.4.
 \end{aligned}$$

For the photon, we require the following cuts,

$$\begin{aligned}
 p_{T,\gamma} &\geq 30 \text{ GeV}, & -2.5 \leq y_\gamma \leq 2.5, \\
 \Delta R_{\gamma\gamma} &\geq 0.4.
 \end{aligned}$$

Finally, the Frixione isolation parameters were chosen following the tight isolation accord:

$$\delta_0 = 0.4, \quad \epsilon = 0.05.$$

The exclusive number of jets is plotted in Fig. 4.7. The NLO process only include contributions with one jet and zero jets, which are due to the real correction and a combination of the Born plus real correction contributions, respectively. The real corrections also participate on the zero jet contribution because the emitted parton can be reabsorbed by the jet algorithm into the emitter particle, while the two, three and four jet exclusive processes can not have any contribution from the fixed-order NLO calculation. At LO, using the dipole shower, all the jet multiplicities are populated, but the total cross-section is given by the LO, not shown in Fig. 4.7. For the NLO, there are two different showers, in blue an angular-ordered shower and in red a dipole based one. The dipole shower has a preference for zero multiplicity events while the angular-ordered one has a higher cross-section for

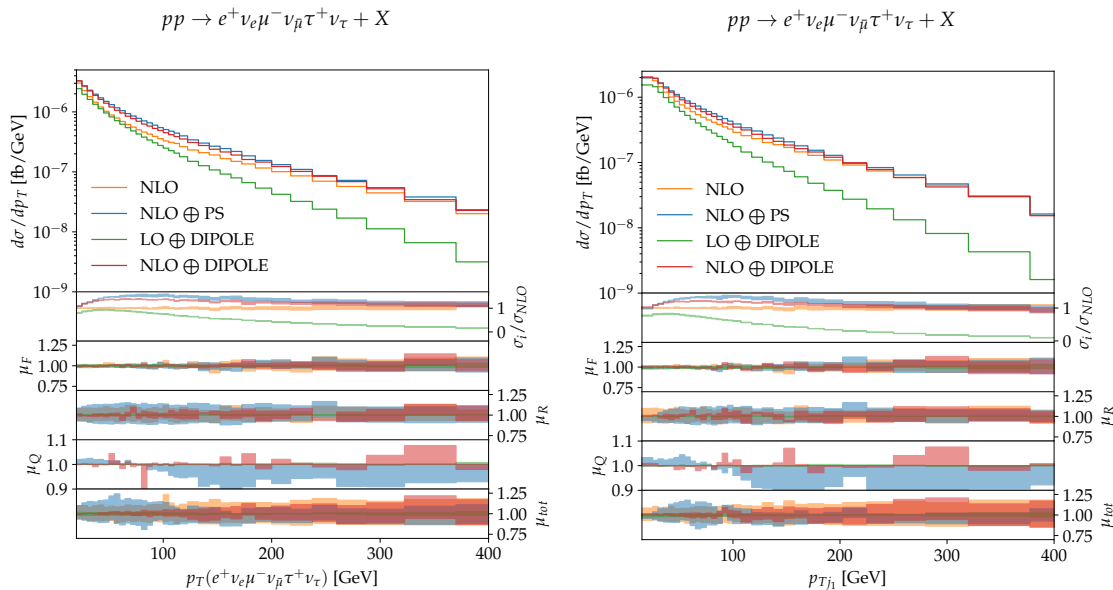


Figure 4.8: p_T of the six lepton system. The NLO calculation in orange is plotted together with two parton showers: an angular ordered shower shown in blue and a dipole based one in red. Also, for comparison the LO showered process is also shown in green.

one and two jet events. Also, the scale variation uncertainties are consistently lower for the dipole based parton shower.

The LO contribution for the $pp \rightarrow e^+ \nu_e \mu^- \bar{\nu}_\mu \tau^+ \nu_\tau$ process, without parton shower, has a fully leptonic final-state. At NLO, or in the showered case, the final-state leptons will have to recoil against the QCD radiation, which means that the observables of the full leptonic system will match the expected modifications due to the radiation pattern. As we explained in Sec. 2.3.8, the region of hard radiation is shaped by the real contribution to the NLO fixed-order process while the soft radiation region is mainly shaped by the parton shower. This is clear in Fig. 4.8 where the p_T of the full electroweak system is shown on the left figure and the p_T of the hardest jet on the right figure. The NLO matched with parton shower in the left figure approaches the LO showered result in the low p_T region, while the high p_T region agrees with the pure NLO result. Approximately, the same shape can be observed for the hardest jet, right figure, with small differences due to the contributions of the second, third and fourth jet in EW system's p_T . The scale variation in both plots is very stable, with relatively large values in the renormalization scale, close to 20%. The reason of the large uncertainty variations is that this distribution has a non-zero value for the first time at NLO, which effectively makes this observable a LO result. Another interesting thing is the inversion of the hard-scale variation around 90 GeV which probably is due to the separation between the soft and hard regions in the parton shower.

Observables that do not depend directly on the QCD radiation, like the p_T of the hardest charged lepton in the case of the $pp \rightarrow e^+ \nu_e \mu^- \bar{\nu}_\mu \tau^+ \nu_\tau + X$ process, or the p_T of the hardest photon in the $pp \rightarrow e^- \bar{\nu}_e \mu^+ \nu_\mu \gamma + X$ are expected to be left unchanged by the parton shower. The p_T of the hardest charged lepton in the $pp \rightarrow e^+ \nu_e \mu^- \bar{\nu}_\mu \tau^+ \nu_\tau + X$ process is shown in the left panel of Fig. 4.9, where an approximate agreement between the NLO fixed-order and NLO parton shower can be observed through all the range. This can also be observed from the p_T of the hardest photon in the $pp \rightarrow e^- \bar{\nu}_e \mu^+ \nu_\mu \gamma + X$ process, right panel of Fig. 4.9, where the difference between the LO and NLO is clear,

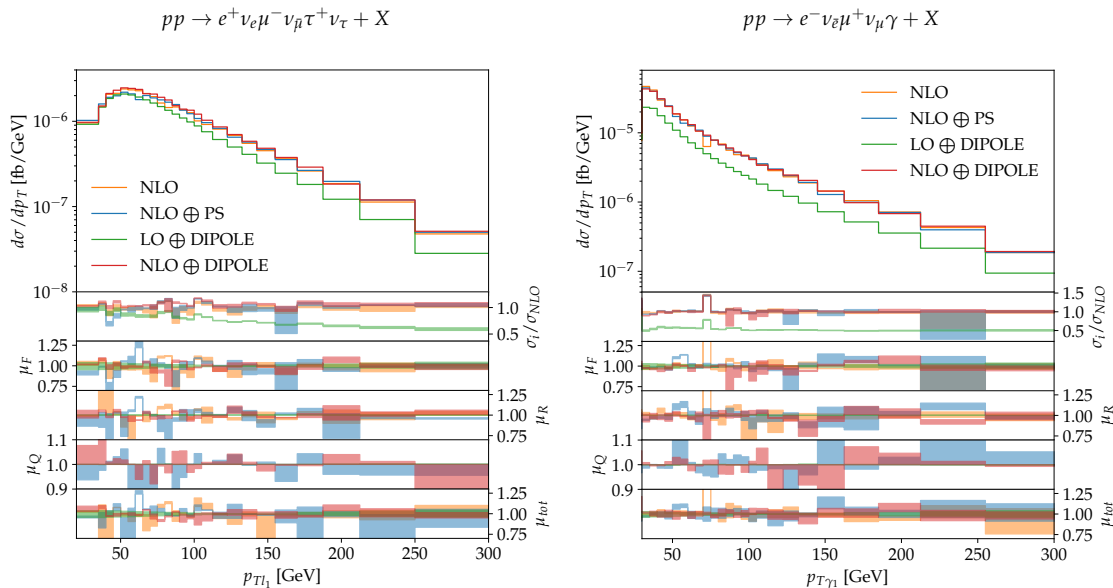


Figure 4.9: p_T of the hardest lepton in the $pp \rightarrow e^+ \nu_e \mu^- \bar{\nu}_\mu \tau^+ \nu_\tau + X$ process (left), and p_T of the photon in the $pp \rightarrow e^- \bar{\nu}_e \mu^+ \nu_\mu \gamma + X$ process (right). In both cases, we can observe the LO with dipole shower, in green, together with the fixed-order NLO in orange, and the NLO parton shower in blue and red.

but no modification in this observable due to the parton shower is visible. Moreover, the scale variations are smaller than in the case of the p_T of the jet. The reason is that this observable already exists at LO, the reduction of the scale uncertainties is due to the NLO correction. This also explains why the fluctuations are bigger in this observable due to the one loop corrections.

To look at the impact on the angular distributions, let us start analyzing the $\Delta R_{j_1 l_1}$ of the hardest charged lepton and the hardest jet in the case of the $pp \rightarrow e^+ \nu_e \mu^- \bar{\nu}_\mu \tau^+ \nu_\tau + X$ process, and $\Delta R_{\gamma l_1}$ between the photon and the hardest jet in the case of the $pp \rightarrow e^- \bar{\nu}_e \mu^+ \nu_\mu \gamma + X$ process, which can be seen in Fig. 4.10. Both distributions are similar, monotonically increasing from zero to the maximum value located at π , then monotonically decreasing to zero. The first part is dominated by the $\Delta\phi$ contribution, which reaches a maximum when the particles are back-to-back. The EW system is recoiling against the QCD radiation, and the hardest EW particle absorbs the majority of the hardest jet momentum. So, the peak at π is due to momentum conservation. A large NLO correction respect to the LO but with a modest effect of the parton shower can also be observed, which mainly makes smoother the distribution between the peak at π and the boundaries. Both distributions appear for the first time at NLO, the scale variations are large and smooth as expected. In contrast, the ΔR separation between the hardest charged lepton and the photon in the $pp \rightarrow e^- \bar{\nu}_e \mu^+ \nu_\mu \gamma + X$ process does not increase monotonically, it has two different local maximum, one situated near zero and another near π , the maximum near zero is allowed because the photon does not need to recoil against the charged lepton, there are other particles that can absorb the momenta. The scale variations in this case are smaller but with higher fluctuations, which again shows that this is a NLO observable, contrary to the case in Fig. 4.10.

Finally, observables related to the missing p_T for the $pp \rightarrow e^+ \nu_e \mu^- \bar{\nu}_\mu \tau^+ \nu_\tau + X$ process are shown in Fig. 4.12. In this process, the missing p_T is due to the three neutrinos that escape the detector undetected. The p_T curve due to these neutrinos can be seen in the

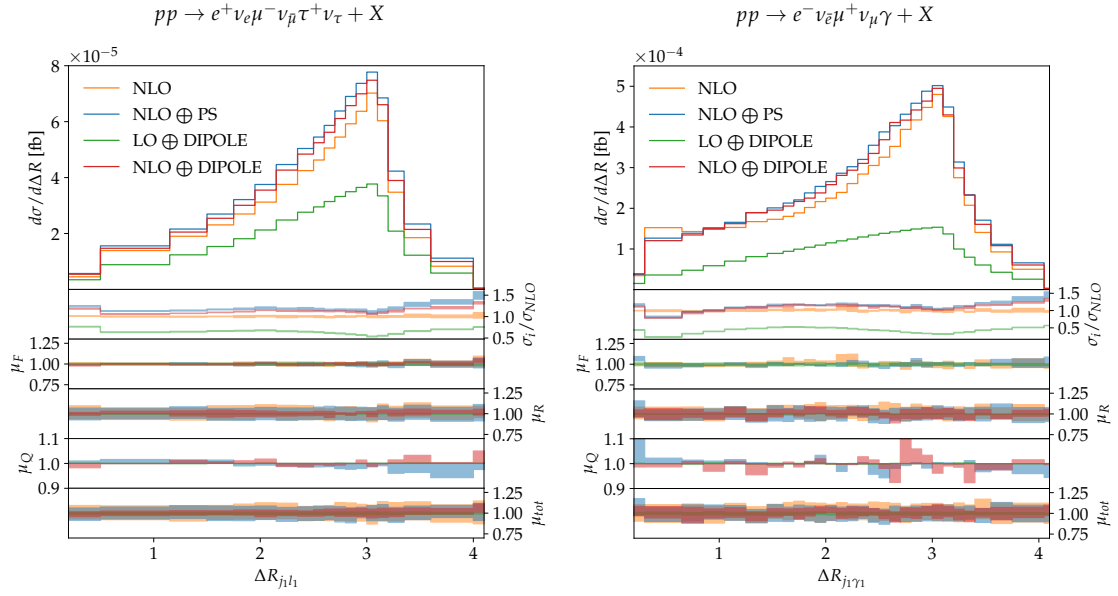


Figure 4.10: Euclidean distance in the $\phi - \eta$ plane, ΔR , for the hardest charged lepton and the hardest jet in the $pp \rightarrow e^+ \nu_e \mu^- \bar{\nu}_\mu \tau^+ \nu_\tau + X$ process on the left, and ΔR separation between the photon and the hardest jet in the $pp \rightarrow e^- \bar{\nu}_e \mu^+ \nu_\mu \gamma + X$ process on the right.

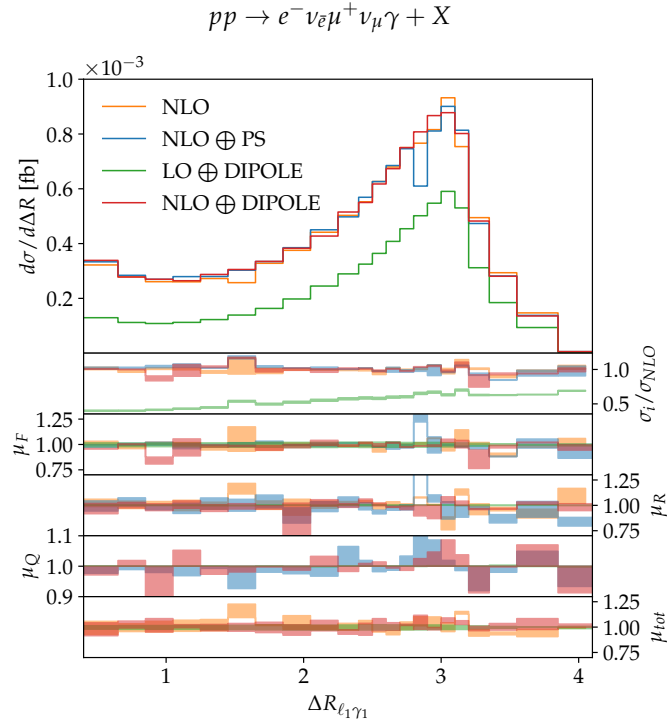


Figure 4.11: ΔR separation between the hardest charged lepton and the photon in the $pp \rightarrow e^- \bar{\nu}_e \mu^+ \nu_\mu \gamma + X$ process.

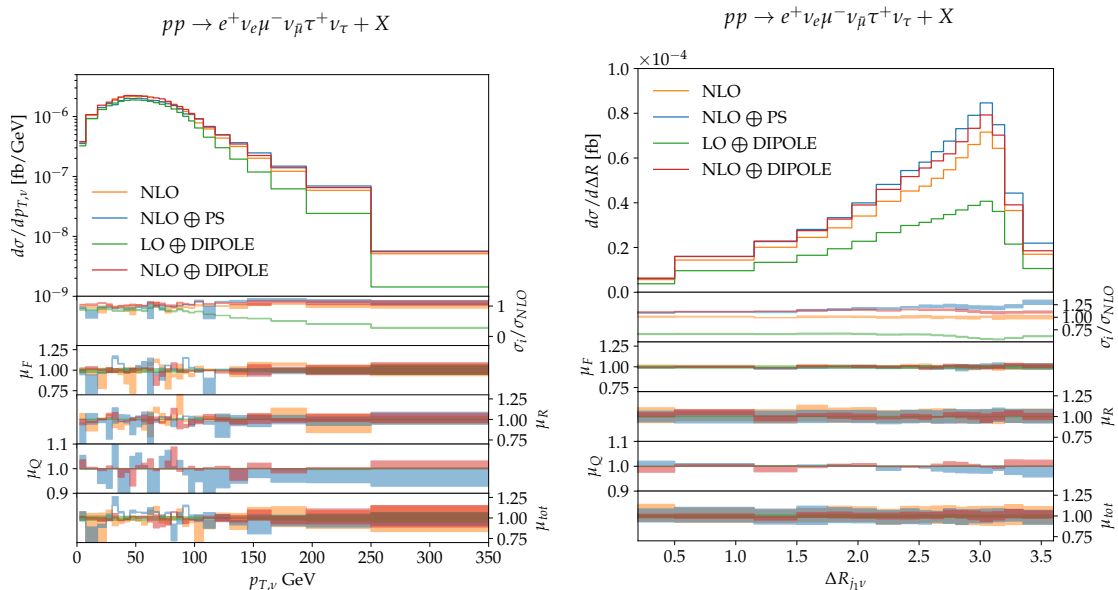


Figure 4.12: Observables due to the missing p_T : p_T miss of the $pp \rightarrow e^+ \nu_e \mu^- \bar{\nu}_\mu \tau^+ \nu_\tau + X$ process (left), and $\Delta R_{j_1 \nu}$ between the miss p_T component and the hardest jet.

left panel of Fig. 4.12. The parton shower leaves the distribution unaffected because it is independent of the QCD radiation pattern. The scale variations are small but with large fluctuations as expected for a NLO observable. The $\Delta R_{j_1 \nu}$ separation between the hardest jet and the missing momenta is shown in the right panel of Fig. 4.12. In contrast to the p_T distribution, this observable appears for the first time at NLO, so, the expected smooth and large scale variations can be observed. The shower has a mild effect on this distribution which basically makes smoother the NLO correction, but also slightly increases the height of the peak. The NLO correction with respect to the LO has a bigger impact, increasing also the total cross-section.

4.4.2 Frixione Isolation Cut

There are two different places where cuts on kinematic variables can be set: during the generation of the fixed-order event, which allows a faster integration due to the smaller phase space and the use importance and adaptive sampling methods to further improve the convergence, or during the analysis, once the event generation is finished. The MC returns the kinematic variables of the generated events, including parton shower, MPI and hadronization. This information can be used to reconstruct the event and define the different observables, including the cuts, at the expense of a slower phase space integration.

The implementation of the cuts at the generation level raises the problem that an event could pass the cuts at the fixed-order level but the changes due to the shower could allow an event to **migrate** through the cut boundaries. A cut at the analysis level will then reject this event, which will change the observable distributions and the total cross-section with respect to the generation level cuts.

To properly compare with the experimental setup, the cut definitions should be included into the analysis, leaving the generation cuts as inclusive as possible. This will obviously have an effect in the MC efficiency. To measure the impact of these migration effects for the Frixione isolation cut, we selected two different values of the cone radius $\delta_0 \in [0.4, 0.7]$ and four different values of the efficiency $\epsilon \in [0.05, 0.15, 0.5, 1.0]$. The case $\delta_0 = 0.4$, $\epsilon = 1.0$

does not appear in the figures below because these were the inclusive cut parameters used at the generation level for analysis level study.

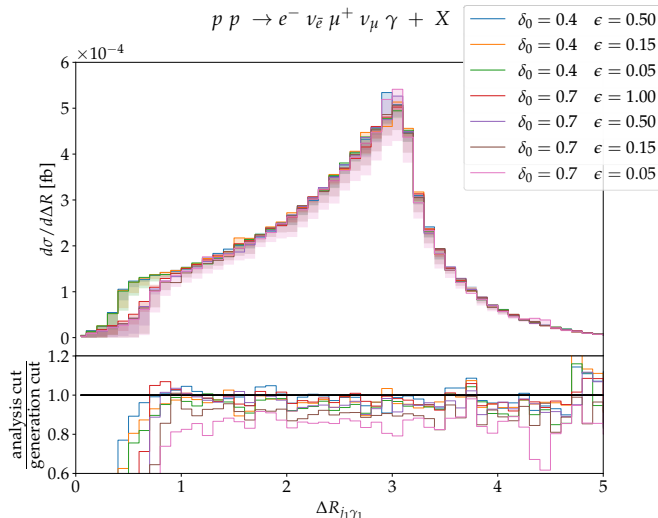


Figure 4.13: An observable involved in the Frixione isolation cut. $\Delta R_{j_1\gamma}$ between the hardest jet and the photon for two different values of the cone radius $\delta_0 \in [0.4, 0.7]$, and four different values of the efficiency $\epsilon \in [0.05, 0.15, 0.5, 1.0]$.

The $\Delta R_{j_1\gamma}$ between the photon and the hardest jet is an observable directly affected by the Frixione isolation cut, and can be seen in Fig. 4.13. The effect of the different cone radius is clearly observed in the splitting of the curves between $\Delta R_{j_1\gamma} = 0.4$ and $\Delta R_{j_1\gamma} = 0.7$. In that region, the migration effect is large due to the almost vanishing cross-section when the cut is implemented in the analysis compared to the relatively large cross-section with the cuts at the generation level, which is mainly due to the migration of the hardest jet. The rest of the distribution shows a constant loss of cross-section due to the migration of the other jets. The size of the effect depends on the different parameters of the isolation cut, which is smaller for the smallest cone radius, and it grows inversely proportional to the efficiency. For the tight-isolation criteria, $\delta_0 = 0.4$, $\epsilon = 0.05$ the value in the constant part of the distribution is approximately 5%, but it can be as large as 20% for parameter values like $\delta_0 = 0.7$, $\epsilon = 0.05$.

This migration effect depends on the exclusive number of jets, with a higher jet multiplicity there are more possibilities, i.e. a bigger chance, for cut migration. The cross-section as a function of the exclusive number of jets is shown in Fig. 4.14. The exclusive non-jet cross-section has a greater value for certain values of the parameters, ($\delta_0 = 0.7$, $\epsilon = 0.15$), ($\delta_0 = 0.7$, $\epsilon = 0.05$), and ($\delta_0 = 0.4$, $\epsilon = 0.05$), when the cuts are set in the analysis instead than in the generation, while all the other parameter values have smaller values. The reason could be due to the migration of some negative weight events coming from the real contribution. For higher jet multiplicities, the cross-section is lower for all the parameter values, and the amount of rejected events grows with the number of jets going from approximately 2% – 16%, in the one jet exclusive process, to 10% – 25%, for the four jet exclusive process.

Finally, the p_T of all the EW system is shown in Fig. 4.15. At LO, the process does not have any final-state colored particles, which means that the full EW system will have to make up for the QCD radiation momenta. There is a plateau in the loss of cross-section for high values of the p_T , but for small values of the p_T , the loss of cross-section goes to

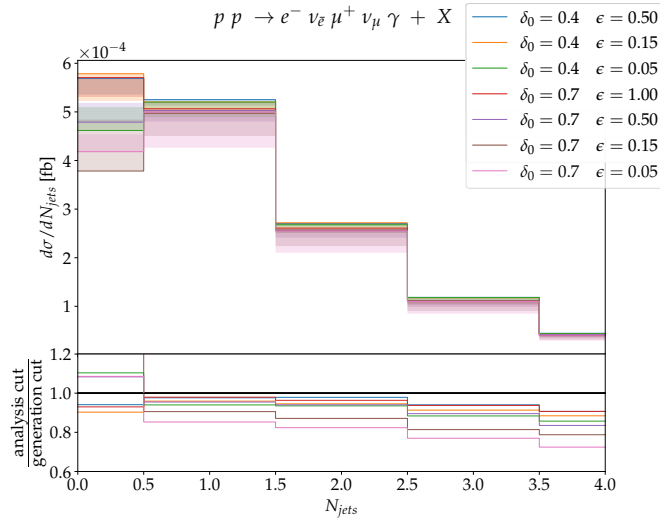


Figure 4.14: Cross-section as a function of the exclusive number of jets for different values of the Frixione isolation cut parameters. Two different values of the cone radius $\delta_0 \in [0.4, 0.7]$, and four different values of the efficiency $\epsilon \in [0.05, 0.15, 0.5, 1.0]$

zero. For values around $p_T \approx 5/10$ GeV, the quotient is only about 5% in the worst case, while for values of $p_T \approx 200$ GeV this quotient grows up to approximately 20%. This is probably due to the zero p_T region being dominated by the zero jet emissions. Remember that the full EW system has to recoil against the QCD radiation to conserve momentum, so, the p_T of the full EW system is exactly zero in the absence of QCD radiation. Then, it grows with p_T until it achieves a plateau where all the jet multiplicities contribute to the cross-section.

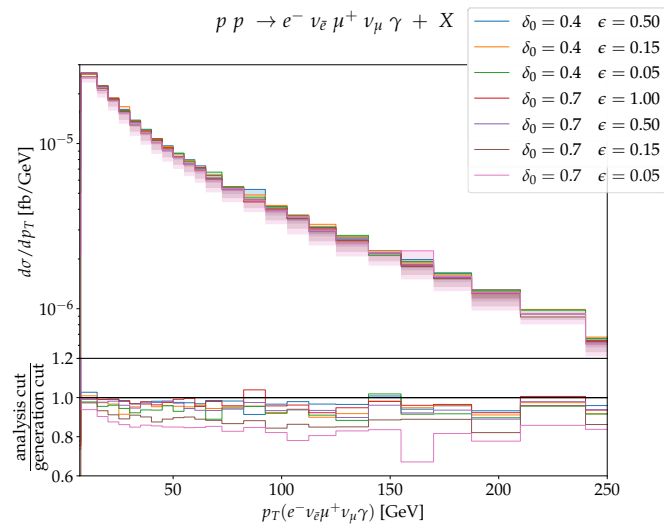


Figure 4.15: p_T of the full EW system for different values of the Frixione isolation cut parameters. Two different values of the cone radius $\delta_0 \in [0.4, 0.7]$, and four different values of the efficiency $\epsilon \in [0.05, 0.15, 0.5, 1.0]$

Chapter 5

Conclusions

Precise theoretical predictions have become mandatory due to improvements in experimental precision. An ongoing effort is being made to achieve the precision required for the LHC in the foreseeable future. Great progress has been achieved in the last decades. In this thesis, we aimed to contribute to these efforts through the implementation and phenomenological analysis of the $pp \rightarrow \gamma\gamma jj$ process in the parton level MC VBFNLO at NLO QCD, and the implementation of an interface following the BLHA standard for all di-boson and tri-boson processes in the framework of VBFNLO at NLO QCD, including a phenomenological study of the parton shower uncertainties for two tri-boson production processes, and the study of migration effects on the Frixione isolation cut.

The implementation of the $pp \rightarrow \gamma\gamma jj$ process through a vector boson exchange, in the VBS approximation, at NLO QCD in the parton level MC VBFNLO was explained in chapter 3, together with a set of tests performed to validate the code. A direct comparison between the event generator Sherpa and our implementation was performed at LO with an agreement under the 0.05%. The agreement of the LO amplitude for the $pp \rightarrow \gamma\gamma jjj$ process, which appears in the NLO correction as the real contribution, was around 2% due to the missing s-channel contribution and interference terms in VBFNLO. After removing the s-channel contribution from the Sherpa process, calculating it separately, an agreement of 0.02% and 0.19% for $p_{T,\gamma} > 20$ GeV, and $p_{T,\gamma} > 30$ GeV, respectively, was obtained. The dipole subtraction was validated and shown for two divergent regions: the collinear region between p_1 and the gluon, and the soft gluon region. The virtual contribution was tested through the numerical evaluation of the IR-poles in Fig. 3.14. The gauge invariance of the process was also checked, through the Ward identities, using the fact that the process has two on-shell final-state photons. We also compared the normalized scale variation between our process and the $pp \rightarrow e^-e^+\gamma jj$ with a cut to remove the $Z \rightarrow e^-e^+$ contribution.

The next section was dedicated to a phenomenological analysis of the $pp \rightarrow \gamma\gamma jj$ VBS process using our implementation. This analysis was performed considering as our only background the process with the same final-state but through a gluon exchange between the quark lines instead of a vector boson.

Two cuts involved in the VBS approximation were studied: the invariant mass of the two tagging jets, $m_{j_1 j_2}^{cut}$, and the rapidity separation between the two tagging jets, $\Delta y_{j_1 j_2}^{cut}$. The study of these two cuts showed that for smaller values of the rapidity separation cut, $\Delta y_{j_1 j_2}^{cut} < 4$, the significance with $L = 1\text{fb}^{-1}$, i.e. $S = \sigma_{EW}/\sqrt{\sigma_{QCD}}$, is approximately independent of $\Delta y_{j_1 j_2}^{cut}$ but has a great dependence on $m_{j_1 j_2}^{cut}$. The maximum is situated at $\Delta y_{j_1 j_2}^{cut} = 2.6$, $m_{j_1 j_2}^{cut} = 1280$ GeV, with a value of $S = 4.31$. The significance only varies between $S \in [4.0, 4.31]$ for $m_{j_1 j_2}^{cut} \in [800, 1500]$ GeV, and $\Delta y_{j_1 j_2}^{cut} \approx 3$, due to the small slope of the distribution close to the maximum.

The scale variation dependence was also studied for four different scale choices: a fixed scale at the Z boson mass, M_Z ; the square root of the product of the two tagging jet's transverse momenta, $\sqrt{p_{T,j_1} p_{T,j_2}}$; the momentum transfer in each quark line, Q_i ; and $H_T/2$ where H_T is the transverse energy sum of the final-state particles. The renormalization and factorization scale were varied together from 0.1 to 10 times the central value. The fixed M_Z scale gave the biggest central value correction from LO to NLO and had the largest variation in the range, both for LO and for NLO. The $\sqrt{p_{T,j_1} p_{T,j_2}}$ and the Q_i gave smaller variations and NLO correction compared with M_Z . The scale that gave the smaller NLO correction and had the smaller scale variation was $H_T/2$.

The Frixione isolation cut was used to isolate prompt photons from the fragmentation photons in an IR-safe manner. The Frixione cut has two different parameters: the radius of the cone around the photon, δ_0 , and the efficiency ϵ . No dependence on the photon isolation cut was observed at LO due to the $\Delta R_{\gamma j}$ cut. At NLO, we observed a small dependence on the efficiency compared with QCD channel. For $\delta_0 = 0.7$ in the range $\epsilon \in [0.01, 1.0]$, the VBS process only varies between $\sigma_{EW} \in [23.4, 24.705]$, while the QCD channel varies between $\sigma_{QCD} \in [21, 41.9]$.

A comparison with other similar VBS processes was performed. In particular, processes with one photon and one other vector boson with its specific leptonic decay were studied. The $\gamma^* \rightarrow l^+ l^-$, $Z \rightarrow l^+ l^- \gamma$, and $W \rightarrow l \nu_l \gamma$ contributions were reduced imposing appropriate cuts, and modified the H_T definition to include the mass of the vector bosons. The results showed that the $pp \rightarrow \gamma \gamma jj$ process had the largest significance for a set of equivalent cuts due to a significant larger total cross-section which is due to the photon being on-shell.

A set of selected differential distributions were studied. The two tagging jets invariant mass, $m_{j_1 j_2}$ in the QCD channel has a bigger cross-section for smaller values of the $m_{j_1 j_2}$, but has a greater decline; the VBS cross-section catches the QCD one at $m_{j_1 j_2} \approx 1500$ GeV. The smaller dependence of the cross-section for the VBS process is the reason that a cut on this observable had such a great effect on the significance. The relative geometry between both tagging jets was investigated through their rapidity and azimuthal angle separations. Both tagging jets are well separated, with a preference for relatively large rapidity separations, $\Delta y_{j_1 j_2} \approx 5 - 6$; and back-to-back in the azimuthal angle. The relative position of the photons with respect to the jets was investigated using the z^* observable, which showed that both photons are located between both jets. The rapidity and azimuthal separations between both photons showed a preference for small rapidity separations but larger azimuthal angle separations. The p_T shape for both photons was identical for the VBS and QCD process. The QCD channel had a higher peak at lower values of the p_T distribution but with a higher decline. Next, the invariant mass of the two photons for two different values of the Wilson coefficient for the $\widehat{B}_{\mu\nu} \widehat{B}^{\mu\nu} \widehat{B}_{\rho\sigma} \widehat{B}^{\rho\sigma}$ operator, $f_{T_8}/\Lambda^4 = 1200 \text{ TeV}^{-4}$ and $f_{T_8}/\Lambda^4 = 600 \text{ TeV}^{-4}$, was shown. This operator was chosen because it is the only operator involving the four neutral vector bosons, which is absent in the SM. The results showed that the modifications due to the effects of these operators in the $m_{\gamma\gamma}$ observable were located in the high-energy region. At $m_{\gamma\gamma} \lesssim 400$ GeV the results from the two different values for the anomalous vertex and the SM coincide. At large values, the predictions with the anomalous vertex break unitary bounds, which is expected for an effective theory without using form factors to ensure unitarity.

To conclude, an interface following the Binoth-LesHouches Accord (BLHA) for all di-boson and tri-boson processes with leptonic decays in VBFNLO was implemented. The interface was tested in the di-boson case with a comparison, for each NLO component separately, between Herwig + VBFNLO and Herwig + MadGraph in the two flavor scheme.

In the tri-boson case, the VBFNLO standalone result was compared to the Herwig + VBFNLO result in the four flavor scheme.

A scale variation uncertainty study of the $pp \rightarrow e^+\nu_e\mu^-\bar{\nu}_\mu\tau^+\nu_\tau + X$ and $pp \rightarrow e^-\bar{\nu}_e\mu^+\nu_\mu\gamma + X$ was performed using the implemented interface. Two parton showers were used in our analysis: an angular ordered shower and a dipole based one. The p_T of the full electroweak system was investigated, which has to recoil against the QCD radiation; the full electroweak system at LO has $p_T = 0$ due to momentum conservation. The scale variations were large, with small fluctuations, consistent with a LO observable. At low p_T the LO plus parton shower and the NLO at fixed order coincide, as expected, while at large p_T the NLO plus parton shower and NLO fixed-order agree, showing that the large p_T part of the spectrum is given mainly by the real contribution. The hard veto scale for the angular ordered shower shows an inversion in boundary between these two behaviors. The electroweak observables are not modified by the shower, and their scale variation uncertainty bands are smaller but with higher fluctuations due to the instabilities of the loop calculations. These effects can be consistently seen through all the differential distributions, the observables which only include electroweak particles, like the p_{T,l_1} , $p_{T,\gamma}$, $p_{T,\nu}$, and $\Delta R_{l_1,\gamma}$, have small scale uncertainties with larger fluctuations, while the ones including jets show larger and smoother scale variations.

The cross-section loss in the Frixione isolation cut due to the migration through cut boundaries in the $pp \rightarrow e^-\bar{\nu}_e\mu^+\nu_\mu\gamma + X$ process was investigated for two different values of the radius parameter, $\delta_0 \in [0.4, 0.7]$, and four values of the efficiency, $\epsilon \in [0.05, 0.15, 0.5, 1.0]$. The distributions were separately calculated with this cut at the generation level and at the analysis level. The $\Delta R_{j_1,\gamma}$ is directly affected by this cut, where the boundary crossing of the hardest jet can be seen at $\Delta R_{j_1,\gamma} < 0.4, 0.7$. The effect of the other jets can also be seen in this observable through the plateau for higher values of $\Delta R_{j_1,\gamma}$. The migration effect as a function of the exclusive number of jets was also studied in Fig. 4.14, where higher loss in cross-section was seen for higher jet multiplicities. Finally, the p_T of the full electroweak system showed that the cut migration effects were smaller at small p_T , consistent with the smaller cross-section loss for lower multiplicities.

This thesis has emphasized the necessity of precise theoretical calculations in the ongoing effort to match the future experimental precision needed to reveal new physics BSM, and we have aimed to contribute to this effort with the implementation of new tools and the phenomenological study of relevant processes.

Chapter 6

Resum

El segle XX va ser una època de revolucions en la Física. Els fonaments teòrics d'aquesta ciència estaven dominats per les teories clàssiques de Newton, postulada tres segles abans i de la teoria de l'electromagnetisme intuïda per Faraday i formalitzada per Maxwell al llarg del segle XIX. Aquestes teories serien finalment substituïdes per la Mecànica Quàntica i la Relativitat General. Mentre a finals del segle XIX, a les principals reunions de físics, es podia sentir parlar de la teoria del flogist o de quin era el moviment de la Terra dintre de l'èter. A finals del segle XX, a aquestes mateixes reunions, se sentiria parlar d'unificació, de matèria i energia fosca o de dimensions extra.

La unió de la Mecànica Quàntica i la Relativitat Especial en les anomenades Teories Quàntiques de Camps i, en especial, en el Model Estàndard de la Física de Partícules (SM, per les seues segles en anglés), ens han donat la capacitat de fer prediccions amb una precisió que mai havia sigut vista amb anterioritat. Un exemple comú és la predicció del moment anòmal de l'electró que mostra un acord amb l'experiment de deu xifres significatives.

Al llarg dels anys 1908-1913, els físics Hans Geiger i Ernest Marsden, sota la supervisió d'Ernest Rutherford van dur a terme un conjunt d'experiments que consistien a llançar nuclis d'heli contra una fina làmina d'or, i permeteren determinar l'estructura de l'àtom. Experiments semblants són els que continuen duent-se a terme en l'actualitat, amb la diferència que per determinar cada vegada estructures més xicotetes, l'energia, i la mida, d'aquests experiments ha augmentat dràsticament. El més gran d'aquests és el Gran Col·lisionador d'Hadrons (LHC, per les seues segles en anglés), un anell de 27 km situat baix terra en la frontera entre França i Suïssa. Al LHC s'acceleren protons (i ions pesats) fins velocitats properes a la de la llum i es fan col·lisionar en quatre grans experiments que mesuren les restes d'aquestes col·lisions. Un gran esforç experimental, que inclou milers de persones, entre físics i enginyers, ha permés construir, mantindre i analitzar les dades d'aquest experiment.

Per poder comparar les dades obtingudes al LHC amb els nostres models teòrics, i avançar en el nostre coneixement de les lleis fonamentals, un esforç igualment gran és requerit per part de la comunitat de físics teòrics. Els càlculs involucrats en obtindre observables que puguen ser comparats amb els experiments són llargs i complicats. Aquests es poden dur a terme de dues formes diferents. La primera manera és anomenada teoria de camps en una xarxa, on una part finita de l'espai-temps es divideix en un reticle discret de punts. Les limitacions de la teoria de camps en una xarxa no permet avui dia dur a terme els càlculs requerits per obtindre observables relacionats amb les col·lisions d'alta energia al LHC. L'altra opció, la utilitzada majoritàriament en altes energies, s'anomena teoria de pertorbacions. En teoria de pertorbacions el resultat s'obté de sumar un nombre finit de

termes d'una sèrie en funció d'una variable xicoteta, sabent el resultat exacte per al valor de la variable d'expansió igual a zero. Els diferents termes en teoria de perturbacions es poden escriure mitjançant uns diagrames utilitzats per primera vegada pel físic nord-americà Richard Feynman i anomenats, en el seu honor, diagrames de Feynman. El nombre de diagrames a cada ordre en la sèrie perturbativa creix molt ràpidament i fa que els càlculs a ordres superiors estiga fora del nostre abast a pesar de la utilització d'eines informàtiques. A més a més, la constant d'acoblament de la interacció forta, la qual és fonamental per descriure correctament les interaccions entre partícules al LHC, esdevé molt gran a baixes energies fent que la teoria de perturbacions no done resultats correctes.

Quan es va construir el LHC existien motius prou convinents per a fer pensar que una partícula escalar, involucrada en la consistència del SM i anomenada bosó de Higgs, anava a ser detectada directament. L'absència d'aquesta partícula hauria causat un gran revolt en la física teòrica. Afortunadament, l'any 2012 les col·laboracions ATLAS i CMS, experiments del LHC, van confirmar el descobriment d'un bosó escalar compatible amb el bosó de Higgs. Amb el descobriment del bosó de Higgs, el SM està complet i és internament consistent.

Així i tot, tenim raons teòriques per pensar que el SM no és la descripció definitiva de l'Univers. Entre altres, l'absència de la interacció gravitatòria, l'absència d'una partícula que pugui explicar la matèria fosca, l'absència d'un mecanisme que expliqui correctament l'energia fosca, l'absència d'una explicació l'origen de les masses dels neutrins i l'absència d'un mecanisme que done la suficient violació de CP per a explicar l'asimetria entre matèria i antimatèria al nostre univers. A pesar de totes aquestes mancances, l'èxit del SM i de LHC es pot observar en la falta de desviacions significatives entre les prediccions teòriques i les dades experimentals. Durant aquests anys, l'esperança d'observar nova física directament que resolguera aquests problemes, o almenys una part, ha anat disminuint d'acord amb l'augment de l'estadística recol·lectada als experiments del LHC. Per fer front a la possible incapacitat dels experiments actuals d'observar nova física directament, altres estratègies han sigut desenvolupades. Entre elles, la física de precisió, que busca trobar xicotetes diferències en els observables de les partícules que es poden generar al LHC a causa d'una possible física a energies no accessibles directament.

La física de precisió va mà en mà amb les anomenades Teories Efectives de Camps i requereix el càlcul en teoria de perturbacions a ordres alts, així com sumar contribucions degudes a la radiació de QCD a tots els ordres. Les Teories Efectives de Camps han esdevingut una ferramenta ideal per sistematitzar els possibles efectes de física a altes energies en la teoria a baixes energies. Aquests efectes venen descrits pels valors d'uns paràmetres anomenats coeficients de Wilson que acompanyen operadors construïts amb les simetries i les partícules del SM però amb dimensions de massa superiors a quatre. Al SM, tots aquests coeficients són zero, així qualsevol desviació de la teoria respecte del SM ve donat per valors dels coeficients de Wilson diferents de zero. A més a més, informació sobre les característiques de la teoria a altes energies es pot extraure dels operadors particulars que contribueixen.

En la pràctica, els càlculs esmentats fins ara no es duen a terme analíticament sinó que s'implementen en uns programes d'ordinador anomenats generadors de Monte Carlo (MC). Els MC simulen esdeveniments que poden ser comparats directament amb els resultats obtinguts als experiments. Els càlculs requerits per dur a terme aquesta comparació se separen en diferents components depenent de l'escala d'energia típica del subprocés.

La primera component del càlcul és la de l'estructura interna del protó. Al LHC es col·lionen principalment protons, aquests són partícules compostes mantingudes per la interacció forta. A les baixes energies involucrades en la coherència del protó, la

interacció forta és molt intensa i la teoria de pertorbacions no és una ferramenta apropiada. Afortunadament, quan col·lionem protons a les energies típiques del LHC, els components del protó, anomenades partons i que a aquestes energies es comporten com partícules lliures, són els que realment participen en la col·lisió. L'estructura interna del protó només ens dona la probabilitat que certa component siga la involucrada en la col·lisió d'altres energies. A més a més, aquesta estructura és universal i pot ser deduïda d'altres experiments. L'evolució de l'estructura del protó sí que és pertorbativa i pot ser calculada amb les equacions DGLAP una vegada obtinguda a una escala particular.

La component que més informació ens dona és la col·lisió a altes energies entre partons. A aquesta escala d'energia més alta, la interacció forta sí que és pertorbativa i podem utilitzar teoria de pertorbacions per obtindre el resultat d'aquesta part del càlcul a qualsevol ordre, encara que a causa de les dificultats inherents al càlcul només ordres baixos, primer, segon o tercer ordre depenent del nombre de partícules externes, ha sigut obtingut. A més a més, en aquesta part del càlcul trobem les famoses divergències que van portar de cap als físics a mitjan segle passat. Aquestes divergències poden trobar-se als dos extrems d'energies. A altes energies, anomenades divergències ultraviolades (UV), que es tracten renormalitzant els paràmetres del Lagrangià i a baixes energies, anomenades infraroges (IR) que desapareixen si tenim una especial cura a l'hora de definir els nostres observables. La complexitat dels càlculs ha fet que hagen aparegut programes especialitzats, anomenats proveïdors d'amplituds a un bucle (OLP, per les seues segles en anglés), que com el seu nom indica calculen l'amplitud a segon ordre i se la comuniquen al MC, que històricament sol només tindre amplituds a primer ordre. La comunicació entre l'OLP i el MC es porta a terme a través d'una interfície proposta a Les Houches l'any 2010.

Per altra banda, al LHC podem observar que els estats finals tenen una gran multiplicitat de partícules neutres respecte a la interacció forta que formen estructures col·limades anomenades jets. Aquests dos fenòmens corresponen a les dues últimes components del càlcul. La cascada partònica, que simula l'emissió de partícules carregades baix la interacció forta, i l'hadronització, en la qual els MC utilitzen models heurístics per agrupar les partícules de la cascada partònica en les partícules que són observades als experiments.

En aquesta tesi, la major part dels càlculs requerits per obtindre observables al LHC han sigut portats a terme amb dos projectes diferents. La implementació d'un procés a NLO QCD en el generador de Monte Carlo a nivell partònic VBFNLO i en la implementació d'una interfície entre VBFNLO i el generador d'esdeveniments Herwig que permet obtindre observables complets a partir de l'amplitud a NLO QCD calculada per VBFNLO per als processos amb 4 i 6 fermions a l'estat final d'origen electrofeble.

El treball està dividit en 6 capítols diferents, una introducció al tema, el desenvolupament teòric, la implementació de la producció de dos fotons en l'aproximació VBS en VBFNLO, la implementació de la interfície entre VBFNLO i Herwig i, finalment, les conclusions i aquest resum. A continuació anem a fer un resum dels tres capítols principals, explicant on faça falta els resultats més rellevants.

El capítol dos, fonaments teòrics, comença amb una xicoteta introducció al SM. Les principals nocions que ens faran falta a la resta de la tesi són explicades, entre elles la de Teoria Gauge, la llibertat asimptòtica, el confinament i la ruptura espontània de la simetria. A continuació passem a explicar la Teoria Efectiva del Model Estàndard (SMEFT, per les seues segles en anglés), teoria que té com a límit de baixes energies el SM però inclou operadors amb dimensions de massa superiors a quatre que sistematitzen les contribucions de graus de llibertat no accessibles a baixes energies. En particular, hem donat explícitament una llista dels operadors de dimensió 6 i dimensió 8 construïts amb els bosons electrodèbils i el Higgs.

La resta del capítol, dintre de la secció "física del LHC", descriu tècnicament les ferramentes necessàries per a obtenir resultats teòrics que puguin ser comparats amb l'experiment. Comencem amb una breu introducció del LHC com a aparell experimental i descrivim les coordenades més utilitzades per descriure els esdeveniments observats, en particular donem una motivació teòrica per la utilització de la rapidesa i la pseudorapidesa. Continuem amb una descripció del model partònic, que ens permet separar les diverses components del càlcul en les seues parts pertorbatives i no pertorbatives, les funcions de distribució partònica, que ens donen l'estructura del protó, i les equacions d'evolució DGLAP.

A continuació ens centrem en la part pertorbativa del càlcul i descrivim con dur a terme càlculs pertorbatius a NLO QCD d'una manera totalment general. Els càlculs a NLO estan dividits en dues contribucions diferents: la contribució virtual i la contribució real. La contribució virtual està formada per diagrames de Feynman amb bucles que contenen divergències, tant UV com IR. Les divergències UV, com hem esmentat abans, s'eliminen mitjançant la renormalització dels paràmetres del Lagrangià. Les divergències IR desapareixeran de l'observable final, si aquest compleix certes condicions, quan sumem la part virtual i la part real.

La contribució virtual està formada per diagrames de Feynman que contenen bucles amb cert nombre de moments externs. Com que les deltes de Dirac de conservació del moment no són suficients per a eliminar totes les integrals en aquest cas, una integral amb un moment arbitrari dintre del bucle roman. Les integrals que apareixen es classifiquen depenent del nombre de propagadors i del nombre d'índex Lorentz. Les integrals sense cap índex Lorentz s'anomenen escalars i són molt importants, ja que qualsevol integral que apareix a un bucle pot ser reduïda a una combinació lineal d'integrals escalars amb quatre denominadors o menys. Aquesta reducció, anomenada reducció de Passarino-Veltman, es porta a terme recursivament. Durant el procés de reducció, determinants de matrius de Gram apareixen al denominador. En situacions cinemàtiques degenerades, per exemple quan les partícules són col·lineals, aquest determinant és zero i complica el càlcul numèric dels coeficients tensorials de la combinació lineal.

La contribució real està formada per diagrames amb una emissió QCD extra. És a dir, té una cinemàtica amb una partícula més que el primer ordre o la part virtual. El càlcul dels diagrames presents en aquesta contribució són diagrames sense bucles i, per tant, es calculen de manera anàloga al primer ordre. La contribució real no conté divergències UV però sí divergències IR. Les divergències IR apareixen quan l'emissió QCD extra té una cinemàtica degenerada amb la partícula que l'emet i, per tant, es redueix a la cinemàtica de primer ordre. Aquestes divergències tenen el mateix origen que les divergències IR de la part virtual i tenen la mateixa magnitud però signe oposat si tot l'espai fàsic on apareixen aquestes divergències se té en compte. És a dir, la suma de la contribució virtual i real serà finita si les regions divergents de l'espai fàsic se tenen en compte en la part real.

Seguidament, es discuteixen els anomenats observables de jets. Hi ha dos tipus d'observables que podem considerar, observables inclusius, com per exemple la secció eficaç total, o observables exclusius on només estem interessats en parts d'un procés. La utilitat de considerar observables exclusius es deu, entre altres coses, a què ens dona la capacitat de considerar limitacions experimentals o centrar-nos en regions de l'espai fàsic que ens permeten separar parts interessants de la física des del punt de vista teòric d'altres parts que contenen menys informació. De totes maneres, quan considerem observables exclusius hem de ser curosos, ja que és fàcil espatllar la cancel·lació de les divergències infraroges. Els observables segurs, aquells que no espatllen la cancel·lació de les divergències, són aquells que són independents de l'estructura exacta de la radiació QCD. En particular,

els més utilitzats s'anomenen observables de jets perquè reproduïxen l'estructura de jet de la radiació QCD observada als col·lisionadors.

Una vegada hem explicat com obtenir els observables a NLO QCD, passem a explicar què és un Monte Carlo. En poques paraules, és una forma de fer integrals de dimensió alta mitjançant un mostreig finit d'aquesta. En aquesta secció, donem una comparació amb altres formes de dur a terme la integració numèrica i observem com per a dimensions grans Monte Carlo és la millor ferramenta, ja que la dependència amb el nombre d'avaluacions del valor esperat de l'error no depèn de la dimensió de la integral. A més a més, expliquem breument l'ús d'algunes tècniques com el mostreig d'importància que millora raonablement la convergència de la integral.

Com s'ha dit abans, les divergències infraroges desapareixen de la suma de les contribucions virtual i real per observables segurs. Però la integració numèrica, utilitzant Monte Carlo, de les dues contribucions es fa de forma separada. Això implica que les divergències infraroges no es cancel·len i, per tant, poden aparèixer inestabilitats numèriques. Per evitar aquest problema utilitzem el mètode de sostracció de Catani-Seymour, on afegim una contribució tant a la part real com a la virtual amb signes oposats que cancel·len les divergències punt a punt abans d'integrar. En la subsecció sobre Catani-Seymour expliquem detalladament l'algorisme i donem l'exemple de l'emissió d'un gluó des d'una línia de quark amb un bosó vectorial que serà útil posteriorment.

En la següent subsecció s'explica la implementació de la cascada partònica, una manera de considerar part de la contribució de la radiació QCD a tots els ordres. Per a l'emissió d'una partícula carregada baix la interacció forta, en l'aproximació col·lineal i de baixes energies, la secció eficaç factoritza en la secció eficaç del procés sense la partícula emesa i un terme que depèn del desdoblament particular pel qual la partícula s'ha emés. Aquesta factorització té una interpretació probabilística i ens permet calcular aproximadament l'emissió d'un nombre arbitrari de partícules carregades baix la interacció forta fins a aplegar a certa escala d'energies baixa on l'hadronització té lloc. En el cas que el desdoblament siga d'alguna partícula en l'estat inicial, haurem de tindre en compte l'efecte sobre les funcions de distribució partònica.

Finalment, acabem el capítol amb l'explicació d'un tall de l'espai fàsic degut a Stefano Frixione. Quan tenim un procés que té fotons a l'estat final, aquests fotons podem vindre de dos llocs diferents: del procés d'alta energia en la col·lisió dels dos partons o de la radiació electromagnètica. El primer cas és el que ens interessa perquè ens dona més informació sobre la física fonamental darrere de la col·lisió. Generalment, els fotons deguts a la radiació electromagnètica se troben principalment en una direcció col·lineal a la partícula emissora. Això ens indica que podríem utilitzar un con que eliminara aquesta part de l'espai fàsic. El problema amb aquest procediment és que l'eliminació d'aquesta part de l'espai fàsic pot espatllar la cancel·lació de les divergències infraroges. El tall degut a Frixione ens permet eliminar els processos amb fotons deguts a la radiació electromagnètica de forma segura, és a dir, sense espatllar la cancel·lació de les divergències infraroges.

El capítol tres està centrat en la implementació del procés amb dos fotons i dos jets a l'estat final en l'aproximació VBS. Comencem amb una xicoteta introducció on s'explica amb detall el nostre procés. Hi ha dues maneres diferents, a primer ordre, d'aconseguir el nostre estat final dependent del nombre de constants d'acoblament electromagnètiques o fortes. Anomenarem EW al cas on totes les constants d'acoblament són electromagnètiques i QCD quan la mitat són electromagnètiques i l'altra mitat pertanyen a la interacció forta. Considerarem el canal QCD com un fons de soroll mentre que el cas EW en l'aproximació VBS serà el nostre senyal. El canal EW consisteix de topologies de tres tipus, anomenades canal-s, canal-t i canal-u.

Els canals-t/u contenen informació sobre els vèrtexs amb tres o quatre bosons vectorials que són d'interés en la cerca de física més enllà del SM (BSM, per les seues sigles en anglés). Per altra banda, els canals-t/u se poden separar del canal-s, ja que ambdós omplim regions diferents de l'espai fàsic. Els canals-t/u generen jets en la direcció dels protons inicials i fotons en la regió central del detector mentre que el canal-s presenta una corba de Breit-Wigner al voltant de la massa del bosó intermedi. Això ens permet eliminar la contribució del canal-s fàcilment mitjançant l'eliminació de la regió de l'espai fàsic on aquesta és important. Com utilitzant aquest espai fàsic restringit, la contribució del canal-s és negligible, podem calcular només els canals-t/u i obtindre una bona aproximació al resultat complet, aquesta aproximació és el que hem anomenat abans l'aproximació VBS. En la introducció donem una taula a primer ordre on es mostra que efectivament aquesta aproximació està justificada i dona el mateix valor que el càlcul complet amb un error per sota de l'un per mil. Aquesta secció acaba amb la descripció dels subprocessos i la mostra dels diagrames de Feynman que contribueixen al nostre procés.

En la següent secció, implementació, es mostra la implementació del procés descrit en la secció anterior al generador de Monte Carlo a nivell partònic VBFNLO a NLO QCD. La implementació està dividida en tres parts: el primer ordre, la contribució real i la contribució virtual. Durant l'explicació de la implementació del primer ordre aprofitem per a descriure amb detall les subrutines de Fortran que s'utilitzen en VBFNLO per construir els diagrames de Feynman. Una vegada aquestes han sigut descrites expliquem com ajuntar-les per obtindre els diagrames, primer en el cas amb tots els bosons vectorials neutres i després per al cas on apareixen bosons vectorials carregats. En la implementació de la part real ens centrem en els termes de Catani-Seymour, ja que la implementació dels diagrames és anàloga al cas anterior. Un punt que hem de tindre en compte és l'absorció per part de les funcions de distribució partònica de les divergències col·lineals de l'estat inicial. A continuació, ens centrem en la contribució virtual, en aquesta secció calculem com a exemple la correcció d'una línia de quark amb un bosó vectorial adjunt. El càlcul utilitza les tècniques mostrades a la secció sobre fonaments teòrics i aplega a un resultat finit després de la renormalització i l'ús de la sostracció de Catani-Seymour. A banda, expliquem breument com s'implementen en el codi les correccions a línies de quark amb dos o tres bosons adjunts que també contribueixen al nostre procés. Finalment, acabem aquesta secció amb la implementació dels vèrtex anòmals deguts a operadors de dimensió 6 i 8, mostrats al capítol 2.

Continuem amb una secció on mostrem les proves que hem fet per assegurar que el procés està correctament implementat. La primera comprovació ha sigut una comparació directa amb un altre generador de Monte Carlo, Sherpa, a primer ordre. Sherpa ens dona el resultat EW complet a primer ordre, així que trobem certa desviació respecte al nostre resultat. En el cas del primer ordre aquesta desviació és menor del 0.04% però per a la part real és fins del 2%. Com la part real només és un 5% del resultat total, aquest error continua sent negligible. A més a més, per assegurar-nos que efectivament aquesta desviació és deguda per no considerar el canal-s, calculem el canal-s i els sostraiem al resultat de Sherpa, amb el resultat sostret, la desviació passa a ser del 0.02%. Un altre test ha sigut el càlcul numèric de les divergències infraroges donades per les subrutines que calculen els bucles en VBFNLO, una comparació amb el valor analític conegut mostra que aquests són compatibles menys per l'error numèric. També hem fet una comparació deguda a la variació de la secció eficaç amb l'escala d'energies. Aquesta dependència amb l'escala és un efecte a causa del truncament de la sèrie pertorbativa i és una indicació de l'error comés per negligir ordres superiors. En el nostre cas, hem comparat la variació amb l'escala del nostre procés amb un altre procés anteriorment implementat en VBFNLO que

hauria de tindre la mateixa dependència baix certes condicions. Finalment, hem vist que les identitats de Ward se satisfieien menys pels errors numèrics.

Una vegada el procés ha estat implementat i la implementació comprovada passem a una anàlisi fenomenològica del procés. En la secció següent duem a terme aquesta anàlisi i a continuació expliquem els resultats més importants obtinguts. El primer resultat d'interés ha sigut el tall de la massa invariant dels dos jets, aquest tall que està relacionat amb l'aproximació VBS, també té un efecte important en separar el nostre senyal del fons. Usualment, aquest tall té un valor al voltant de 400 GeV però en el nostre cas, el valor d'aquest tall per una significança òptima és més proper a 800 GeV. Un altre punt d'interés és que tant la significança com la secció eficaç total del nostre procés és major que els processos equivalents on un fotó és substituït per un altre bosó vectorial i la seua desintegració leptònica. La forma general del nostre procés té les mateixes característiques que les observades en altres processos en l'aproximació VBS, dos jets energètics en la direcció dels protons inicials i els bosons vectorials en la part central del detector. Un observable interessant descobert en aquest estudi ha sigut la separació en l'angle azimutal del segon jet en moment transversal i el fotó més energètic. Aquest observable ajuda amb la significança però més important ajuda a eliminar una zona governada principalment per efectes d'ordres superiors, el que pot ajudar a millorar les prediccions per a aquest procés. Finalment, observem l'efecte d'un dels operadors de dimensió-8 en l'espectre de la massa invariant dels dos fotons per al nostre procés.

Per últim, al capítol 4, expliquem la implementació d'una interfície entre VBFNLO i el generador Herwig que ens permetrà utilitzar la cascada partònica i els models d'hadronització del segon amb les amplituds a segon ordre i els vèrtexs anòmals del primer per als processos de producció de dos i tres bosons vectorials. Aquests processos són d'una gran importància al LHC, ja que permeten mesurar els paràmetres del sector EW i ens donen accés als vèrtexs triples i quàdruples, que en el SM venen fixats pel grup de simetria. Les desviacions dels valors predits pel SM ens donen acoblaments anòmals per a aquests vèrtexs, les contribucions dels quals podem sistematitzar utilitzant una EFT. La primera secció és una xicoteta introducció on expliquem la necessitat d'aquesta interfície. En concret, aprofitar la precisió de següent ordre i els acoblaments anòmals de VBFNLO i la cascada partònica i models d'hadronització de Herwig. A la segona secció expliquem detalladament les funcions que componen la interfície i com està implementada. A la tercera secció mostrem les proves que hem fet per assegurar-nos de la correcta implementació de la interfície. Finalment, a la secció 4, fem una anàlisi de la dependència del procés amb les diverses escales que apareixen al mateix amb cascada partònica i un estudi de la pèrdua de secció eficaç deguda a una migració a través dels talls, en particular del tall de Frixione utilitzat per eliminar la contribució dels fotons de la cascada electromagnètica de forma segura. Com a resultats interessants d'aquesta secció podem mencionar el gran impacte de la migració a través del tall que en alguns casos aplega a ser del 10% i del xicotet valor de la variació de la secció eficaç al variar l'escala que governa la cascada partònica.

Finalment, al capítol 5, hem exposat els resultats i conclusions rellevants del nostre treball. Fent particular èmfasi en la importància dels càlculs de precisió que seran necessaris per a comparar amb els resultats obtinguts experimentalment en el futur pròxim, particularment, en la cerca de nova física.

Bibliography

- [1] G. Aad, T. Abajyan, B. Abbott, J. Abdallah, S. A. Khalek, A. A. Abdelalim, R. Aben, B. Abi, M. Abolins, O. AbouZeid, *et al.*, “Observation of a new particle in the search for the standard model higgs boson with the atlas detector at the lhc,” *Physics Letters B*, vol. 716, no. 1, pp. 1–29, 2012.
- [2] S. Chatrchyan, V. Khachatryan, A. M. Sirunyan, A. Tumasyan, W. Adam, E. Aguilo, T. Bergauer, M. Dragicevic, J. Erö, C. Fabjan, *et al.*, “Observation of a new boson at a mass of 125 gev with the cms experiment at the lhc,” *Physics Letters B*, vol. 716, no. 1, pp. 30–61, 2012.
- [3] M. Peskin, *An introduction to quantum field theory*. CRC press, 2018.
- [4] M. Srednicki, *Quantum field theory*. Cambridge University Press, 2007.
- [5] M. D. Schwartz, *Quantum field theory and the standard model*. Cambridge University Press, 2014.
- [6] S. Weinberg, *The quantum theory of fields*. Cambridge university press, 1995.
- [7] T. Aoyama, M. Hayakawa, T. Kinoshita, and M. Nio, “Tenth-order electron anomalous magnetic moment: Contribution of diagrams without closed lepton loops,” *Physical Review D*, vol. 91, no. 3, p. 033006, 2015.
- [8] D. Hanneke, S. Fogwell, and G. Gabrielse, “New measurement of the electron magnetic moment and the fine structure constant,” *Physical Review Letters*, vol. 100, no. 12, p. 120801, 2008.
- [9] D. Hanneke, S. F. Hoogerheide, and G. Gabrielse, “Cavity control of a single-electron quantum cyclotron: Measuring the electron magnetic moment,” *Physical Review A*, vol. 83, no. 5, p. 052122, 2011.
- [10] C. Baker, D. Doyle, P. Geltenbort, K. Green, M. Van der Grinten, P. Harris, P. Iaydjiev, S. Ivanov, D. May, J. Pendlebury, *et al.*, “Improved experimental limit on the electric dipole moment of the neutron,” *Physical Review Letters*, vol. 97, no. 13, p. 131801, 2006.
- [11] J. Pendlebury, S. Afach, N. Ayres, C. Baker, G. Ban, G. Bison, K. Bodek, M. Burghoff, P. Geltenbort, K. Green, *et al.*, “Revised experimental upper limit on the electric dipole moment of the neutron,” *Physical Review D*, vol. 92, no. 9, p. 092003, 2015.
- [12] B. Graner, Y. Chen, E. Lindahl, B. Heckel, *et al.*, “Reduced limit on the permanent electric dipole moment of hg 199,” *Physical review letters*, vol. 116, no. 16, p. 161601, 2016.

-
- [13] L. D. Faddeev and V. N. Popov, “Feynman diagrams for the yang-mills field,” *Physics Letters B*, vol. 25, no. 1, pp. 29–30, 1967.
- [14] J. C. Romao and J. P. Silva, “A resource for signs and feynman diagrams of the standard model,” *International Journal of Modern Physics A*, vol. 27, no. 26, p. 1230025, 2012.
- [15] D. J. Gross and F. Wilczek, “Ultraviolet behavior of non-abelian gauge theories,” *Physical Review Letters*, vol. 30, no. 26, p. 1343, 1973.
- [16] H. D. Politzer, “Reliable perturbative results for strong interactions?,” *Physical Review Letters*, vol. 30, no. 26, p. 1346, 1973.
- [17] P. Zyla *et al.*, “Review of Particle Physics,” *PTEP*, vol. 2020, no. 8, p. 083C01, 2020.
- [18] S. Weinberg, “A model of leptons,” *Physical review letters*, vol. 19, no. 21, p. 1264, 1967.
- [19] S. L. Glashow, “Partial-symmetries of weak interactions,” *Nuclear physics*, vol. 22, no. 4, pp. 579–588, 1961.
- [20] A. Salam, “Weak and Electromagnetic Interactions,” *Conf. Proc. C*, vol. 680519, pp. 367–377, 1968.
- [21] P. W. Higgs, “Broken symmetries, massless particles and gauge fields,” *Phys. Lett.*, vol. 12, pp. 132–133, 1964.
- [22] P. W. Higgs, “Broken Symmetries and the Masses of Gauge Bosons,” *Phys. Rev. Lett.*, vol. 13, pp. 508–509, 1964.
- [23] F. Englert and R. Brout, “Broken Symmetry and the Mass of Gauge Vector Mesons,” *Phys. Rev. Lett.*, vol. 13, pp. 321–323, 1964.
- [24] N. Cabibbo, “Unitary Symmetry and Leptonic Decays,” *Phys. Rev. Lett.*, vol. 10, pp. 531–533, 1963.
- [25] M. Kobayashi and T. Maskawa, “CP Violation in the Renormalizable Theory of Weak Interaction,” *Prog. Theor. Phys.*, vol. 49, pp. 652–657, 1973.
- [26] K. Hagiwara, R. Szalapski, and D. Zeppenfeld, “Anomalous higgs boson production and decay,” *Physics Letters B*, vol. 318, no. 1, pp. 155–162, 1993.
- [27] K. Hagiwara, S. Ishihara, R. Szalapski, and D. Zeppenfeld, “Low energy effects of new interactions in the electroweak boson sector,” *Physical Review D*, vol. 48, no. 5, p. 2182, 1993.
- [28] C. Degrande, O. Eboli, B. Feigl, B. Jäger, W. Kilian, O. Mattelaer, M. Rauch, J. Reuter, M. Sekulla, and D. Wackerroth, “Monte carlo tools for studies of non-standard electroweak gauge boson interactions in multi-boson processes: A snowmass white paper,” *arXiv preprint arXiv:1309.7890*, 2013.
- [29] B. Grzadkowski, M. Iskrzyński, M. Misiak, and J. Rosiek, “Dimension-six terms in the standard model lagrangian,” *Journal of High Energy Physics*, vol. 2010, no. 10, p. 85, 2010.

- [30] W. Buchmüller and D. Wyler, “Effective lagrangian analysis of new interactions and flavour conservation,” *Nuclear Physics B*, vol. 268, no. 3-4, pp. 621–653, 1986.
- [31] O. J. Éboli, M. Gonzalez-Garcia, and J. Mizukoshi, “ $p p \rightarrow j j e \pm \mu \pm \nu \nu$ and $j j e \pm \mu \pm \nu \nu$ at o (α_{em}^6) and o ($\alpha_{em}^4 \alpha_s^2$) for the study of the quartic electroweak gauge boson vertex at cern lhc,” *Physical Review D*, vol. 74, no. 7, p. 073005, 2006.
- [32] O. Éboli and M. Gonzalez-Garcia, “Mapping the genuine bosonic quartic couplings,” *arXiv preprint arXiv:1604.03555*, 2016.
- [33] P. D. Group, P. Zyla, R. Barnett, J. Beringer, O. Dahl, D. Dwyer, D. Groom, C.-J. Lin, K. Lugovsky, E. Pianori, *et al.*, “Review of particle physics,” *Progress of Theoretical and Experimental Physics*, vol. 2020, no. 8, p. 083C01, 2020.
- [34] J. Campbell, J. Huston, and F. Krauss, *The black book of quantum chromodynamics: a primer for the LHC era*. Oxford University Press, 2018.
- [35] R. P. Feynman, *Photon-hadron interactions*. CRC Press, 2018.
- [36] V. N. Gribov and L. N. Lipatov, “Deep inelastic ep-scattering in a perturbation theory,” tech. rep., Inst. of Nuclear Physics, Leningrad, 1972.
- [37] L. Lipatov, “Parton model and perturbation theory,” tech. rep., Leningrad Inst. of Nuclear Physics, 1974.
- [38] G. Altarelli and G. Parisi, “Asymptotic freedom in parton language,” *Nuclear Physics B*, vol. 126, no. 2, pp. 298–318, 1977.
- [39] Y. L. Dokshitzer, “Calculation of the structure functions for deep inelastic scattering and e^+e^- annihilation by perturbation theory in quantum chromodynamics,” *Zh. Eksp. Teor. Fiz*, vol. 73, p. 1216, 1977.
- [40] R. V. Harlander, S. Y. Klein, and M. Lipp, “Feyngame,” *Computer Physics Communications*, vol. 256, p. 107465, 2020.
- [41] R. K. Ellis, Z. Kunszt, K. Melnikov, and G. Zanderighi, “One-loop calculations in quantum field theory: from feynman diagrams to unitarity cuts,” *Physics reports*, vol. 518, no. 4-5, pp. 141–250, 2012.
- [42] C. G. Bollini and J. J. Giambiagi, “Dimensional renormalization: The number of dimensions as a regularizing parameter,” *Il Nuovo Cimento B (1971-1996)*, vol. 12, no. 1, pp. 20–26, 1972.
- [43] M. Veltman *et al.*, “Regularization and renormalization of gauge fields,” *Nuclear Physics B*, vol. 44, no. 1, pp. 189–213, 1972.
- [44] W. Marciano, “Dimensional regularization and mass singularities,” *Physical Review D*, vol. 12, no. 12, p. 3861, 1975.
- [45] F. Bloch and A. Nordsieck, “Note on the radiation field of the electron,” *Physical Review*, vol. 52, no. 2, p. 54, 1937.
- [46] T. Kinoshita, “Mass singularities of feynman amplitudes,” *Journal of Mathematical Physics*, vol. 3, no. 4, pp. 650–677, 1962.

-
- [47] T.-D. Lee and M. Nauenberg, “Degenerate systems and mass singularities,” *Physical Review*, vol. 133, no. 6B, p. B1549, 1964.
- [48] G. t Hooft and M. Veltman, “Scalar one-loop integrals,” *Nuclear Physics B*, vol. 153, pp. 365–401, 1979.
- [49] A. Denner, U. Nierste, and R. Scharf, “A compact expression for the scalar one-loop four-point function,” *Nuclear Physics B*, vol. 367, no. 3, pp. 637–656, 1991.
- [50] R. K. Ellis and G. Zanderighi, “Scalar one-loop integrals for qcd,” *Journal of High Energy Physics*, vol. 2008, no. 02, p. 002, 2008.
- [51] A. Denner and S. Dittmaier, “Scalar one-loop 4-point integrals,” *Nuclear Physics B*, vol. 844, no. 2, pp. 199–242, 2011.
- [52] A. Denner and S. Dittmaier, “Reduction schemes for one-loop tensor integrals,” *Nuclear Physics B*, vol. 734, no. 1-2, pp. 62–115, 2006.
- [53] F. Campanario, Q. Li, M. Rauch, and M. Spira, “Zz+ jet production via gluon fusion at the lhc,” *Journal of High Energy Physics*, vol. 2013, no. 6, pp. 1–17, 2013.
- [54] F. Campanario, “Towards $pp \rightarrow vvjj$ at nlo qcd: Bosonic contributions to triple vector boson production plus jet,” *Journal of High Energy Physics*, vol. 2011, no. 10, p. 70, 2011.
- [55] G. P. Salam, “Towards jetography,” *The European Physical Journal C*, vol. 67, no. 3-4, pp. 637–686, 2010.
- [56] S. Catani, Y. L. Dokshitzer, M. Olsson, G. Turnock, and B. R. Webber, “New clustering algorithm for multijet cross sections in e^+e^- annihilation,” *Physics Letters B*, vol. 269, no. 3-4, pp. 432–438, 1991.
- [57] S. Catani, Y. L. Dokshitzer, M. H. Seymour, and B. R. Webber, “Longitudinally-invariant k_{\perp} -clustering algorithms for hadron-hadron collisions,” *Nuclear Physics B*, vol. 406, no. 1-2, pp. 187–224, 1993.
- [58] Y. L. Dokshitzer, G. Leder, S. Moretti, and B. Webber, “Better jet clustering algorithms,” *Journal of High Energy Physics*, vol. 1997, no. 08, p. 001, 1997.
- [59] M. Cacciari, G. P. Salam, and G. Soyez, “The anti-kt jet clustering algorithm,” *Journal of High Energy Physics*, vol. 2008, no. 04, p. 063, 2008.
- [60] G. P. Salam and G. Soyez, “A practical seedless infrared-safe cone jet algorithm,” *Journal of High Energy Physics*, vol. 2007, no. 05, p. 086, 2007.
- [61] G. P. Lepage, “A new algorithm for adaptive multidimensional integration,” *Journal of Computational Physics*, vol. 27, no. 2, pp. 192–203, 1978.
- [62] G. P. Lepage, “Vegas-an adaptive multi-dimensional integration program,” tech. rep., 1980.
- [63] K. Fabricius, G. Kramer, G. Schierholz, and I. Schmitt, “Higher order perturbative qcd calculation of jet cross sections in e^+e^- annihilation,” *Zeitschrift für Physik C Particles and Fields*, vol. 11, no. 4, pp. 315–333, 1982.

-
- [64] G. Kramer and B. Lampe, “Jet cross sections in $e^+ e^-$ annihilation,” *Fortschritte der Physik/Progress of Physics*, vol. 37, no. 3, pp. 161–206, 1989.
- [65] H. Baer, J. Ohnemus, and J. Owens, “Next-to-leading-logarithm calculation of jet photoproduction,” *Physical Review D*, vol. 40, no. 9, p. 2844, 1989.
- [66] B. W. Harris and J. F. Owens, “Two cutoff phase space slicing method,” *Physical Review D*, vol. 65, no. 9, p. 094032, 2002.
- [67] S. Frixione, “A general approach to jet cross sections in qcd,” *Nuclear Physics B*, vol. 507, no. 1-2, pp. 295–314, 1997.
- [68] S. Frixione, Z. Kunszt, and A. Signer, “Three-jet cross sections to next-to-leading order,” *Nuclear Physics B*, vol. 467, no. 3, pp. 399–442, 1996.
- [69] S. Catani and M. Seymour, “A General algorithm for calculating jet cross-sections in NLO QCD,” *Nucl. Phys. B*, vol. 485, pp. 291–419, 1997. [Erratum: Nucl.Phys.B 510, 503–504 (1998)].
- [70] S. Catani, S. Dittmaier, M. H. Seymour, and Z. Trocsanyi, “The dipole formalism for next-to-leading order qcd calculations with massive partons,” *Nuclear Physics B*, vol. 627, no. 1-2, pp. 189–265, 2002.
- [71] S. Frixione and B. R. Webber, “Matching nlo qcd computations and parton shower simulations,” *Journal of High Energy Physics*, vol. 2002, no. 06, p. 029, 2002.
- [72] H. Baer, J. Ohnemus, and J. Owens, “Next-to-leading-logarithm calculation of direct photon production,” *Physical Review D*, vol. 42, no. 1, p. 61, 1990.
- [73] P. Aurenche, R. Baier, and M. Fontannaz, “Prompt photon production at colliders,” *Physical Review D*, vol. 42, no. 5, p. 1440, 1990.
- [74] E. L. Berger and J. Qiu, “Calculations of prompt-photon production in qcd,” *Physical Review D*, vol. 44, no. 7, p. 2002, 1991.
- [75] E. Glover and W. Stirling, “Isolated hard photon radiation in multijet production at lep,” *Physics Letters B*, vol. 295, no. 1-2, pp. 128–135, 1992.
- [76] Z. Kunszt and Z. Trócsányi, “Qcd corrections to photon production in association with hadrons in $e^+ e^-$ annihilation,” *Nuclear Physics B*, vol. 394, no. 1, pp. 139–168, 1993.
- [77] L. Gordon and W. Vogelsang, “Polarized and unpolarized prompt photon production beyond the leading order,” *Physical Review D*, vol. 48, no. 7, p. 3136, 1993.
- [78] E. N. Glover and A. Morgan, “Measuring the photon fragmentation function at lep,” *Zeitschrift für Physik C Particles and Fields*, vol. 62, no. 2, pp. 311–321, 1994.
- [79] S. Frixione, “Isolated photons in perturbative qcd,” *Physics Letters B*, vol. 429, no. 3-4, pp. 369–374, 1998.
- [80] F. Campanario, M. Kerner, D. Ninh, and I. Rosario, “Diphoton production in vector-boson scattering at the LHC at next-to-leading order QCD,” *JHEP*, vol. 06, p. 072, 2020.

-
- [81] D. Buarque *et al.*, “Vector Boson Scattering Processes: Status and Prospects,” 6 2021.
- [82] R. Covarelli, M. Pellen, and M. Zaro, “Vector-Boson scattering at the LHC: Unraveling the electroweak sector,” *Int. J. Mod. Phys. A*, vol. 36, no. 16, p. 2130009, 2021.
- [83] B. Feigl, *Electroweak processes in the standard model and beyond: backgrounds to Higgs physics and semileptonic decay modes*. PhD thesis, PhD Thesis, ITP Karlsruhe 2013, <https://digbib.ubka.uni-karlsruhe.de/volltexte/1000037298.>, 2013.
- [84] J. R. Andersen and J. M. Smillie, “Qcd and electroweak interference in higgs production by gauge boson fusion,” *Physical Review D*, vol. 75, no. 3, p. 037301, 2007.
- [85] A. Bredenstein, K. Hagiwara, and B. Jäger, “Mixed qcd-electroweak contributions to higgs-plus-dijet production at the cern lhc,” *Physical Review D*, vol. 77, no. 7, p. 073004, 2008.
- [86] F. Campanario, T. M. Figy, S. Plätzer, M. Rauch, P. Schichtel, and M. Sjö Dahl, “Stress testing the vector-boson-fusion approximation in multijet final states,” *Physical Review D*, vol. 98, no. 3, p. 033003, 2018.
- [87] T. Gehrmann, N. Greiner, and G. Heinrich, “Precise QCD predictions for the production of a photon pair in association with two jets,” *Phys. Rev. Lett.*, vol. 111, p. 222002, 2013.
- [88] S. Badger, A. Guffanti, and V. Yundin, “Next-to-leading order QCD corrections to di-photon production in association with up to three jets at the Large Hadron Collider,” *JHEP*, vol. 03, p. 122, 2014.
- [89] Z. Bern, L. Dixon, F. F. Cordero, S. Hoeche, H. Ita, D. Kosower, N. L. Presti, and D. Maitre, “Next-to-leading order $\gamma \gamma + 2$ - jet production at the lhc,” *Physical Review D*, vol. 90, no. 5, p. 054004, 2014.
- [90] K. Arnold, M. Bähr, G. Bozzi, F. Campanario, C. Englert, T. Figy, N. Greiner, C. Hackstein, V. Hankele, B. Jäger, *et al.*, “Vbfnlo: a parton level monte carlo for processes with electroweak bosons,” *Computer Physics Communications*, vol. 180, no. 9, pp. 1661–1670, 2009.
- [91] J. Baglio, J. Bellm, G. Bozzi, M. Brieg, F. Campanario, C. Englert, B. Feigl, J. Frank, T. Figy, F. Geyer, *et al.*, “Vbfnlo: A parton level monte carlo for processes with electroweak bosons—manual for version 2.7. 0,” *arXiv preprint arXiv:1107.4038*, 2011.
- [92] K. Arnold, J. Bellm, G. Bozzi, F. Campanario, C. Englert, B. Feigl, J. Frank, T. Figy, B. Jager, M. Kerner, *et al.*, “Release note—vbfnlo-2.6. 0,” *arXiv preprint arXiv:1207.4975*, 2012.
- [93] J. Baglio, J. Bellm, F. Campanario, B. Feigl, J. Frank, T. Figy, M. Kerner, L. Ninh, S. Palmer, M. Rauch, *et al.*, “Release note—vbfnlo 2.7. 0,” *arXiv preprint arXiv:1404.3940*, 2014.
- [94] K. Hagiwara and D. Zeppenfeld, “Amplitudes for multi-parton processes involving a current at $e^+ e^-$, $e^\pm p$, and hadron colliders,” *Nuclear Physics B*, vol. 313, no. 3, pp. 560–594, 1989.

-
- [95] H. Murayama, I. Watanabe, and K. Hagiwara, “Helas: Helicity amplitude subroutines for feynman diagram evaluations,” tech. rep., National Lab. for High Energy Physics, 1992.
- [96] J. Butterworth, S. Carrazza, A. Cooper-Sarkar, A. De Roeck, J. Feltesse, S. Forte, J. Gao, S. Glazov, J. Huston, Z. Kassabov, *et al.*, “Pdf4lhc recommendations for lhc run ii,” *Journal of Physics G: Nuclear and Particle Physics*, vol. 43, no. 2, p. 023001, 2016.
- [97] A. Buckley, J. Ferrando, S. Lloyd, K. Nordström, B. Page, M. Rüfenacht, M. Schönherr, and G. Watt, “Lhapdf6: parton density access in the lhc precision era,” *The European Physical Journal C*, vol. 75, no. 3, pp. 1–20, 2015.
- [98] M. Aaboud *et al.*, “Measurements of integrated and differential cross sections for isolated photon pair production in pp collisions at $\sqrt{s} = 8$ TeV with the ATLAS detector,” *Phys. Rev. D*, vol. 95, no. 11, p. 112005, 2017.
- [99] G. Aad *et al.*, “Measurement of isolated-photon pair production in pp collisions at $\sqrt{s} = 7$ TeV with the ATLAS detector,” *JHEP*, vol. 01, p. 086, 2013.
- [100] G. Aad *et al.*, “Measurements of $W\gamma$ and $Z\gamma$ production in pp collisions at $\sqrt{s}=7$ TeV with the ATLAS detector at the LHC,” *Phys. Rev. D*, vol. 87, no. 11, p. 112003, 2013. [Erratum: Phys.Rev.D 91, 119901 (2015)].
- [101] G. Aad *et al.*, “Measurements of $Z\gamma$ and $Z\gamma\gamma$ production in pp collisions at $\sqrt{s} = 8$ TeV with the ATLAS detector,” *Phys. Rev. D*, vol. 93, no. 11, p. 112002, 2016.
- [102] M. Aaboud *et al.*, “Measurement of $WW/WZ \rightarrow \ell\nu qq'$ production with the hadronically decaying boson reconstructed as one or two jets in pp collisions at $\sqrt{s} = 8$ TeV with ATLAS, and constraints on anomalous gauge couplings,” *Eur. Phys. J. C*, vol. 77, no. 8, p. 563, 2017.
- [103] M. Aaboud *et al.*, “Measurement of the W^+W^- production cross section in pp collisions at a centre-of-mass energy of $\sqrt{s} = 13$ TeV with the ATLAS experiment,” *Phys. Lett. B*, vol. 773, pp. 354–374, 2017.
- [104] M. Aaboud *et al.*, “Measurement of W^+W^- production in association with one jet in proton–proton collisions at $\sqrt{s} = 8$ TeV with the ATLAS detector,” *Phys. Lett. B*, vol. 763, pp. 114–133, 2016.
- [105] G. Aad *et al.*, “Measurement of W^+W^- production in pp collisions at $\sqrt{s}=7$ TeV with the ATLAS detector and limits on anomalous WWZ and WW γ couplings,” *Phys. Rev. D*, vol. 87, no. 11, p. 112001, 2013. [Erratum: Phys.Rev.D 88, 079906 (2013)].
- [106] G. Aad *et al.*, “Measurement of total and differential W^+W^- production cross sections in proton-proton collisions at $\sqrt{s} = 8$ TeV with the ATLAS detector and limits on anomalous triple-gauge-boson couplings,” *JHEP*, vol. 09, p. 029, 2016.
- [107] G. Aad *et al.*, “Simultaneous measurements of the $t\bar{t}$, W^+W^- , and $Z/\gamma^* \rightarrow \tau\tau$ production cross-sections in pp collisions at $\sqrt{s} = 7$ TeV with the ATLAS detector,” *Phys. Rev. D*, vol. 91, no. 5, p. 052005, 2015.

-
- [108] M. Aaboud *et al.*, “Measurement of the $W^\pm Z$ boson pair-production cross section in pp collisions at $\sqrt{s} = 13$ TeV with the ATLAS Detector,” *Phys. Lett. B*, vol. 762, pp. 1–22, 2016.
- [109] G. Aad *et al.*, “Measurements of $W^\pm Z$ production cross sections in pp collisions at $\sqrt{s} = 8$ TeV with the ATLAS detector and limits on anomalous gauge boson self-couplings,” *Phys. Rev. D*, vol. 93, no. 9, p. 092004, 2016.
- [110] G. Aad *et al.*, “Measurement of WZ production in proton-proton collisions at $\sqrt{s} = 7$ TeV with the ATLAS detector,” *Eur. Phys. J. C*, vol. 72, p. 2173, 2012.
- [111] “ $ZZ \rightarrow \ell^+ \ell^- \ell'^+ \ell'^-$ cross-section measurements and aTGC search in 13 TeV pp collisions with the ATLAS detector,” 5 2017.
- [112] M. Aaboud *et al.*, “Measurement of the ZZ production cross section in proton-proton collisions at $\sqrt{s} = 8$ TeV using the $ZZ \rightarrow \ell^- \ell^+ \ell'^- \ell'^+$ and $ZZ \rightarrow \ell^- \ell^+ \nu \bar{\nu}$ channels with the ATLAS detector,” *JHEP*, vol. 01, p. 099, 2017.
- [113] G. Aad *et al.*, “Measurement of ZZ production in pp collisions at $\sqrt{s} = 7$ TeV and limits on anomalous ZZZ and $ZZ\gamma$ couplings with the ATLAS detector,” *JHEP*, vol. 03, p. 128, 2013.
- [114] G. Aad *et al.*, “Measurements of four-lepton production in pp collisions at $\sqrt{s} = 8$ TeV with the ATLAS detector,” *Phys. Lett. B*, vol. 753, pp. 552–572, 2016.
- [115] S. Chatrchyan *et al.*, “Measurement of the Sum of WW and WZ Production with W +Dijet Events in pp Collisions at $\sqrt{s} = 7$ TeV,” *Eur. Phys. J. C*, vol. 73, no. 2, p. 2283, 2013.
- [116] S. Chatrchyan *et al.*, “Measurement of the W^+W^- Cross Section in pp Collisions at $\sqrt{s} = 7$ TeV and Limits on Anomalous $WW\gamma$ and WWZ Couplings,” *Eur. Phys. J. C*, vol. 73, no. 10, p. 2610, 2013.
- [117] V. Khachatryan *et al.*, “Measurement of the W^+W^- cross section in pp collisions at $\sqrt{s} = 8$ TeV and limits on anomalous gauge couplings,” *Eur. Phys. J. C*, vol. 76, no. 7, p. 401, 2016.
- [118] V. Khachatryan *et al.*, “Measurement of the WZ production cross section in pp collisions at $\sqrt{s} = 7$ and 8 TeV and search for anomalous triple gauge couplings at $\sqrt{s} = 8$ TeV,” *Eur. Phys. J. C*, vol. 77, no. 4, p. 236, 2017.
- [119] S. Chatrchyan *et al.*, “Measurement of the $W\gamma$ and $Z\gamma$ Inclusive Cross Sections in pp Collisions at $\sqrt{s} = 7$ TeV and Limits on Anomalous Triple Gauge Boson Couplings,” *Phys. Rev. D*, vol. 89, no. 9, p. 092005, 2014.
- [120] V. Khachatryan *et al.*, “Measurement of the $Z\gamma$ Production Cross Section in pp Collisions at 8 TeV and Search for Anomalous Triple Gauge Boson Couplings,” *JHEP*, vol. 04, p. 164, 2015.
- [121] S. Chatrchyan *et al.*, “Measurement of the ZZ Production Cross Section and Search for Anomalous Couplings in 2 l2l' Final States in pp Collisions at $\sqrt{s} = 7$ TeV,” *JHEP*, vol. 01, p. 063, 2013.

-
- [122] V. Khachatryan *et al.*, “Measurement of the $pp \rightarrow ZZ$ Production Cross Section and Constraints on Anomalous Triple Gauge Couplings in Four-Lepton Final States at $\sqrt{s} = 8$ TeV,” *Phys. Lett. B*, vol. 740, pp. 250–272, 2015. [Erratum: *Phys.Lett.B* 757, 569–569 (2016)].
- [123] S. Chatrchyan *et al.*, “Study of Exclusive Two-Photon Production of W^+W^- in pp Collisions at $\sqrt{s} = 7$ TeV and Constraints on Anomalous Quartic Gauge Couplings,” *JHEP*, vol. 07, p. 116, 2013.
- [124] V. Khachatryan *et al.*, “Evidence for exclusive $\gamma\gamma \rightarrow W^+W^-$ production and constraints on anomalous quartic gauge couplings in pp collisions at $\sqrt{s} = 7$ and 8 TeV,” *JHEP*, vol. 08, p. 119, 2016.
- [125] “Observation of heavy triboson production in leptonic final states in proton-proton collisions at $\sqrt{s} = 13$ TeV,” 2020.
- [126] G. Aad, B. Abbott, D. C. Abbott, A. A. Abud, K. Abeling, D. Abhayasinghe, S. Abidi, O. AbouZeid, N. Abraham, H. Abramowicz, *et al.*, “Evidence for the production of three massive vector bosons with the atlas detector,” *Physics Letters B*, vol. 798, p. 134913, 2019.
- [127] M. Aaboud *et al.*, “Search for triboson $W^\pm W^\pm W^\mp$ production in pp collisions at $\sqrt{s} = 8$ TeV with the ATLAS detector,” *Eur. Phys. J. C*, vol. 77, no. 3, p. 141, 2017.
- [128] C. collaboration *et al.*, “Search for the production of $w^\pm w^\pm w$ events at $s = 13$ tev,” *Physical Review D*, vol. 100, no. 1, p. 012004, 2019.
- [129] M. Aaboud *et al.*, “Study of $WW\gamma$ and $WZ\gamma$ production in pp collisions at $\sqrt{s} = 8$ TeV and search for anomalous quartic gauge couplings with the ATLAS experiment,” *Eur. Phys. J. C*, vol. 77, no. 9, p. 646, 2017.
- [130] J. Bellm, *NLO-QCD-Korrekturen zur WZ-und $W\gamma$ -Produktion am LHC*. PhD thesis, Diploma Thesis, ITP Karlsruhe 2012, <http://www.itp.kit.edu/diplomatheses...>, 2012.
- [131] V. Hankele and D. Zeppenfeld, “Qcd corrections to hadronic wwz production with leptonic decays,” *Physics Letters B*, vol. 661, no. 2-3, pp. 103–108, 2008.
- [132] F. Campanario, V. Hankele, C. Oleari, S. Prestel, and D. Zeppenfeld, “Qcd corrections to charged triple vector boson production with leptonic decay,” *Physical Review D*, vol. 78, no. 9, p. 094012, 2008.
- [133] G. Bozzi, F. Campanario, V. Hankele, and D. Zeppenfeld, “Next-to-leading order qcd corrections to $w^+ w^- \gamma$ and $z z \gamma$ production with leptonic decays,” *Physical Review D*, vol. 81, no. 9, p. 094030, 2010.
- [134] G. Bozzi, F. Campanario, M. Rauch, H. Rzehak, and D. Zeppenfeld, “Nlo qcd corrections to $w^\pm z \gamma$ production with leptonic decays,” *Physics Letters B*, vol. 696, no. 4, pp. 380–385, 2011.
- [135] G. Bozzi, F. Campanario, M. Rauch, and D. Zeppenfeld, “ $W \gamma \gamma$ production with leptonic decays at next-to-leading order qcd,” *Physical Review D*, vol. 83, no. 11, p. 114035, 2011.

-
- [136] G. Bozzi, F. Campanario, M. Rauch, and D. Zeppenfeld, “Z $\gamma\gamma$ production with leptonic decays and triple photon production at next-to-leading order qcd,” *Physical Review D*, vol. 84, no. 7, p. 074028, 2011.
- [137] M. Bähr, S. Gieseke, M. A. Gigg, D. Grellscheid, K. Hamilton, O. Latunde-Dada, S. Plätzer, P. Richardson, M. H. Seymour, A. Sherstnev, *et al.*, “Herwig++ physics and manual,” *The European Physical Journal C*, vol. 58, no. 4, pp. 639–707, 2008.
- [138] J. Bellm, S. Gieseke, D. Grellscheid, S. Plätzer, M. Rauch, C. Reuschle, P. Richardson, P. Schichtel, M. H. Seymour, A. Siódmok, *et al.*, “Herwig 7.0/herwig++ 3.0 release note,” *The European Physical Journal C*, vol. 76, no. 4, pp. 1–8, 2016.
- [139] T. Sjöstrand, S. Ask, J. R. Christiansen, R. Corke, N. Desai, P. Ilten, S. Mrenna, S. Prestel, C. O. Rasmussen, and P. Z. Skands, “An introduction to pythia 8.2,” *Computer physics communications*, vol. 191, pp. 159–177, 2015.
- [140] T. Sjöstrand, S. Mrenna, and P. Skands, “Pythia 6.4 physics and manual,” *Journal of High Energy Physics*, vol. 2006, no. 05, p. 026, 2006.
- [141] E. Bothmann, G. S. Chahal, S. Hoche, J. Krause, F. Krauss, S. Kuttimalai, S. Liebschner, D. Napoletano, M. Schonherr, H. Schulz, *et al.*, “Event generation with sherpa 2.2.,” *SciPost physics.*, vol. 7, p. 034, 2019.
- [142] T. Binoth, F. Boudjema, G. Dissertori, A. Lazopoulos, A. Denner, S. Dittmaier, R. Frederix, N. Greiner, S. Höche, W. Giele, *et al.*, “A proposal for a standard interface between monte carlo tools and one-loop programs,” *Computer Physics Communications*, vol. 181, no. 9, pp. 1612–1622, 2010.
- [143] S. Alioli, S. Badger, J. Bellm, B. Biedermann, F. Boudjema, G. Cullen, A. Denner, H. Van Deurzen, S. Dittmaier, R. Frederix, *et al.*, “Update of the binoth les houches accord for a standard interface between monte carlo tools and one-loop programs,” *Computer Physics Communications*, vol. 185, no. 2, pp. 560–571, 2014.
- [144] J. Alwall, R. Frederix, S. Frixione, V. Hirschi, F. Maltoni, O. Mattelaer, H.-S. Shao, T. Stelzer, P. Torrielli, and M. Zaro, “The automated computation of tree-level and next-to-leading order differential cross sections, and their matching to parton shower simulations,” *Journal of High Energy Physics*, vol. 2014, no. 7, p. 79, 2014.
- [145] L. A. Harland-Lang, A. Martin, P. Motylinski, and R. Thorne, “Parton distributions in the lhc era: Mmht 2014 pdfs,” *The European Physical Journal C*, vol. 75, no. 5, pp. 1–53, 2015.